Application of Bifurcation Theory to Subsynchronous Resonance in Power Systems

by

Ahmad M. Harb

Dissertation submitted to the faculty of the
Virginia Polytechnic Institute and State University
in partial fulfillment of the requirements for the degree of

DOCTOR OF PHILOSOPHY

in

Electrical Engineering

APPROVED:

Ali H. Nayfeh, Chairman

Lamine M. Mili, Co-Chairman

Arun G. Phadke

H. F. Van Landingham

Dean T. Mook

December, 1996
Blacksburg, Virginia

keywords: Subsynchronous Resonance, Bifurcation Theory, Power Systems, Methods of Multiple Scales.

Application of Bifurcation Theory to Subsynchronous Resonance in Power Systems

by

Ahmad M. Harb

Committee Chairman: Ali H. Nayfeh

Electrical Engineering

(ABSTRACT)

A bifurcation analysis is used to investigate the complex dynamics of two heavily loaded single-machine-infinite-busbar power systems modeling the characteristics of the BOARDMAN generator with respect to the rest of the North-Western American Power System and the CHOLLA# generator with respect to the SOWARO station. In the BOARDMAN system, we show that there are three Hopf bifurcations at practical compensation values, while in the CHOLLA#4 system, we show that there is only one Hopf bifurcation.

The results show that as the compensation level increases, the operating condition loses stability with a complex conjugate pair of eigenvalues of the Jacobian matrix crossing transversely from the left- to the right-half of the complex plane, signifying a Hopf bifurcation. As a result, the power system oscillates subsynchronously with a small limit-cycle attractor. As the compensation level increases, the limit cycle grows and then loses stability via a secondary Hopf bifurcation, resulting in the creation of a two-period quasiperiodic subsynchronous oscillation, a two-torus attractor. On further increases of the compensation level, the quasiperiodic attractor collides with its basin boundary, resulting in the destruction of the attractor and its basin boundary in a bluesky catastrophe. Consequently, there are no bounded motions.

When a damper winding is placed either along the q-axis, or d-axis, or both axes of the BOARDMAN system and the machine saturation is considered in the CHOLLA#4 system, the study shows that, there is only one Hopf bifurcation and it occurs at a much lower level of compensation, indicating that the damper windings and the machine saturation destabilize the system by inducing subsynchronous resonance.

Finally, we investigate the effect of linear and nonlinear controllers on mitigating subsynchronous resonance in the CHOLLA#4 system . The study shows that the linear controller increases the compensation level at which subsynchronous resonance occurs and the nonlinear controller does not affect the location and type of the Hopf bifurcation, but it reduces the amplitude of the limit cycle born as a result of the Hopf bifurcation.

ACKNOWLEDGEMENTS

All praise and thanks be to Allah, God the Almighty, most beneficent and most merciful. I am grateful to my advisors, Dr. Ali H. Nayfeh and Dr. Lamine M. Mili, for their valuable guidance and advices during this research. Also my thanks to Dr. Arun Phadke, Dr. Vanlandingham, and Dr. Dean Mook for serving in my committee. I also thank my family back home for their continuous support specially my great parents, *Mohammad* and *Mariam*. Not to be forgotten my lovely wife,*Kamelia*, and the two beautiful daughters, *Banah* and *Talah*, for the long lonely nights they spent while I was busy with this research. I would like to thank my friends in the nonlinear dynamics laborotaries, specially Dr. Char_Ming Chin for his valuable discussions.

TABLE OF CONTENTS

LIST OF FIGURES

Chapter 1

INTRODUCTION

1.1 Problem Definition and Literature Review

1.1.1 Subsynchronous Resonance Problem

In power systems, series capacitors are being installed by many electric utilities to increase the power transfer capability of the transmission lines as well as to improve the stability of these systems. However, this introduces problems together with the benefits, namely the occurrence of undesirable oscillations that may lead to the destruction of the shaft of the turbine or the loss of synchronism of the generator. This phenomenon has been given the name subsynchronous resonance or SSR for short[1].

The phenomenon of SSR was brought to general attention in connection with the two damages that occurred to the turbine-generator shafts at the Mohave Generating Station in southern Nevada in the United States of America in December of 1970 and October of 1971. These two failures have been analyzed by Walker et al. [2], among others. Walker and his colleagues found that the failures occurred in the shaft section between the generator and the exciter of the main generator collector are due to torsional fatigue. They concluded that a conducting path was generated from each collector ring through the insulating sleeves to the shaft. Heavy current flowing through the double ground then eroded large pockets of metal from the shaft and collector rings. Analysis of line current oscillograms taken during the disturbance indicate the presence of appreciable magnitudes of currents at subsynchronous frequency. These currents produced subsynchronous torques on the generator of approximately the same magnitude, but at a slip frequency that was very nearly equal to the frequency of the second torsional mode of the shaft system. The

latter involved, essentially, the exciter-alternator shaft, which was oscillating mechanically against the remaining shaft inertial elements, thereby causing the destruction of the shaft of the turbine-generator system.

1.1.2 Types of SSR

There are many ways in which the system and the generator may interact under subsynchronous resonance conditions. Farmer et al. [3], in their analysis carried out during the Navajo project, identified three types of subsynchronous resonance. They have been called induction generator effect, torsional interaction effect, and transient torque effect. These three interactions, which are of particular interest, are briefly discussed next.

As mentioned in [4-9], the induction generator effect is caused by self-excitation of the synchronous generators when the resistance of the rotor to the subsynchronous current, viewed from the armature terminal, becomes negative. The network also presents a positive resistance to these same currents. However, if the negative resistance of the generator is greater in magnitude than the positive resistance of the network at the natural frequencies, there will be sustained subsynchronous currents.

The torsional interaction effect occurs when the slip frequency, which is equal to the difference between the synchronous and subsynchronous frequencies (i.e., $f - f_n$), is close to a torsional mode frequency "f_m" of the shaft. Consequently, generator-rotor oscillations can build up to induce armature voltage components of subsynchronous and supersynchronous frequencies [8]. The subsynchronous frequency voltage is phased to sustain the subsynchronous torque. If the latter equals or exceeds the inherent mechanical damping torque of the rotating system, the system will become self-excited. As a result, severe torque amplification can occur, resulting in damage to the shaft of the machine.

As for transient torques, they are not self-excited. They are rather induced by system disturbances, which tend to excite the natural frequencies of the network. This causes the generator-turbine masses to oscillate relative to one another at one or more of their natural frequencies depending on the system disturbance.

1.1.3 SSR Countermeasures

As a solution to SSR problems, several countermeasures have been applied and more have been suggested in the literature. We will summarize the ones proposed by Farmer et al. [3] and the General Electric system. Regarding the elimination of the induction generator effect, they recommend that the generator be equipped with poleface amortisseurs. As for the mitigation of the torsional interaction effect, they suggest the installation of filters in series with the generator to increase the circuit resistance for each torsional mode. Finally, to reduce the transient torque on the turbine-generator shafts to the level that shaft fracture may not occur for any single transient incident, they suggest the adoption of a capacitor dual gap flashing scheme. Because of the high amplitudes of oscillations and the fast torque build up, transient torque problems require more extreme and costly countermeasures than those needed to mitigate the self-excitation cases.

A linear excitation system controller, namely GENEREX, has been implemented by Beagles et al. [10]. This type of controller is used to enlarge the stability region. In this DISSERTATION, in addition to the linear controller, we design a nonlinear controller to reduce the amplitudes of the nonlinear oscillations in the unstable region.

1.1.4 Analytical Tools

There are several techniques proposed to study the phenomenon of SSR. They can be classified into two categories, namely linear and nonlinear techniques. The most common of these techniques are frequency scanning, eigenvalue analysis, and ElectroMagnetic Transient Program (EMTP) analysis (see Anderson et al. [8] and [11-13], among others). The first two methods are linear and the third one is nonlinear.

The frequency scanning technique has been utilized by Ballance and Goldberg [1], Kilgore et al. [12], Farmer et al. [3], Rana et al. [13], and Edris [11], among others. This method has been widely used in North America for at least a preliminary analysis of the SSR problem. It is particularly effective in the study of the induction generator effect. It

computes, as a function of frequency, the equivalent resistance and reactance that are seen looking into the network from a point behind the stator winding of a particular generator. While being relatively inexpensive for large systems, the frequency scanning method cannot identify self-excited torsional oscillations. For analyzing this type of oscillations, one resorts to eigenvalue analysis.

The eigenvalue analysis technique has been utilized by Yu [14], Fouad and Khu [15], Walker et al. [2], Yan and Yu [16], Anderson et al. [8], and Iravani and Edris, [17], to cite a few. It is performed with the network and the generators modeled in a linearized system of differential equations. It is a very attractive technique because it provides both the frequencies of oscillation and the damping at each frequency. However, the eigenvalue analysis technique is relatively expensive, especially for large power systems.

To avoid linearizing the differential equations, Gross and Hall [9] and Edris [11], among others, have used EMTP. The latter numerically integrates the set of nonlinear differential equation that govern the power system. EMTP is a full three-phase model of the system with much more detailed modeling of the transmission lines, cables, machines, and special devices, such as series capacitors, with complex bypass switching arrangements. Moreover, EMTP permits nonlinear modeling of complex system components. It is, therefore, well suited for the analysis of SSR problems.

EMTP has also been used by several authors [9, 18-21] to invalidate the results predicted by the linearized theories, especially the eigenvalue analysis. The latter predicts that disturbances to the power system decay below a critical compensation level μ_c at which a complex conjugate pair of eigenvalues crosses the imaginary axis into the right-half of the complex plane and exponentially grow above μ_c. In nonlinear dynamics, μ_c is known as a Hopf bifurcation value. But, numerical simulations using EMTP demonstrate that the nonlinearities put a cap on the exponential growth. This limitation of the linearized theories has prompted a growing interest in nonlinear bifurcation methods.

In recent years, power system dynamics has been studied from the point of view of geometric methods of nonlinear dynamics. The presence of different types of bifurcation

in power system models has been revealed. The most commonly encountered bifurcation in these models is the Hopf bifurcation. Abed and Varaiya [22] were the first to spot a subcritical Hopf bifurcation in a voltage stability model of a power system consisting of a machine with an excitation system connected to an infinite busbar. Later, Dobson and Chiang [23], Nayfeh et al. [24], Venkatasubramanian et al. [25], Ajjarapu and Lee [26], among others, studied voltage stability by investigating the bifurcation of static and dynamic solutions. Recently, Abed et al. [27], Ji and Venkatasubramian [28], and Nayfeh et al. [29] showed that the birth or death of limit cycles from an equilibrium point gives rise to oscillations that may undergo period multiplications, cyclic folds, and crises.

In the SSR area, Zhu [18] and Zhu et al. [20] were the first to employ bifurcation methods to demonstrate the existence of a Hopf bifurcation in a single-machine-infinite-busbar power system. They appealed to the Hopf bifurcation theorem to show that the bifurcation is supercritical and, hence, it leads to the birth of a stable small-amplitude limit cycle. They validated these results with numerical simulations obtained by using EMTP. Zhu [18] found that, as the series compensation level increases, the limit cycle loses stability with a complex conjugate pair of Floquet multipliers leaving the unit circle in the complex plane away from the real axis. This indicates a two-period quasiperiodic (two-torus) motion. She conjectured that the torus is unstable. In this DISSERTATION, we show that the created two-torus is stable and that as the compensation level increases, it loses stability in a bluesky catastrophe.

1.2 Objectives and Scope of the DISSERTATION

In this DISSERTATION, we concentrate on the second type of self-excitation, which results from the interaction of the electrical subsynchronous mode with a torsional mode. Bifurcation theory, Floquet theory, and the method of multiple scales [30] are used to investigate the complex dynamics of a series capacitor compensated single-machine-infinite-busbar power system. Two practical power system models are used, namely the BOARDMAN and

CHOLLA#4.

In the BOARDMAN model, the dynamics of the automatic voltage regulator (AVR), the turbine governor, and the generator saturation are neglected. We consider two cases, one without damper windings and the other one with. In the first case, we extend the work of Zhu [18] by revealing the existence of not one but three supercritical Hopf bifurcations for practical compensation values. We show that they result from the interaction of the electrical subsynchronous mode with one of the mechanical modes of the system. In addition, we use a combination of a two-point boundary-value scheme and Floquet theory to unveil the presence of three secondary Hopf bifurcations. In their vicinity, the oscillations have two incommensurate periods with bounded amplitudes, yielding two-period quasiperiodic motions (two-torus). Finally, we show that these attractors grow in size until they collide with their basins of attraction, resulting in their joint destruction in a bluesky catastrophe. Above this level of compensation, the oscillations become unbounded and the generator permanently loses synchronism. These scenarios are validated through time-domain simulations obtained by integrating the differential equations that govern the system. We have also studied the effects of the damper windings on SSR. We found that placing damper windings on either the q-axis, or the d-axis, or both axes reduces the compensation level at which the system loses stability via a Hopf bifurcation.

The effect of the generator saturation has been analyzed in another power system model, namely the CHOLLA#4 model. Here, the dynamics of the turbine governor have been neglected. When the saturation and automatic voltage regulator (AVR) are neglected, it is shown that there is only one supercritical Hopf bifurcation point in the vicinity of which there exist small stable limit cycles. As the compensation level of the line increases, the limit cycles grow in size and then undergo a secondary Hopf bifurcation, which leads to two-period quasiperiodic attractors. When the generator saturation is accounted for, it is found that the supercritical Hopf bifurcation point occurs at a lower level of compensation, implying a decrease in the positively damped region.

To move the Hopf bifurcation point to higher capacitor compensation values (i.e., to

enlarge the stability region), we have used a PSS-type linear controller that acts on the excitation system. Moreover, to decrease the amplitudes of the nonlinear oscillations in the unstable region, we have designed a nonlinear (quadratic) controller that injects an additional stabilizing signal into the automatic voltage regulator (AVR). We note that, for both the linear and nonlinear controllers, the input signal is the deviation of thr generator-rotor frequency from the synchronous frequency.

1.3 Outline of the DISSERTATION

The DISSERTATION is organized as follows. Chapter 2 briefly reviews methods of modern nonlinear dynamics, such as bifurcation and Floquet theories and the method of multiple scales. Chapter 3 studies the effect of damper windings on the subsynchronous resonance of the BOARDMAN model. Chapter 4 analyzes the effect of the generator saturation on the SSR of the CHOLLA#4 model. In Chapter 5, mitigation of SSR in CHOLLA#4 through linear and nonlinear controllers is demonstrated. Finally, some conclusions and recommendations for future work are given in Chapter 6.

Chapter 2

A REVIEW OF MODERN NONLINEAR DYNAMICS

In this chapter, methods of modern nonlinear dynamics are briefly reviewed [30]. Specifically, the constant solutions and their stability are analyzed using bifurcation theory. The method of multiple scales [31] is implemented to find the normal form of the system near the Hopf bifurcation points. Moreover, Floquet theory is employed to study the stability of limit cycles.

2.1 Equilibrium Solutions

The equilibrium solutions or constant solutions of an autonomous system defined by

$$\dot{\mathbf{x}} = \mathbf{F}(\mathbf{x}; \mu) \tag{2.1}$$

where $\mathbf{x}$ is a state variables vector, $x_1, x_2, ..., x_n$, n is an integer number, $\mathbf{F}$ is the field vector, and μ is the control parameter of the system, correspond to

$$\dot{\mathbf{x}} = \mathbf{0} \tag{2.2}$$

By equating the right-hand side of Eq. (2.1) to zero, we end up with either linear or nonlinear algebraic equations. If the function $\mathbf{F}$ in Eq. (2.1) is linear, then the system is linear. So, it has only one constant solution, namely, the trivial solution if the system matrix is nonsingular. In contrast, for a nonlinear system, there may be more than one constant or equilibrium solution. Using a continuation scheme, discussed in Sec. 2.3, we solve these equations as a function of the control parameter μ. The stability of this type of solution is discussed next.

2.1.1 Stability of Equilibrium Solutions

The stability of an equilibrium solution $\mathbf{x_0}$ at $\mu = \mu_0$ depends on the eigenvalues of the Jacobian matrix $\mathbf{J}$ of the system (2.1), which is the matrix of first partial derivatives. Consider a small disturbance $\mathbf{y}$ to the equilibrium solution $\mathbf{x_0}$, so that

$$\mathbf{x(t)} = \mathbf{x_0} + \mathbf{y(t)}. \tag{2.3}$$

Substituting Eq. (2.3) into Eq. (2.1) gives

$$\dot{\mathbf{y}} = \mathbf{F}(\mathbf{x_0} + \mathbf{y}; \mu_0). \tag{2.4}$$

Using a Taylor series expansion around $\mathbf{x_0}$ and keeping only the linear terms in $\mathbf{y}$, one obtains

$$\dot{\mathbf{y}} = \mathbf{F}(\mathbf{x_0}; \mu_0) + \mathbf{D_x F}(\mathbf{x_0}; \mu_0) y + ... \tag{2.5}$$

However, at the equilibrium solution $\mathbf{x_0}$, $\mathbf{F}(\mathbf{x_0}; \mu_0) = 0$. So, Eq. (2.5) becomes

$$\dot{\mathbf{y}} \approx \mathbf{D_x F}(\mathbf{x_0}; \mu_0)\mathbf{y} = \mathbf{J}\mathbf{y} \tag{2.6}$$

The eigenvalues of the constant matrix J provide information about the local stability of the equilibrium solution $\mathbf{x_0}$. An equilibrium solution is classified as hyperbolic or non-hyperbolic. If all of the eigenvalues of J have nonzero real parts, then the corresponding equilibrium solution is called a hyperbolic fixed point; otherwise, it is called a nonhyperbolic fixed point. The hyperbolic fixed points are of three types: stable nodes, unstable nodes, and saddle points. A fixed point is called a stable node or a sink if all of the eigenvalues of J have negative real parts. If the matrix J associated with a stable node has complex eigenvalues, the stable node is also called a stable focus. An equilibrium point is called an unstable node or a source if one or more of the eigenvalues of J have positive real parts. An unstable node is called an unstable focus if the associated matrix J has complex eigenvalues.

An equilibrium point is a saddle if some, but not all, of the eigenvalues have positive real parts while the rest of them have negative real parts. On the other hand, a nonhyperbolic fixed point is unstable if one or more of the eigenvalues of J have positive real parts. It is said to be marginally stable if some of the eigenvalues of J have negative real parts while the rest of them have zero real parts. It is called a center if all the eigenvalues of J are purely imaginary and nonzero.

2.2 Bifurcation Theory

Bifurcation is a French word that has been introduced into nonlinear dynamics by Poincare. It is used to indicate a qualitative change in the dynamics of a system, such as the number and type of solutions under the variation of one or more parameters on which the system in question depends. In bifurcation problems, it is useful to consider a space formed by using the state variables and the control parameters, called the state-control space. In this space, locations at which bifurcations occur are called bifurcation points.

In this DISSERTATION, we are mainly concerned with local bifurcation of fixed points and limit cycles of an autonomous system of differential equations as a function of scalar control parameters.

2.2.1 Local Bifurcations of Fixed Points

Local bifurcation is a qualitative change occurring in the neighborhood of a fixed point or a periodic solution of the system. When a single control parameter is varied, a fixed point of an autonomous system, such as the one given by (2.1), can lose stability through one of the following bifurcations: saddle-node bifurcation, pitchfork bifurcation, transcritical bifurcation, and Hopf bifurcation.

At bifurcation points associated with saddle-node, pitchfork, and transcritical bifurcations, only branches of fixed points or static solutions meet. Hence, these three bifurcations

are classified as static bifurcations. In contrast, branches of fixed points and periodic solutions meet at a hopf bifurcation point. Hence, a Hopf bifurcation is classified as a dynamic bifurcation.

Let us now give the definition of a static and Hopf bifurcation. A static bifurcation of a fixed point of (2.1) occurs at a certain value of μ, say $\mu = \mu_0$, if the following conditions are satisfied:

1- $\mathbf{F}(\mathbf{x_0}; \mu_0) = \mathbf{0}$

2- The Jacobian matrix $\mathbf{D_x F}$ evaluated at $(\mathbf{x_0}; \mu_0)$ has a zero eigenvalue while all of its other eigenvalues have negative real parts.

It is clear that the first condition ensures that the considered solution is a fixed point of (2.1), while the second condition implies that this fixed point is a nonhyperbolic fixed point. One should note that these conditions are necessary but not sufficient.

A Hopf bifurcation of a fixed point of (2.1) occurs at a certain value of μ, say $\mu = \mu_0$, if the following conditions are satisfied:

1- $\mathbf{F}(\mathbf{x_0}; \mu_0) = \mathbf{0}$

2- The Jacobian matrix $\mathbf{D_x F}$ evaluated at $(\mathbf{x_0}; \mu_0)$ has a pair of purely imaginary eigenvalues $\pm j\omega$ while all of its other eigenvalues have negative real parts.

3- For $\mu = \mu_0$, let the analytic continuation of the pair of purley imaginary eigenvalues be $(\hat{\lambda} \pm j\omega)$. Then $\frac{d\hat{\lambda}}{d\mu} \neq 0$ at $\mu = \mu_0$.

The first two conditions imply that the fixed point undergoing the bifurcation is a nonhyperbolic fixed point. The third condition implies a transversal or nonzero speed crossing of the imaginary axis and, hence, it is called a transversality condition. When all of the above three conditions are satisfied, a periodic solution of period $(2\pi/\omega)$ may be born at $(\mathbf{x_0}; \mu_0)$.

2.2.2 Continuation Schemes

Continuation schemes are used to determine how solutions of (2.1) vary with a certain parameter. These schemes are based on the Implicit Function Theorem. There are two categories of continuation schemes. The first category consists of predictor-corrector methods, which approximately follow a branch of solutions. The second category consists of piecewise-linear or simplical methods, which exactly follow a piecewise-linear curve that approximates a branch of solutions.

Among the above two categories, there are many types of continuation methods, such as the sequential scheme, the Davidenko Newton-Raphson scheme, the arclength scheme, and the pseudo-arclength scheme. In the arclength scheme, the arclength s along a branch of solutions is used as the continuation parameter. So, $\mathbf{x}$ and μ are considered to be function of s; that is, $\mathbf{x} = \mathbf{x}(s)$ and $\mu = \mu(s)$. This parameterization is useful in carrying out a continuation along a path with a saddle-node bifurcation (turning point). On the path parameterized by the arclength s, we seek $\mathbf{x}$ and μ such that

$$\mathbf{F}(\mathbf{x}(s); \mu(s)) = \mathbf{0} \tag{2.7}$$

Thus, differentiating Eq. (2.7) with respect to s yields

$$\mathbf{F}_{\mathbf{x}}(\mathbf{x}; \mu)\mathbf{x}^{'} + \mathbf{F}_{\mu}(\mathbf{x}; \mu)\mu^{'} = \mathbf{0} \tag{2.8}$$

where $\mathbf{x}^{'} = \frac{d\mathbf{x}}{ds}$ and $\mu^{'} = \frac{d\mu}{ds}$. Hence, Eq. (2.8) can be rewritten as

$$[\mathbf{F}_{\mathbf{x}}|\mathbf{F}_{\mu}]\mathbf{t} = [\mathbf{F}_{\mathbf{x}}|\mathbf{F}_{\mu}][\mathbf{x}^{'}\mu^{'}]^{T} = \mathbf{0} \tag{2.9}$$

where the $(n+1)$ vector $\mathbf{t}$ is the tangent vector at $(\mathbf{x}; \mu)$ of the path. The system (2.8) consists of n linear algebraic equations in the $(n+1)$ unknowns $\mathbf{x}^{'}$ and $\mu^{'}$. To uniquely specify these unknowns, we supplement (2.7) with an inhomogeneous equation. A convenient additional equation is specified by the Euclidean arclength normalization defined as

$$\mathbf{x}'^{T}\mathbf{x}' + \mu'^{2} = 1 \tag{2.10}$$

The initial conditions for Eqs. (2.8) and (2.10) are given by $\mathbf{x} = \mathbf{x_0}$ and $\mu = \mu_0$ at $s = 0$. If the Jacobian matrix $\mathbf{F_x}$ is nonsingular and $\mathbf{F}_\mu$ is a zero vector, Eqs. (2.8) and (2.10) yield

$$[\mathbf{x}'^{T}\mu'] = \pm[0\ 0\ \ldots\ 0\ 1] \tag{2.11}$$

If $\mathbf{F_x}$ is nonsingular and $\mathbf{F}_\mu$ is a nonzero vector, one can solve Eqs. (2.8) and (2.10) to determine the tangent vector $\mathbf{t}$ as follows. First, solve the system of n linear algebraic equations

$$\mathbf{F_x}(\mathbf{x};\mu)\mathbf{Z} = -\mathbf{F}_\mu(\mathbf{x};\mu) \tag{2.12}$$

for the vector $\mathbf{Z}$. Then, owing to the linearity of Eq. (2.8) in $\mathbf{x}'$ and μ', we write

$$\mathbf{x}' = \mathbf{Z}\mu' \tag{2.13}$$

where μ' is still unknown. Substituting Eq. (2.13) into the arclength Eq. (2.10) yields

$$\mu' = \pm\frac{1}{\sqrt{(1 + \mathbf{Z}^T\mathbf{Z})}} \tag{2.14}$$

where the plus and minus signs determine the direction of the continuation. Having determined the tangent vector $\mathbf{t}$, we use it to predict the values of $\mathbf{x}$ and μ at $s = \Delta s$ according to $\mathbf{x} = \mathbf{x_0} + \mathbf{x}'\Delta s$ and $\mu = \mu_0 + \mu'\Delta s$. These predicted values can be corrected by using a Newton-Raphson procedure, and the predictor-corrector scheme is continued until the branch is traced. The choice of the step size Δs should be such that the initial guess or estimate is within the radius of convergence of the corrector. The step size may have to be adaptively varied during the continuation.

2.2.3 The Normal Form Near a Hopf Bifurcation Point

To determine the normal form of Eq. (2.1) near a Hopf bifurcation value H_i, we let

$$\mathbf{x} - \mathbf{x}_0 = \epsilon \mathbf{y} \text{ and } \mu - H_i = \epsilon^2 \hat{\mu} \tag{2.15}$$

where $\mathbf{x}_0$ is the fixed point at H_i and ϵ is a small dimensionless parameter that is used as a bookkeeping device. Substituting Eq. (2.15) into Eq. (2.1) and expanding the result for small ϵ, we obtain

$$\dot{\mathbf{y}} = J\mathbf{y} + \epsilon \mathbf{Q}(\mathbf{y}, \mathbf{y}) + \epsilon^2 \mathbf{C}(\mathbf{y}, \mathbf{y}, \mathbf{y}) + \epsilon^2 \hat{\mu} B \mathbf{y} + \cdots \tag{2.16}$$

Here J is the $n \times n$ Jacobian matrix of $\mathbf{F}$ evaluated at $(\mathbf{x}_0, H_i)$, B is a $n \times n$ constant matrix, $\mathbf{Q}(\mathbf{y}, \mathbf{y})$ is generated by a vector-valued symmetric bilinear form $\mathbf{Q}(\mathbf{u}, \mathbf{v})$, and $\mathbf{C}(\mathbf{y}, \mathbf{y}, \mathbf{y})$ is generated by a vector-valued symmetric trilinear form $\mathbf{C}(\mathbf{u}, \mathbf{v}, \mathbf{w})$. At $\mu = H_i$, J has a pair of purely imaginary eigenvalues $\pm j\omega$ with the remaining eigenvalues in the left-half plane. Using the method of multiple scales [31 and 32], we seek a third-order expansion in the form

$$\mathbf{y}(t; \epsilon) = \mathbf{y}(T_0, \tau_2) + \epsilon \mathbf{y}_2(T_0, \tau_2) + \epsilon^2 \mathbf{y}_3(T_0, \tau_2) + \cdots \tag{2.17}$$

where $T_0 = t$ and $\tau_2 = \epsilon^2 t$. Substituting Eq. (2.17) into Eq. (2.16) and equating coefficients of like powers of ϵ, we obtain equations governing $\mathbf{y}_1, \mathbf{y}_2$, and $\mathbf{y}_3$. The non-decaying solution of $\mathbf{y}_1$ is written as

$$\mathbf{y}_1 = A(\tau_2)\mathbf{p}e^{j\omega T_0} + \bar{A}(\tau_2)\bar{\mathbf{p}}e^{-j\omega T_0} \tag{2.18}$$

where $\mathbf{p}$ is the right eigenvector of J corresponding to the eigenvalue $j\omega$. Then, the solution of the second-order problem is expressed as

$$\mathbf{y}_2 = 2\mathbf{z}_0 A\bar{A} + 2\mathbf{z}_2 A^2 e^{2j\omega T_0} + cc \tag{2.19}$$

where cc is the complex conjugate of the preceding terms and $\mathbf{z}_0$ and $\mathbf{z}_2$ are the solutions of the algebraic systems of equations

$$J\mathbf{z}_0 = -\frac{1}{2}\mathbf{Q}(\mathbf{p}, \mathbf{p}) \tag{2.20}$$

$$(2j\omega - J)\mathbf{z}_2 = \frac{1}{2}\mathbf{Q}(\mathbf{p}, \mathbf{p}) \tag{2.21}$$

Finally, eliminating the secular terms from $\mathbf{y}_3$ yields

$$A' = \mu(\beta_1 + j\beta_3)A + 4(\beta_2 + j\beta_4)A^2\bar{A} \tag{2.22}$$

where

$$\beta_1 + j\beta_3 = \mathbf{q}^T B\mathbf{p} \tag{2.23}$$

$$\beta_2 + j\beta_4 = 2\mathbf{q}^T\mathbf{Q}(\mathbf{p}, \mathbf{z}_0) + \mathbf{q}^T\mathbf{Q}(\bar{\mathbf{p}}, \mathbf{z}_2) + \frac{3}{4}\mathbf{q}^T\mathbf{C}(\mathbf{p}, \mathbf{p}, \bar{\mathbf{p}}) \tag{2.24}$$

and $\mathbf{q}$ is the left eigenvector of J corresponding to the eigenvalue $j\omega$. It is normalized so that $\mathbf{q}^T\mathbf{p} = 1$. Letting $A = \frac{1}{2}a\exp(j\theta)$ and separating real and imaginary parts, we find that the real part is given by

$$a' = (\mu - H_i)\beta_1 a + \beta_2 a^3 \tag{2.25}$$

2.2.4 Floquet Theory

To study the stability of a periodic solution $\mathbf{X}(t)$ of least period T of the system of n autonomous first-order nonlinear equations (2.1), we let

$$\mathbf{X}(t) = \mathbf{X}(t) + \mathbf{u}(t) \tag{2.26}$$

Substituting (2.26) into (2.1) and linearizing in $\mathbf{u}(t)$ leads to

$$\dot{\mathbf{u}} = D_{\mathbf{x}}\mathbf{F}(\mathbf{X}; \mu)\mathbf{u} \tag{2.27}$$

where $D_{\mathbf{x}}\mathbf{F}(\mathbf{X}; \mu)$ is the Jacobian matrix of $\mathbf{F}$ evaluated at $\mathbf{x} = \mathbf{X}$. Then, we solve the linear system of equations (2.27) to determine n linearly independent solutions $\mathbf{u}_1, \mathbf{u}_2, \cdots, \mathbf{u}_n$ and form the fundamental matrix

$$U = [\mathbf{u}_1 \;\; \mathbf{u}_2 \;\; \cdots \;\; \mathbf{u}_n] \tag{2.28}$$

Usually, one chooses the initial conditions such that

$$U(0) = I \tag{2.29}$$

where I is the $n \times n$ identify matrix. Then, the stability of $\mathbf{X}(t)$ is ascertained from the eigenvalues $\rho_1, \rho_2, \cdots, \rho_n$ of the so-called monodromy matrix $U(T)$. These eigenvalues are called the Floquet multipliers. One of these multipliers is always unity for an autonomous system [19]. If all of the other multipliers are inside the unit circle in the complex plane, the limit cycle $\mathbf{X}(t)$ is stable; otherwise, it is unstable.

2.2.5 Local Bifurcations of Periodic Solutions

When a single control parameter varies, a periodic solution of an autonomous system, such as the one given by Eq. (2.1), can lose stability through one of the following bifurcations: transcritical, symmetry-breaking, cyclic-fold, period doubling, and secondary Hopf bifurcations. The resulting solution depends on how the Floquet multipliers leave the unit circle. There are three possible scenarios. First, a Floquet multiplier leaves the unit circle along the real axis through $+1$, resulting in either a trancritical, or a symmetry-breaking, or a cyclic-fold bifurcation. At a cyclic-fold bifurcation, stable limit cycle collides with an unstable limit cycle, resulting in their annihilation. In a transcritical bifurcation, two branches of stable and unstable cycles coexist below the bifurcation value and exchange stability after the bifurcation. In a symmetry-breaking bifurcation, the symmetry of the limit cycle is broken. At such a bifurcation, a branch of symmetric limit cycles meets branches of asymmetric limit cycles.

Second, a Floquet multiplier leaves the unit circle through -1, resulting in a period-doubling bifurcation. A branch of stable limit cycles that exist before the bifurcation μ_c continues as unstable branch of limit cycles after μ_c. If the bifurcation is supercritical, a new branch of stable period-doubled solutions is created. If the point is subcritical, a branch of unstable period-doubled solutions is destroyed.

Third, two complex conjugate Floquet multipliers leave the unit circle away from the real axis, resulting in a secondary Hopf or Neimark bifurcation. As mentioned earlier, the Hopf bifurcation of a fixed point of an autonomous system, such as the one given by Eq. (2.1), leads to a periodic solution of this system. In other words, the Hopf bifurcation

introduces a new frequency to the system in addition to the first one. The Hopf bifurcation of a periodic solution, called secondary Hopf bifurcation, produces either a periodic or a two-period quasiperiodic solution, depending on whether the two frequencies are commensurate or not.

Chapter 3

ON THE EFFECT OF DAMPER WINDINGS

In this chapter, we analyze the effect of damper windings on subsynchronous resonance of a practical power system model by using the methods of modern nonlinear dynamics. The choosen model is the BOARDMAN generator. We have revealed the existence of complex self-excited oscillations of the turbine-generator rotor, such as limit cycles and two-period quasiperiodic attractors for practical compensation values. We have shown that they result from a strong interaction of the subsynchronous electrical mode with one of the torsional modes. For high compensation values, they may induce loss of synchronism of the generator following the disappearance of the two-period quasiperiodic attractor and its basin of attraction in a bluesky catastrophe.

3.1 System Description

We consider the single-machine-infinite-busbar (SMIB) power system shown in Fig. 3.1. The model and parameters are chosen to represent characteristics of the BOARDMAN generator with respect to the rest of the North-Western American Power System when the generator is heavily loaded. The system is governed by 17 first-order nonlinear ordinary-differential equations, 7 of which represent the electrical subsystem and 10 represent the mechanical system.

The latter consist of a high-pressure (HP), an intermediate-pressure (IP), and a low-pressure (LP) turbine section, a generator, and an exciter, all mounted on the same shaft, as indicated in Fig. 3.1.

We neglect the dynamics of the automatic voltage regular (AVR) and the turbine gov-

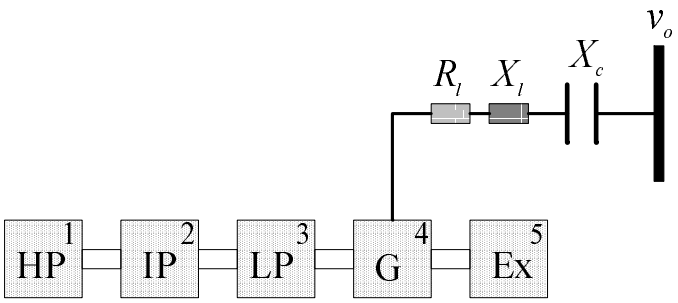

Figure 3.1: A schematic diagram for a series capacitor-compensated single machine power system. The mechanical system consists of a high-pressure (HP), an intermediate-pressure (IP), and a low-pressure (LP) turbine section, a generator (G), and an exciter (Ex).

ernor and include the dynamics of the damper windings on the q-and d-axes. Using the direct and quadrature $d-q$ axes and Park's transformation, one can write the equations describing the system as follows [14]:

(a) Machine:

$$\frac{d\psi_d}{dt} = \omega_b \left(v_d + R_a i_d + \omega_r \psi_q\right) \tag{3.1}$$

$$\frac{d\psi_q}{dt} = \omega_b \left(v_q + R_a i_q - \omega_r \psi_d\right) \tag{3.2}$$

$$\frac{d\psi_f}{dt} = \omega_b \left(v_f - R_f i_f\right) \tag{3.3}$$

$$\frac{d\psi_Q}{dt} = \omega_b \left(-R_Q i_Q\right) \tag{3.4}$$

$$\frac{d\psi_D}{dt} = \omega_b \left(-R_D i_D\right) \tag{3.5}$$

(b) Flux linkages in the $d-q$ axes:

$$\psi_d = -X_d i_d + X_{md} i_f + X_{md} i_D \tag{3.6}$$

$$\psi_q = -X_q i_q + X_{mq} i_Q \tag{3.7}$$

$$\psi_f = -X_{md} i_d + X_f i_f + X_{md} i_D \tag{3.8}$$

$$\psi_Q = -X_{mq} i_q + X_Q i_Q \tag{3.9}$$

$$\psi_D = -X_{md} i_d + X_{md} i_f + X_D i_D \tag{3.10}$$

(c) Voltage drop across $R_a + jX_\ell$:

$$v_d = R_\ell i_d - X_\ell i_q + \frac{X_\ell}{\omega_b}\frac{di_d}{dt} + e_{cd} + v_{od} \tag{3.11}$$

$$v_q = R_\ell i_q + X_\ell i_d + \frac{X_\ell}{\omega_b}\frac{di_q}{dt} + e_{cq} + v_{oq} \tag{3.12}$$

$$v_{od} = v_0 \sin\delta_r \tag{3.13}$$

$$v_{oq} = v_0 \cos\delta_r \tag{3.14}$$

(d) Voltage drop across X_c:

$$\frac{de_{cd}}{dt} = \omega_b \left(X_c i_d + e_{cq}\right) \tag{3.15}$$

$$\frac{de_{cq}}{dt} = \omega_b \left(X_c i_q - e_{cd}\right) \tag{3.16}$$

(e) High-pressure turbine:

$$\frac{d\omega_1}{dt} = \frac{1}{M_1}\left[-D_1(\omega_1 - 1) - K_{12}\left(\theta_1 - \theta_2\right)\right] \tag{3.17}$$

$$\frac{d\theta_1}{dt} = \omega_b(\omega_1 - 1) \tag{3.18}$$

(f) Medium-pressure turbine:

$$\frac{d\omega_2}{dt} = \frac{1}{M_2}\left[-D_2(\omega_2 - 1) + K_{12}\left(\theta_1 - \theta_2\right) - K_{23}\left(\theta_2 - \theta_3\right)\right] \tag{3.19}$$

$$\frac{d\theta_2}{dt} = \omega_b(\omega_2 - 1) \tag{3.20}$$

(g) Low-pressure turbine:

$$\frac{d\omega_3}{dt} = \frac{1}{M_3}\left[-D_3(\omega_3 - 1) + K_{23}\left(\theta_2 - \theta_3\right) - K_{34}\left(\theta_3 - \delta_r\right)\right] \tag{3.21}$$

$$\frac{d\theta_3}{dt} = \omega_b(\omega_3 - 1) \tag{3.22}$$

(h) Generator:

$$\frac{d\omega_r}{dt} = \frac{1}{M}\left[T_m - T_e + K_{34}(\theta_3 - \delta_r) - K_{45}(\delta_r - \theta_5) - D_r(\omega_r - 1)\right] \tag{3.23}$$

$$\frac{d\delta_r}{dt} = \omega_b(\omega_r - 1) \tag{3.24}$$

(i) Exciter:

$$\frac{d\omega_5}{dt} = \frac{1}{M_5}\left[-D_5(\omega_5 - 1) + K_{45}\left(\delta_r - \theta_5\right)\right] \tag{3.25}$$

$$\frac{d\theta_5}{dt} = \omega_b(\omega_5 - 1) \tag{3.26}$$

where

$$T_e = i_q\psi_d - i_d\psi_q$$

Equations (3.1)-(3.14) can be combined into

$$\begin{aligned} -(X_\ell + X_d)\frac{di_d}{dt} + X_{md}\frac{di_f}{dt} + X_{md}\frac{di_D}{dt} = \omega_b\left[(R_\ell + R_a)i_d\right. \\ \left. -(X_\ell + \omega_r X_q)i_q + \omega_r X_{mq} i_Q + e_{cd} + v_0 \sin\delta_r\right] \end{aligned} \tag{3.27}$$

$$-(X_\ell + X_q)\frac{di_q}{dt} + X_{mq}\frac{di_Q}{dt} = \omega_b\left[(X_\ell + \omega_r X_d)i_d + (R_\ell + R_a)i_q - \omega_r X_{md} i_f + \omega_r X_{md} i_D + e_{cq} + v_0 \cos\delta_r\right] \tag{3.28}$$

$$-X_{md}\frac{di_d}{dt} + X_f\frac{di_f}{dt} + X_{md}\frac{di_D}{dt} = \omega_b\left[-R_f i_f + \frac{R_f E_{fd}}{X_{md}}\right] \tag{3.29}$$

$$-X_{mq}\frac{di_q}{dt} + X_Q\frac{di_Q}{dt} = -\omega_b R_Q i_Q \tag{3.30}$$

$$-X_{md}\frac{di_d}{dt} + X_{md}\frac{di_f}{dt} + X_D\frac{di_D}{dt} = -\omega_b R_D i_D \tag{3.31}$$

where $v_f = R_f E_{ed}/X_{md}$. Using Eqs. (3.6) and (3.7), we express T_e as

$$T_e = (X_q - X_d)\, i_d i_q + X_{md} i_f i_q - X_{mq} i_Q i_d + X_{md} i_D i_q \tag{3.32}$$

Equations (3.15)-(3.31) constitute a system of 17 first-order nonlinear ordinary-differential equations describing the dynamics of the SMIB power system shown in Fig. 3.1. The 17 state variables of the system are i_d, i_q, i_f, i_Q, i_D, e_{cd}, e_{cq}, ω_1, θ_1, ω_2, θ_2, ω_3, θ_3, ω_r, δ_r, ω_5, and θ_5. The parameters used in this study are the same as those used by Zhu [18] and Zhu et al. [20] in the absence of damper windings. The parameters in p.u. for the generator and the line are

$$\begin{aligned}
&X_{md} = 1.66, \quad X_d = 1.79, \quad X_q = 1.71, \quad X_f = 1.70,\\
&X_{mq} = 1.58, \quad X_D = 1.666, \quad X_Q = 1.696, \quad R_f = 0.01,\\
&R_D = 0.0037, \quad R_a = 0.015, \quad X_\ell = 0.30,\\
&R_\ell = 0.0165, \quad R_Q = 0.006.
\end{aligned}$$

The mechanical inertias, stiffnesses and damping coefficients in p.u. are

$$\begin{aligned}
&D_1 = 0.518, \quad M_1 = 0.6695\\
&D_2 = 0.224, \quad M_2 = 1.4612, \quad K_{12} = 33.07\\
&D_3 = 0.224, \quad M_3 = 1.6307, \quad K_{23} = 28.59\\
&D_4 = 0.000, \quad M_4 = 1.5228, \quad K_{34} = 44.68
\end{aligned}$$

$$D_5 = 0.145, \quad M_5 = 0.0903, \quad K_{45} = 21.98$$

The control parameters in this study are

$$T_m, \quad E_{fd}, \quad v_0, \quad \text{and} \quad \mu = X_c/X_\ell$$

3.2 The Case of No Damper Windings

To cancel the effect of the damper windings, we set $i_Q = i_D = 0$ in Eqs. (3.27) and (3.28). Then, the dynamics of the system are governed by Eqs. (3.15)-(3.29). This case was treated by Zhu [18] and Zhu et al. [20] and is analyzed next.

3.2.1 Operating Conditions and their Stability

The operating conditions (equilibrium solutions or points) can be obtained by setting the derivatives of the state variables in the system of equations (3.15)-(3.29) equal to zero. The result is

$$(R_\ell + R_a)i_d - (X_\ell + X_q)i_q + e_{cd} + v_0 \sin\delta_r = 0 \tag{3.33}$$

$$(X_\ell + X_d)i_d + (R_\ell + R_a)i_q - X_{md}i_f + e_{cq} + v_0 \cos\delta_r = 0 \tag{3.34}$$

$$E_{fd} = X_{md}i_f \tag{3.35}$$

$$e_{cd} = X_c i_q \tag{3.36}$$

$$e_{cq} = -X_c i_d \tag{3.37}$$

$$T_m = (X_q - X_d)i_d i_q + X_{md}i_q i_f \tag{3.38}$$

$$\omega_r = \omega_1 = \omega_2 = \omega_3 = \omega_5 = 1 \tag{3.39}$$

$$\delta_r = \theta_1 = \theta_2 = \theta_3 = \theta_5 \tag{3.40}$$

Instead of specifying T_m, E_{fd}, and v_0, one usually specifies the real P_e and reactive Q_e powers and the terminal voltage v_t of the generator. In p.u., these control parameters are related to the voltages and currents through

$$P_e = v_d i_d + v_q i_q \tag{3.41}$$

$$Q_e = v_q i_d - v_d i_q \tag{3.42}$$

$$v_t^2 = v_d^2 + v_q^2 \tag{3.43}$$

To relate the voltages v_d and v_q to the currents i_d, i_q, and i_f, we note that, at the operating condition, Eqs. (3.1) and (3.2) reduce to

$$v_d = -R_a i_d - \psi_q \tag{3.44}$$

$$v_q = -R_a i_q + \psi_d \tag{3.45}$$

Using Eqs. (3.6) and (3.7) to eliminate ψ_d and ψ_q from Eqs. (3.44) and (3.45) yields

$$v_d = -R_a i_d + X_q i_q \tag{3.46}$$

$$v_q = -R_a i_q - X_d i_d + X_{md} i_f \tag{3.47}$$

Given P_e, Q_e, v_t, and $\mu = X_c/X_\ell$, we solve the algebraic system of nine equations (3.33), (3.34), (3.36), (3.37), (3.41)-(3.43), (3.46), and (3.47) to determine the eight state variables i_d, i_q, i_f, e_{cd}, e_{cq}, v_d, v_q, and δ_r and the control parameter v_0. Then, we calculate E_{fd} and T_m from Eqs. (3.35) and (3.38), thereby determining the operating condition and the control parameters v_0, E_{fd}, and T_m. Using an arclength continuation scheme [30], we calculate variation of the operating condition (equilibrium point) with the control parameter μ.

The stability of a given equilibrium point is ascertained by examination of the eigenvalues of the Jacobian matrix J of equations (3.15)-(3.29) evaluated at the equilibrium point. The equilibrium point is asymptotically stable if all of the eigenvalues of the Jacobian matrix lie in the left-half of the complex plane and unstable if at least one eigenvalue lies in the right-half of the complex plane.

Because the 15 x 15 Jacobian matrix of the system is real, it has one real eigenvalue, which is negative and corresponds to the field windings, and 7 pairs of complex conjugate eigenvalues, yielding 7 modes of oscillation. Two of them are associated with the electrical system and 5 with the mechanical system. In the sequel, they will be referred to as electrical and mechanical modes, respectively. The mechanical mode with the lowest frequency, 2.0

Hz, is the mode usually considered in power-system stability analysis. It is called the swing or electro-mechanical mode because the turbine sections, generator, and exciter oscillate together as a rigid body. As for the other 4 mechanical modes, they are called torsional modes to indicate that some of the shaft masses oscillate against the others, as seen in Fig. 3.2. For example, let us study the second and third torsional modes. They are of special interest because, under certain conditions described below, they may be self-excited when they interact with one of the electrical modes. The second torsional mode has a natural frequency of 24.5 Hz and one polarity reversal located between the LP turbine section and the generator. On the other hand, the third torsional mode has a natural frequency of 28.7 Hz and three polarity reversals, one between each pair of masses except between the HP and IP turbine sections. Obviously, these oscillatory modes are extremely dangerous when excited because they will cause loss of fatigue life and eventually the destruction of the rotor, even if they have small amplitudes (see Kundur [33, pp. 1061-1065], for more details.) Consequently, they should be detected at the incipient level and damped off by an appropriate control action.

To study how these oscillatory modes interact with each other, let us analyze variation of the real and imaginary parts of the eigenvalues with the compensation level μ, which are displayed in Fig. 3.3. They have been calculated for $P_e = 0.876$, $Q_e = -0.115$, and $v_t = 1.09$. For small μ, the frequencies of the electrical modes are approximately 377 rad/sec, but as μ increases, they separate from each other. One of them increases and is called supersynchronous and the other one decreases and is called subsynchronous. The supersynchronous mode is highly damped and hence its real part does not show up in Fig. 3.3(b). Here, we are interested in the subsynchronous frequency and how its associated mode interacts with the torsional modes.

We observe from Fig. 3.3(a) that the frequency of the subsynchronous electrical mode intersects that of the fourth torsional mode at approximately 313rad/ses and $\mu \approx 0.072$. This causes the associated eigenvalue to move closer to the imaginary axis of the complex plane, but not enough to cross it, as evident in Fig. 3.3(b). Consequently, the fourth

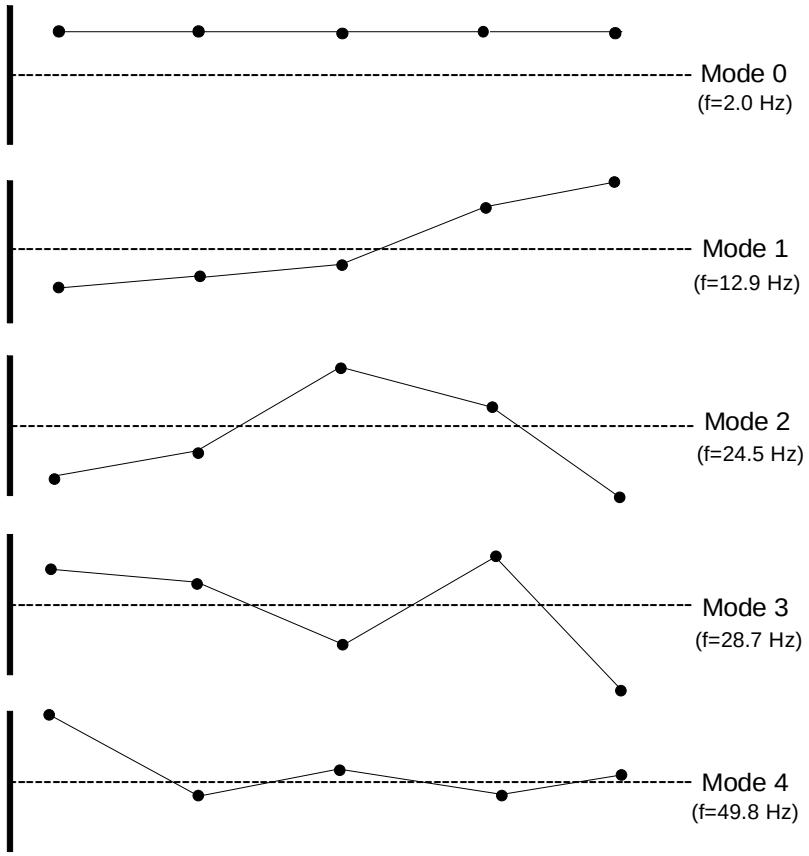

Figure 3.2: Mode shapes of the five-mass-turbine-generator system.

torsional mode does not lose stability. As μ increases further, the frequency of the electrical mode continues to decrease away from that of the fourth torsional mode while approaching that of the third torsional mode. The latter is finally crossed at $\mu \approx 0.61859$. As seen in Fig. 3.3(b), the eigenvalue of the fourth torsional mode moves to the left, away from the imaginary axis, until the influence of the electrical mode on the fourth torsional mode becomes insignificant. On the other hand, the influence of the electrical mode on the third torsional mode gains sufficient strength to move its eigenvalue transversely across the imaginary axis into the right-half of the complex plane. The crossing occurs at $\mu = H_1 \approx 0.618592$, a value termed Hopf bifurcation. There, the third torsional mode loses stability. This mode regains stability at a reverse Hopf bifurcation, namely $\mu = H_2 \approx 0.724331$, where the frequencies of both modes start to separate from each other.

As μ passes H_2, the frequency of the electrical mode continues its descent toward now that of the second torsional mode. When the frequency of the electrical mode attains approximately 154 rad/sec, it intersects that of the second torsional mode at $\mu \approx 0.771$, which causes, this time, the eigenvalue of the subsynchronous electrical mode to move to the right. The interaction between these two modes is strong enough to cause the eigenvalue of the electrical mode to cross transversely the imaginary axis into the right-half of the complex plane at a third Hopf bifurcation point, namely $\mu = H_3 \approx 0.745988$. Beyond that point, the eigenvalue of the electrical mode steadily heads to the right and the power system never regains stability. It has no stable operating condition.

A synthetic view of the loci of the stable and unstable equilibria in the $\delta_r - \mu$ plane together with the three Hopf bifurcation points is depicted in Fig. 3.4. We observe that the equilibria are stable and hence all of the modes are positively damped to the left of H_1 and between H_2 and H_3. The equilibria are unstable between H_1 and H_2 and beyond H_3. For the $H_1 - H_2$ portion of the unstable locus, the second torsional mode is unstable, whereas, for the portion to the right of H_3, the subsynchronous electrical mode is unstable.

Figure 3.5 displays variation of the loci of the Hopf bifurcation points in the $P_e - \mu$ plane for $v_t = 1.09$ and $Q_e =$ -0.2. We observe that the first two Hopf bifurcations are insensitive

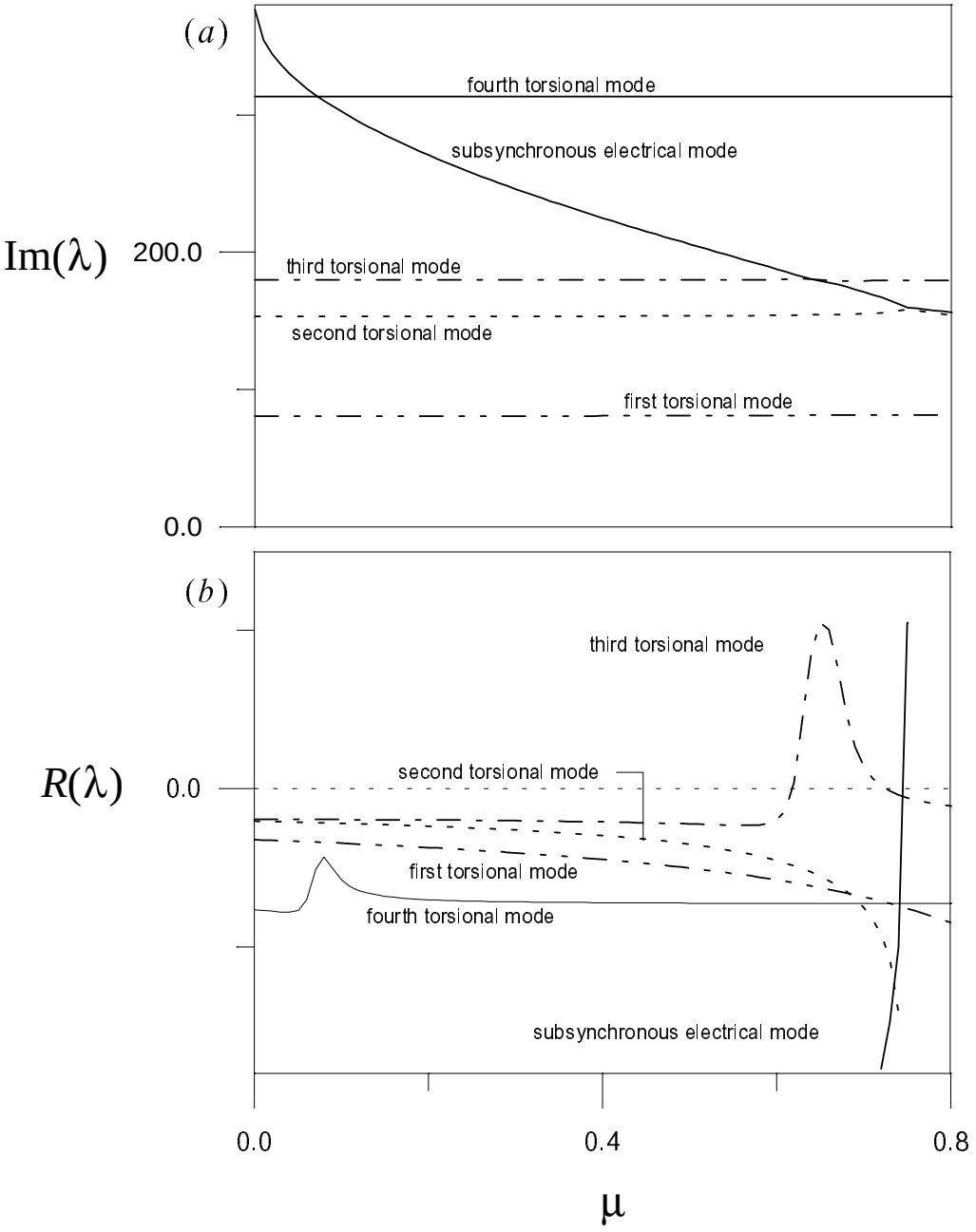

Figure 3.3: Variation of the real parts (a) and imaginary parts (b) of the eigenvalues for $P_e = 0.876$, Q_e = -0.115, and $v_t = 1.09$. There are three supercritical Hopf bifurcations at $\mu = H_1 \approx 0.618592$, $H_2 \approx 0.724331$, and $H_3 \approx 0.745988$.

to the value of P_e, whereas the third Hopf bifurcation increases slightly as P_e decreases. The question that arises here is how these loci vary in the $P_e - \mu$ plane as Q_e increases while v_t is kept constant at 1.09. We see in Fig. 3.6 that their variations widen the stability region and move the unstable region to higher values of μ, as expected. We note that all of the modes are stable to the left of the curve labeled H_1 and between the curves labeled H_2 and H_3, whereas the second torsional mode and the electrical subsynchronous mode are unstable between the curves labeled H_1 and H_2 and to the right of the curve labeled H_3, respectively.

3.2.2 Dynamic Solutions

According to the Hopf bifurcation theorem, the power system possesses small limit cycles near the Hopf bifurcation points. To investigate the stability of these limit cycles, we determine the normal forms of the Hopf bifurcations near curves H_1, H_2, and H_3. To this end, we use the multiple-scales algorithm outlined by Nayfeh and Balachandran [30] and encoded in MAPLE. It yields the normal form of a Hopf bifurcation for any first-order system of nonlinear ordinary-differential equations. For the case depicted in Fig. 3.4 for which $P_e = 0.876$, Q_e = -0.115, and $v_t = 1.09$, variation of the amplitude a of oscillations with time near a Hopf bifurcation H_i is given by

$$a' = (\mu - H_i)\beta_1 a + \beta_2 a^3 \tag{3.48}$$

In the vicinity of the first Hopf bifurcation $H_1 \approx 0.618592$, we find that $\beta_1 = 25.3281$ and β_2 = - 0.01339. Because $\beta_2 < 0$, we conclude that H_1 is supercritical and the limit cycles born as a result of the bifurcation are stable. Their amplitudes are given by

$$a = 43.4922\sqrt{\mu - H_1} \tag{3.49}$$

Similar results are obtained in the vicinity of the second Hopf bifurcation $H_2 \approx 0.618592$ with β_1 = -3.42 and β_2 = - 0.002134, and the third Hopf bifurcation $H_3 \approx 0.745988$ with $\beta_1 = 290.373$ and β_2 = -0.412849. Again, because $\beta_2 < 0$ for both Hopf bifurcations, H_2

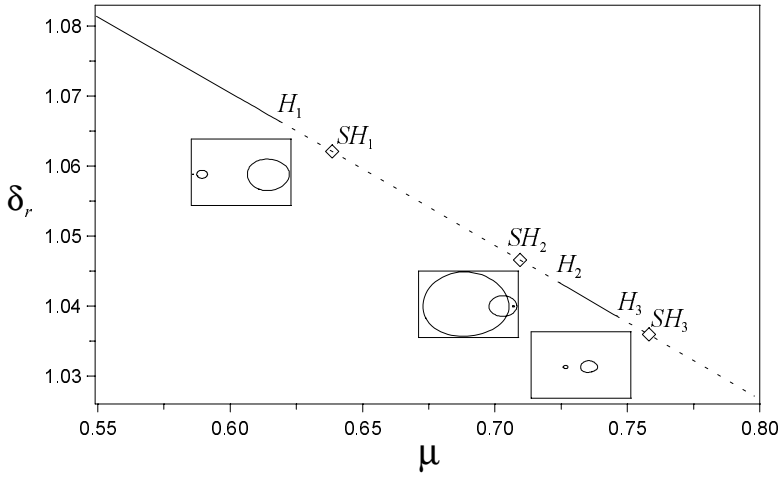

Figure 3.4: Bifurcation diagram showing variation of the generator rotor angle δ_r with the compensation level μ. The solid lines denote sinks and the dashed lines denote unstable foci.

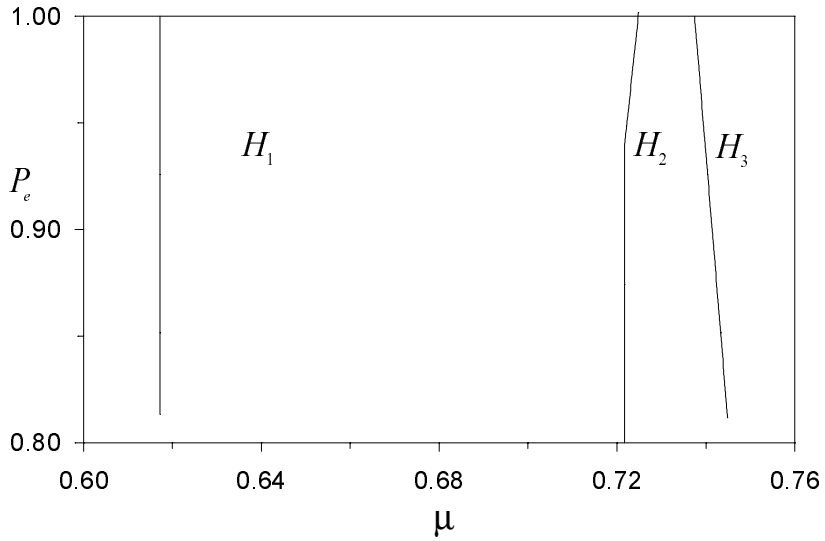

Figure 3.5: Variation of the loci of the Hopf bifurcation points with P_e when $v_t = 1.09$ and $Q_e = -0.2$.

and H_3 are supercritical and the created limit cycles are stable with amplitudes given by $a = 40.0328\sqrt{H_2 - \mu}$ and $a = 26.5205\sqrt{\mu - H_3}$, respectively.

Let us now study by means of a combination of a two-point boundary-value scheme and Floquet theory [30] the growth and stability of the limit cycles when μ moves away from the Hopf bifurcations inside the unstable region. As μ increases from H_1, the limit cycle grows in size while remaining stable with one Floquet multiplier being unity and the 14 remaining Floquet multipliers lying inside the unit circle. See Fig. 3.7(a) for an example of a limit cycle and Fig. 3.8(a) for the corresponding time history of the generator rotor angle δ_r and frequency ω_r. The time traces are periodic, the trajectory closes on itself, the Poincaré section consists of a single point, and the FFT consists of a single frequency and its harmonics.

When μ passes the critical value $SH_1 \approx 0.63848$, two of the Floquet multipliers exit the unit circle away from the real axis, signifying that SH_1 is a secondary Hopf bifurcation. There, the limit cycle loses stability and gives way to a two-period quasiperiodic (two-torus) attractor. Two examples are displayed in Figs. 3.7(b) and (c). The corresponding time histories are given in Fig. 3.8(b) and (c). The time traces are modulated, the trajectories do not close on themselves, the Poincaré sections consist of closed curves, and the FFTs consist of two incommensurate frequencies, their multiples, and combinations.

As μ increases slightly above SH_1 to $C_1 \approx 0.63868$, the two-torus collides with its basin boundary, yielding their destruction in a bluesky catastrophe. This can be observed in Fig. 3.9, which displays the time histories of δ_r and ω_r in the vicinity of the bluesky catastrophe. We note that, when the basin of attraction disappears at C_1, the generator angle δ_r steadily decreases from 19 to settle for a while at -548 and move again to another value, and so forth, indicating that the generator is unable to regain synchronism. Similar results are obtained when μ decreases below $SH_2 \approx 0.70193$ to $C_2 \approx 0.70015$ or increases beyond $SH_3 \approx 0.75799$ to $C_3 \approx 0.76505$. Again, at C_2 and C_3, there are no stable operating conditions.

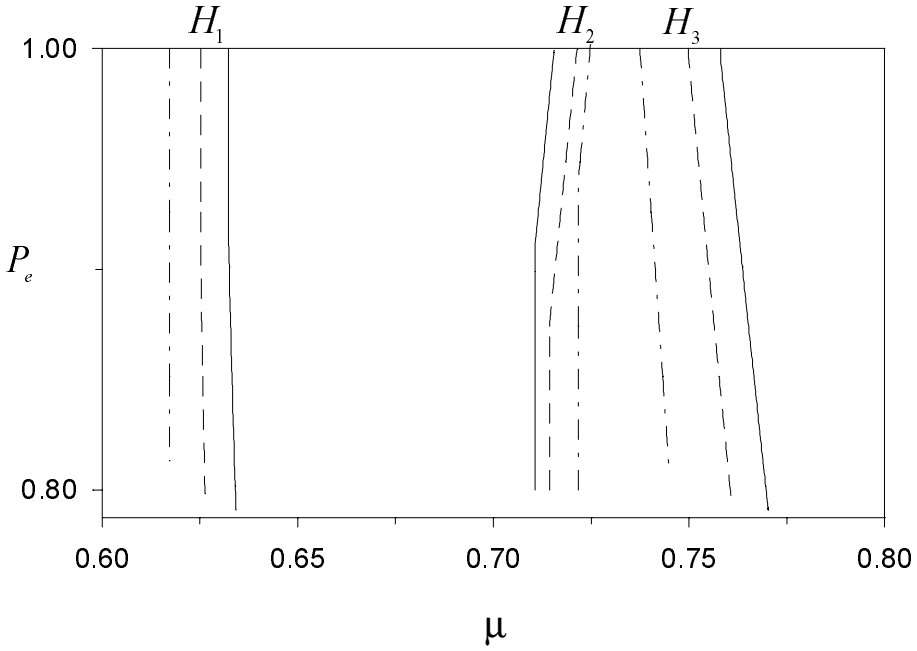

Figure 3.6: The influence of varying Q_e on the locations of the Hopf bifurcations in the $P_e - \mu$ plane for $v_t = 1.09$. The solid lines correspond to $Q_e = 0.45$, the dashed lines correspond to $Q_e = 0.15$, and the dashed-dotted lines correspond to $Q_e = -0.2$.

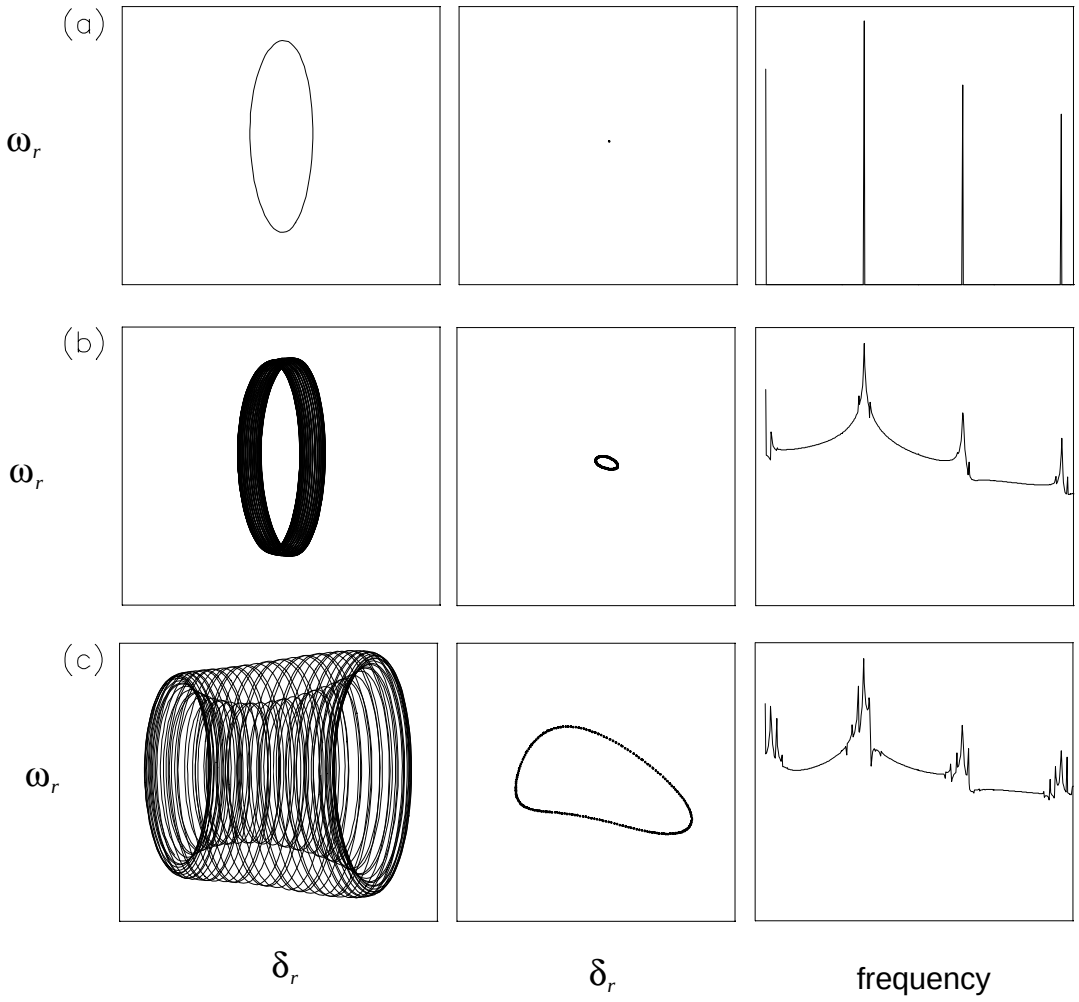

Figure 3.7: Two-dimensional projections of the phase portrait (left) and the Poincaré section (middle) onto the $\omega_r - \delta_r$ plane and the FFT of the corresponding quadrature-axis voltage e_{cq} across the capacitor (right) for μ = (a) 0.63840, (b) 0.63848, and (c) 0.63867. The solution at (a) is a limit cycle, at (b) is a two-torus attractor recorded well before the bluesky catastrophe, and at (c) is a two-torus attractor located just before it disappears in a bluesky catastrophe.

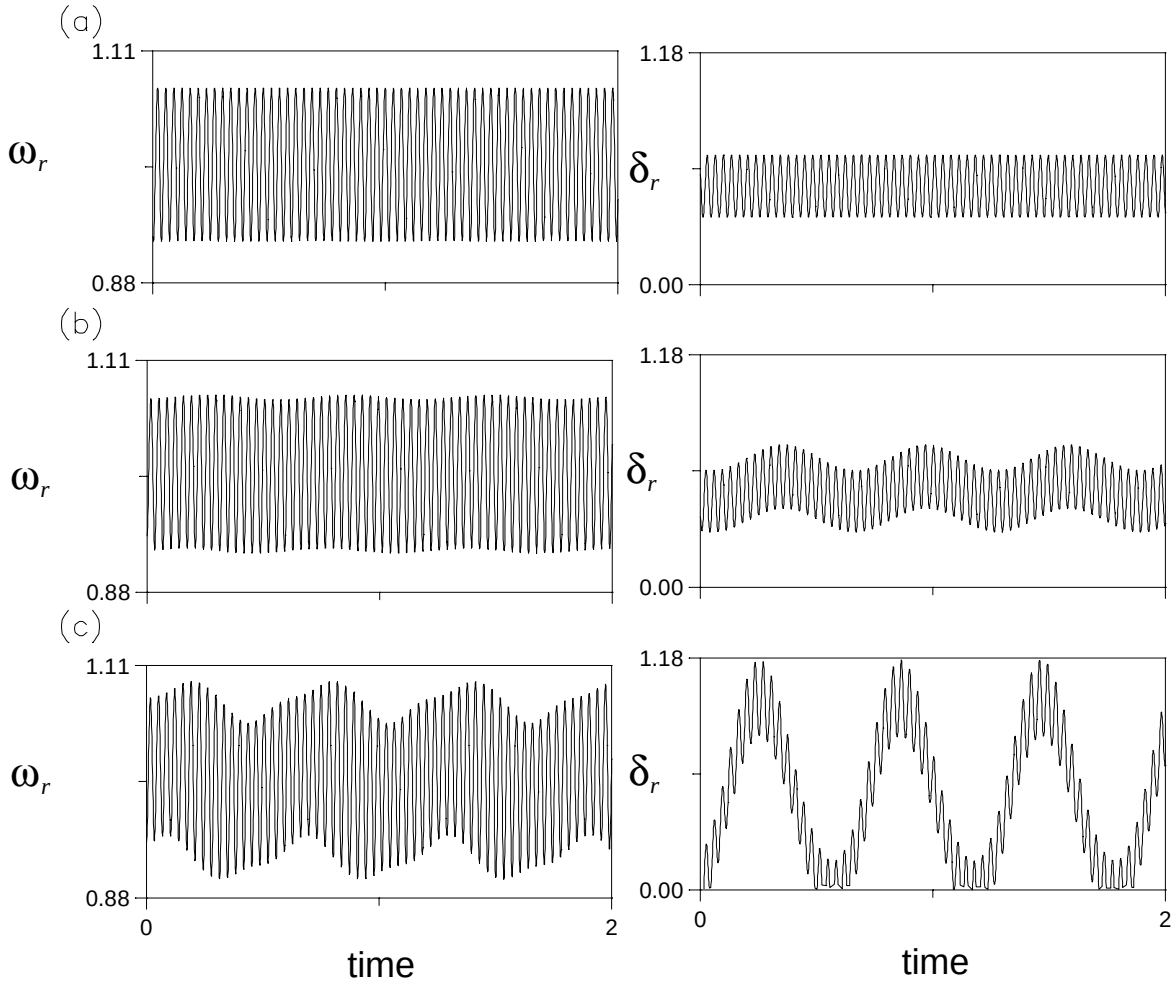

Figure 3.8: Time traces of the generator rotor angle δ_r and frequency ω_r at $\mu =$ (a) 0.63840, (b) 0.63848, and (c) 0.63867.

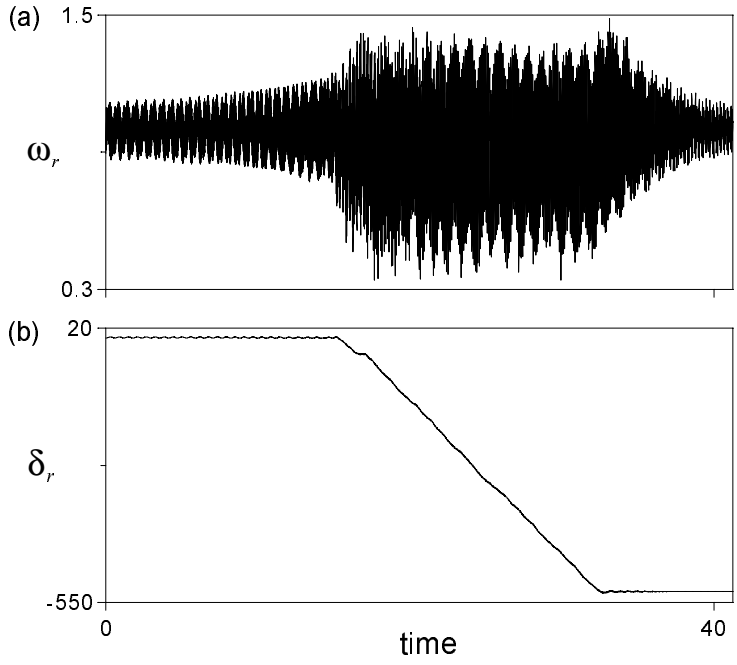

Figure 3.9: Time histories of the generator rotor speed ω_r (in rad/sec) and angle δ_r (in rad) at $\mu = 0.63868$, which is slightly larger than $\mu = C_1 \approx 0.63867$ at which the bluesky catastrophe occurs.

3.3 Effect of Damper Windings

Although damper windings have some benefits in transient stability, such as damping off speed oscillations, they may induce subsynchronous resonance. Hamdan [67] used linear theory to analyze SSR in a single-machine-infinite-busbar power system. He showed that damper windings reduce the compensation level at which subsynchronous resonance occurs. In this section, we study the effect of placing damper windings on either the q-axis, or the d-axis, or both axes on subsynchronous resonance. We evaluate the influence of these damper windings on the Hopf bifurcations and their types and the ensuing dynamic responses.

3.3.1 Q-Axis Damper Windings

For $X_Q = 1.695, X_{mq} = 1.58$, and $R_Q = 0.006$, we show in Fig. 3.10 variation of the real and imaginary parts of the eigenvalues with μ. The Jacobian matrix of the system has 14 complex conjugate eigenvalues and two real eigenvalues. As in the case without damper windings, there are 7 oscillatory modes, two associated with the electrical subsystem and 5 associated with the mechanical system. The two real eigenvalues are negative, one of them is associated with the field windings and the other is associated with the damper windings. As in the case of no damper windings, as μ increases, one of the electrical frequencies (supersynchronous) increases, whereas the other (subsynchronous) decreases. Comparing Figs. 3.4 and 3.10, we note that the damper windings accelerate the decrease in the subsynchronous electrical frequency.

As μ increases further, the frequency of the electrical mode intersects those of the fourth, third, second, and first torsional modes for values of $\mu < 1.0$, resulting in four interaction regions. As in the case without damper windings, the interaction of the electrical and fourth torsional modes is not strong enough to overcome their dampings and, hence, the equilibrium solution retains its stability. However, the other three interactions are strong enough to overcome the dampings of the interacting modes and produce three unstable intervals. In contrast with the case without damper windings where the unstable intervals do

not overlap, the unstable intervals overlap in this case, resulting in a single unstable region. Therefore, once the equilibrium solution loses its stability due to the second interaction, it does not regain it for any larger value of μ, implying the existence of only one Hopf bifurcation point.

Comparing Figs. 3.4 and 3.10, we conclude that the damper windings on the q-axis have a destabilizing influnace on the power system. First, they decrease the value of μ at which the first Hopf bifurcation occurs from 0.6186 to 0.4222. Second, they eliminate the stable region $0.7243 \leq \mu \leq 0.7460$.

In Fig. 3.11, we show variation of the real and imaginary parts of the eigenvalues when R_Q is increased to 0.015. These results are qualitatively similar to those obtained in Fig. 3.10 for $R_Q = 0.006$. However, the rates of growth of the unstable modes have increased by more than 100%. This increase may be attributed to the induction effect. In Fig. 3.12, we show variation of the maxima of the real parts of the eigenvalues with R_Q for selected values of μ. For a given value of μ, the growth rate of the instability increases as R_Q increases, attains a maximum, and then decreases.

When $R_Q \approx 0$, it follows from Eq. (3.30) that $i_Q \approx i_q X_{mq}/X_Q +$ constant, which, when substituted into Eqs. (3.27) and (3.28), leads to an effective inductance X_{qe} given by $X_{qe} \approx X_q - X_{mq}^2/X_Q$. Replacing X_q by X_{qe} in Eqs. (3.15)-(3.29) and putting $i_Q = i_D = 0$ (no damper windings), we find that the Hopf bifurcation occurs very close to that obtained by using Eqs. (3.15)-(3.30) with the q-axis damper windings.

Again, to detremine whether the created limit cycles due to the Hopf bifurcation are stable or unstable, we implement the multiple-scales algorithm outlined by Nayfeh and Balachandran [29] by using MAPLE to reduce the dynamical power system to its normal form, Eq. (3.48), in the vicinity of the Hopf bifurcation point $\mu = H \approx 0.422172$. For $P_e = 0.876, Q_e = -0.115$, and $v_t = 1.09$, we find that $\beta_1 = 7.41447$ and $\beta_2 = 0.0004867$. Thus, the Hopf bifurcation $H \approx 0.422172$ is subcritical and the limit cycles born as a result of the bifurcation are unstable. Their amplitudes are given by

$$a = 123.426\sqrt{\mu - H} \tag{3.50}$$

The dynamics of the system near the subcritical Hopf bifurcation H of Fig. 3.13 is much more complicated than the dynamics of the system near the supercritical Hopf bifurcations in the previous section. Locally, the system possesses a stable equilibrium solution and a small unstable limit cycle for values of μ slightly below that corresponding to H. As μ increases past H, the equilibrium solution loses stability and the small unstable limit cycle disappears. As μ is decreased below H, the unstable limit cycle deforms and increases in size until the branch of unstable limit cycles meets a branch of stable large-amplitude limit cycles at $\mu = 0.406425$, corresponding to point CF. As μ is decreased further, the stable and unstable limit cycles collide and annihilate each other in a cyclic-fold bifurcation.

We again use a combination of a two-point boundary-value scheme and Floquet theory [30] to study the growth and stability of the large-amplitude limit cycles when μ increases from CF. As μ increases from CF, the stable limit cycle grows in size while remaining stable with one Floquet multiplier being unity and the 15 remaining Floquet multipliers lying inside the unit circle. In Fig. 3.14(a) we show an example of a limit cycle. The phase portrait is a closed curve, the time trace of δ_r is periodic, and the FFT of δ_r consists of a single frequency and its harmonics.

When μ increases beyond a critical value $SH \approx 0.411385$, two Floquet multipliers exit the unit circle away from the real axis, signifying that SH is a secondary Hopf bifurcation. There, the limit cycle loses stability and gives way to a two-period quasiperiodic (two-torus) attractor. Two examples are displayed in Figs. 3.14(b) and (c). The trajectories do not close on themselves, the FFTs consist of two incommensurate frequencies, their multiples, and combinations, and the time traces are modulated.

As μ increases slightly above SH to $C \approx 0.418574$, the two-torus collides with its basin boundary, resulting in their destruction in a bluesky catastrophe. This can be observed in Fig. 3.15, which displays the time histories of δ_r and ω_r at $\mu = 0.418576$, which is slightly larger than $C \approx 0.418574$. We note that the bluesky catastrophe and hence the system

loses synchronism at a value of μ that is less than H.

3.3.2 D-Axis Damper Windings

For $X_D = 1.666, X_{md} = 1.66$, and $R_D = 0.0037$, we show in Fig. 3.16 variation of the real and imaginary parts of the eigenvalues with μ. Comparing Figs. 3.16 and 3.3, we note that the d-axis damper windings accelerate the decrease of the subsynchronous electrical frequency and hence its interaction with those of the fourth, third, and second torsional modes, as in the case of the q-axis damper windings. Consequently, the d-axis damper windings reduce the compensation level at which the Hopf bifurcation occurs from $\mu \approx 0.6186$ to $\mu \approx 0.5628$. Again, the instability regions overlap and there is only one Hopf bifurcation; that is, the d-axis damper windings eleminate the stable region $0.7243 \leq \mu \leq 0.7466$.

Next, we investigate the dynamics of the power system near the Hopf bifurcation $H \approx 0.5628$ by determining its normal form, Eq. (3.48). For the case depicted in Fig. 3.17, $P_e = 0.876$, Q_e = -0.115, and $v_t = 1.09$, we find that $\beta_1 = 9.0094$ and β_2 = - 0.00898363. Because $\beta_2 < 0$, we conclude that H is supercritical and the limit cycles born as a result of the bifurcation are stable. Their amplitudes are given by

$$a = 31.653\sqrt{\mu - H} \tag{3.51}$$

To study the development and stability of the limit cycles when μ moves away from the Hopf bifurcation inside the unstable region, we use a combination of a two-point boundary-value algorithm and Floquet theory. As μ increases from H, the limit cycle grows in size while remaining stable with one Floquet multiplier being unity and the 15 remaining Floquet multipliers lying inside the unit circle. See Fig. 3.18(a) for an example of a limit cycle. The time trace is periodic, the FFT of the corresponding generator rotor angle δ_r consists of a discrete frequency and its harmonics, and the trajectory closes on itself.

When μ passes a critical value $SH \approx 0.59283$, two of the Floquet multipliers exit the unit circle away from the real axis, signifying that SH is a secondary Hopf bifurcation.

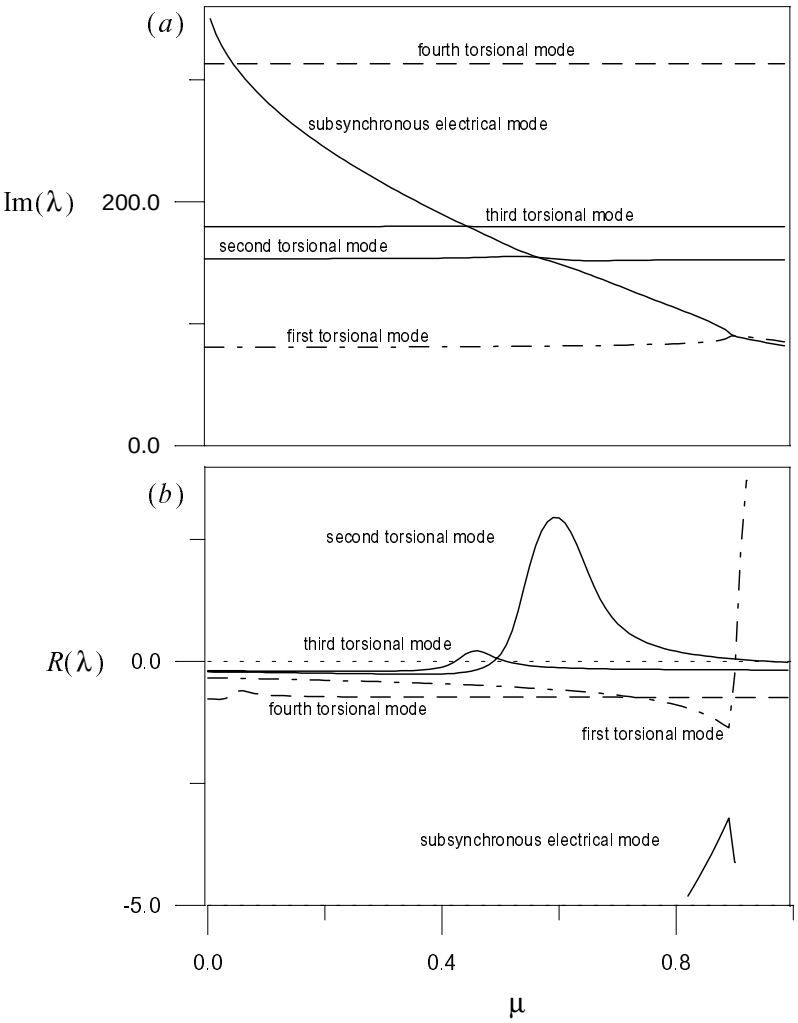

Figure 3.10: Variation of the real and imaginary parts of the eigenvalues with μ when $P_e = 0.876, Q_e = -0.115, v_t = 1.09$, and $R_Q = 0.006$. There is only one Hopf bifurcation at $\mu \approx 0.422172$.

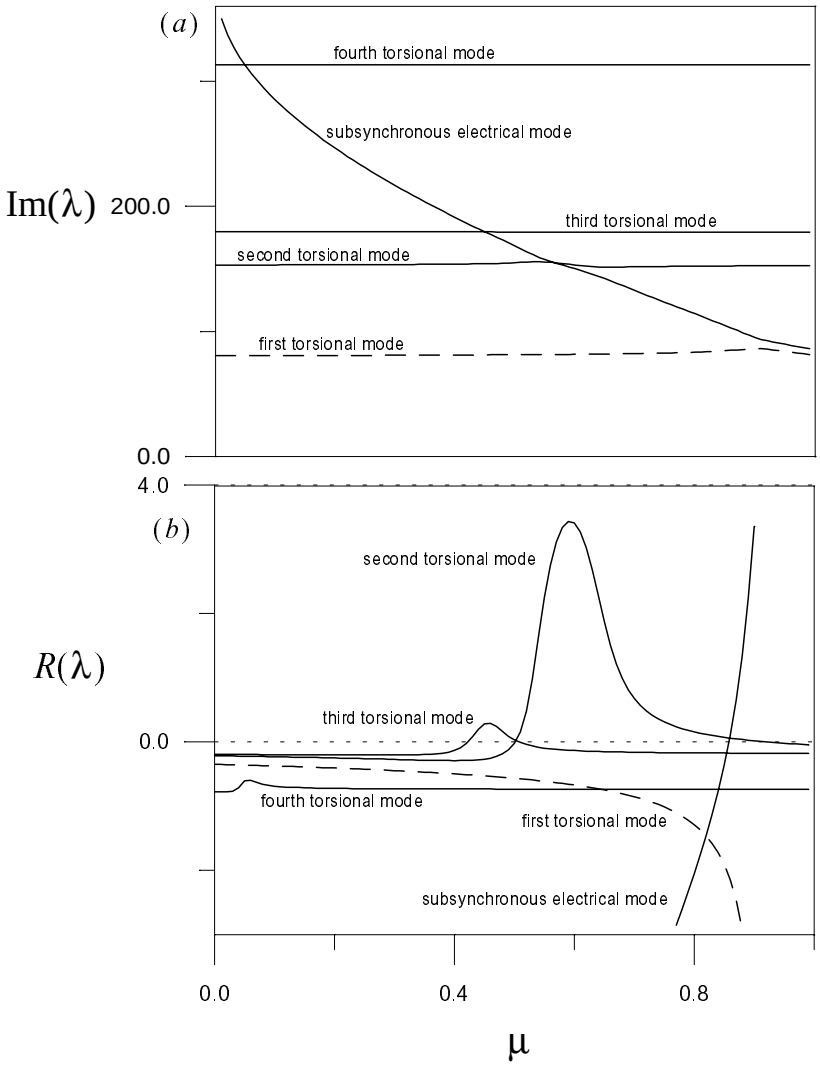

Figure 3.11: Variation of the real and imaginary parts of the eigenvalues with μ when R_Q = 0.015.

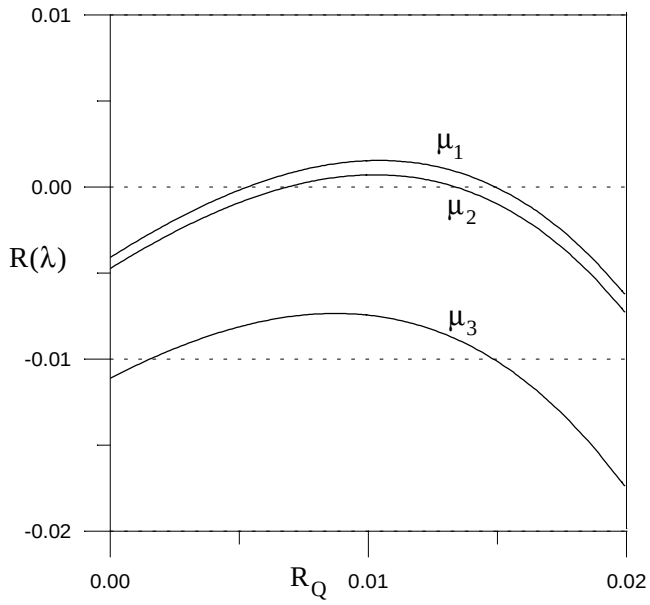

Figure 3.12: Variation of the maximum real parts of the eigenvalues with R_Q for three values of μ : $\mu_1 = 0.422127$, $\mu_2 = 0.422027$, and $\mu_3 = 0.421027$.

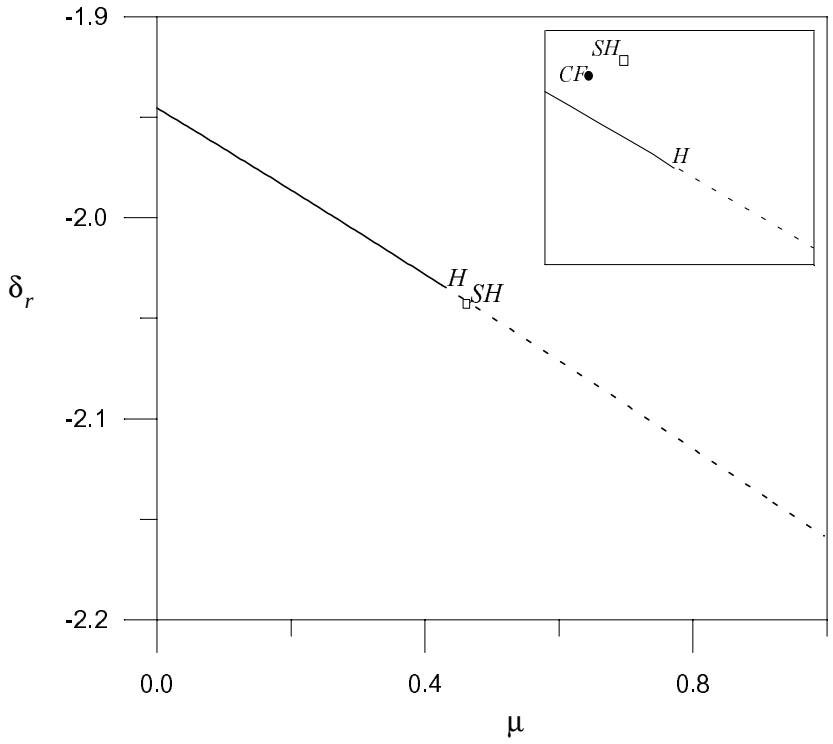

Figure 3.13: Bifurcation diagram showing variation of the generator rotor angle δ_r with the compensation level μ. The solid line denotes sinks and the dashed line denotes unstable foci.

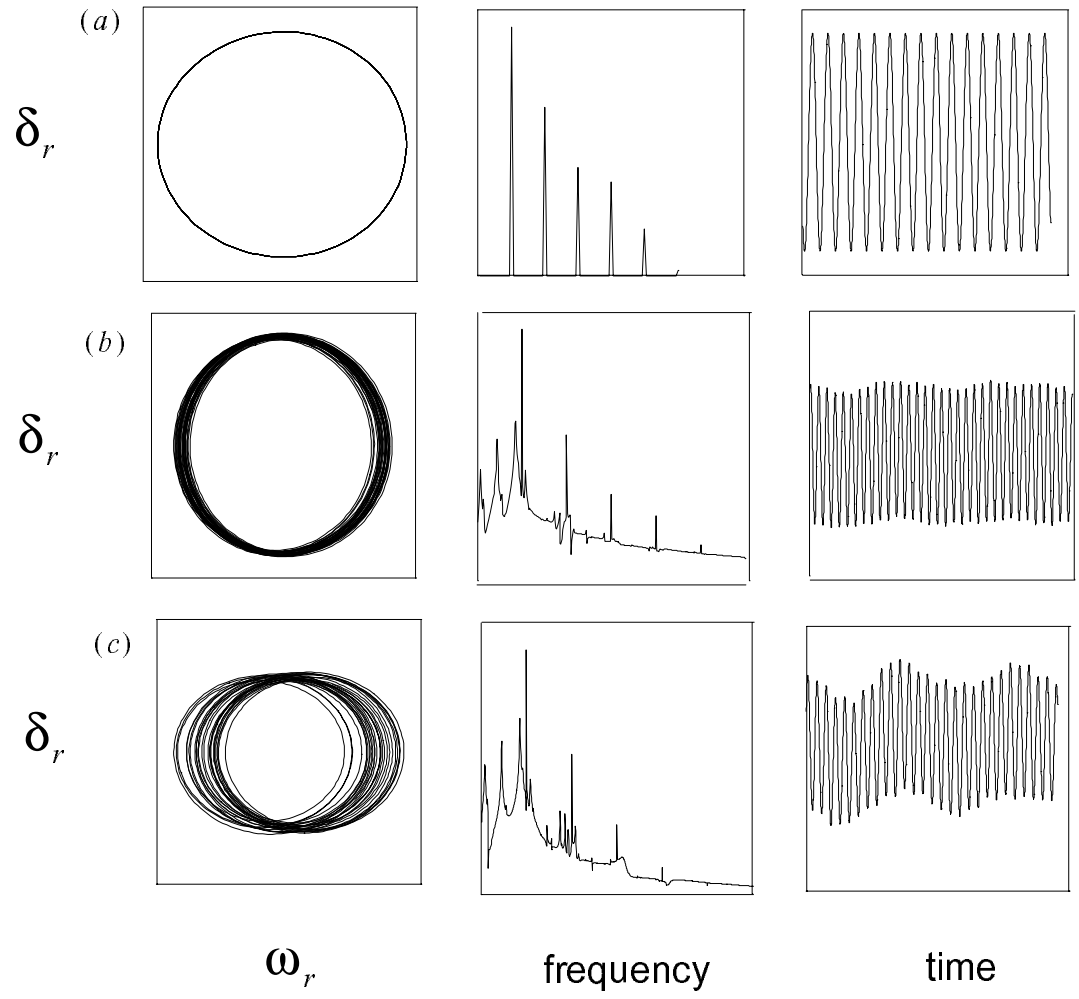

Figure 3.14: Two-dimensional projections of the phase portrait onto the $\omega_r - \delta_r$ plane(left), the FFT of the corresponding generator rotor angle δ_r (middle), and the time traces of the generator rotor angle δ_r (right) at μ = (a) 0.406425, (b) 0.411385, and (c) 0.417424. The solution at (a) is a limit cycle, at (b) is a two-torus attractor recorded well before the bluesky catastrophe, and at (c) is a two-torus attractor located just before it disappears in a bluesky catastrophe.

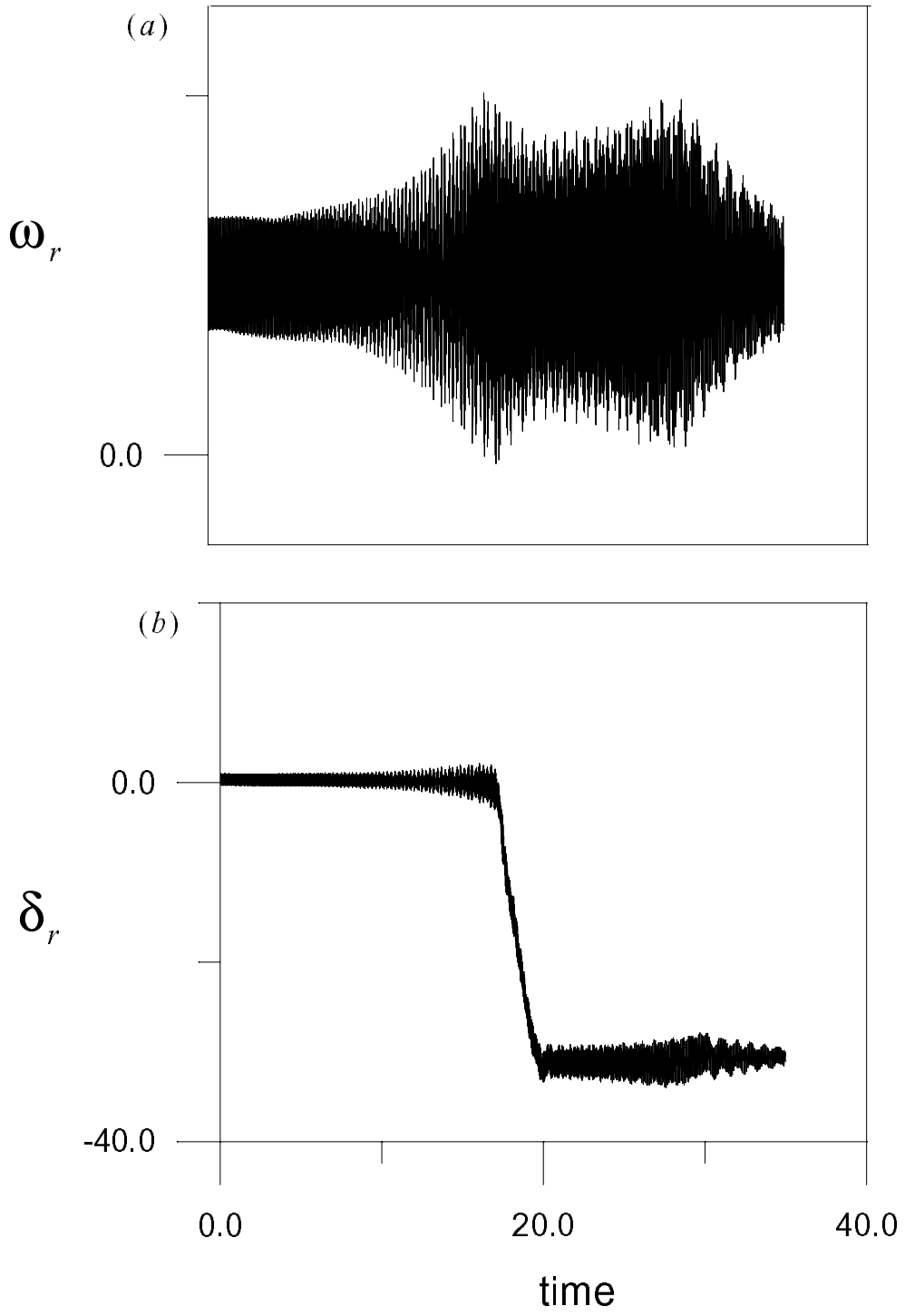

Figure 3.15: Time histories of the generator rotor speed ω_r (in rad/sec) and angle δ_r (in rad) at $\mu = 0.418576$, which is slightly larger than $C \approx 0.418574$ at which the bluesky catastrophe that occurs.

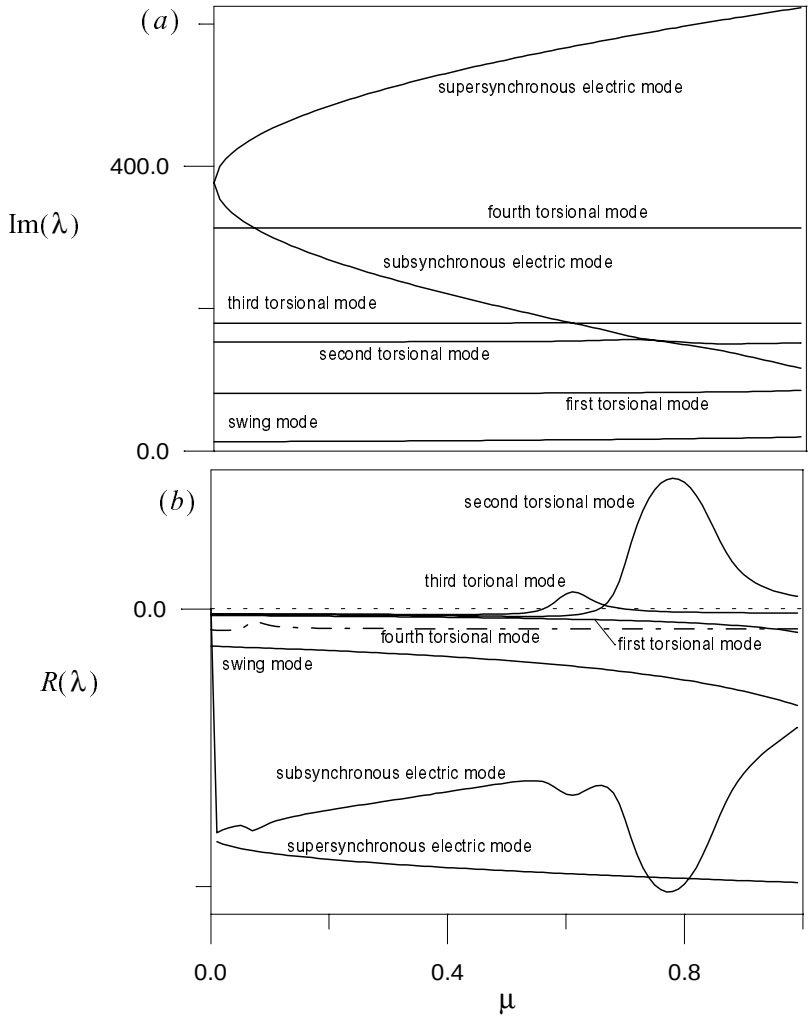

Figure 3.16: Variation of the real and imaginary parts of the eigenvalues with μ in the case of d-axis damper windings when R_D= 0.0037.

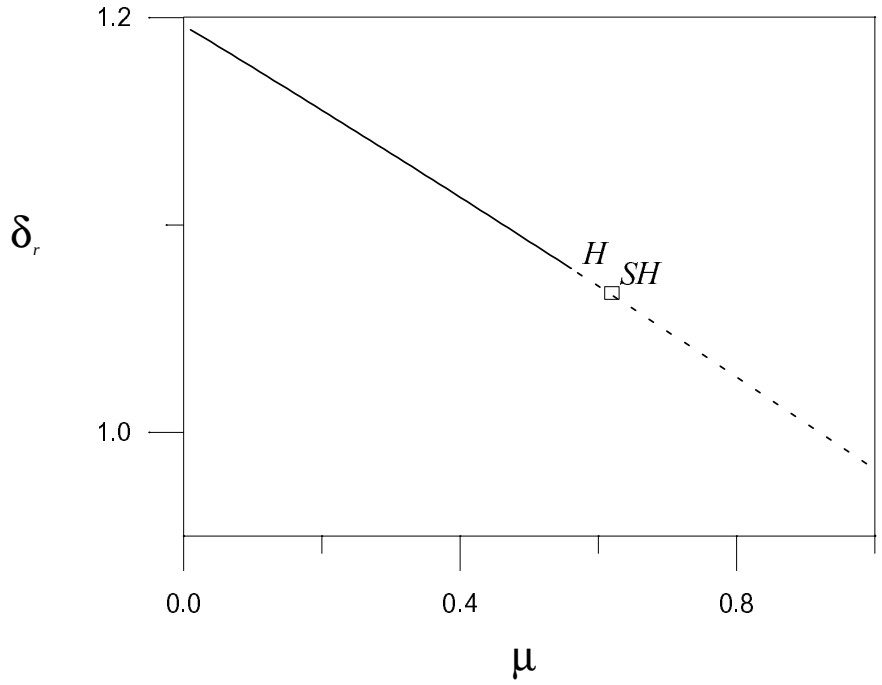

Figure 3.17: Bifurcation diagram showing variation of the generator rotor angle δ_r with the compensation level μ. The solid line denotes sinks and the dashed line denotes unstable foci.

There, the limit cycle loses stability and gives way to a two-period quasiperiodic (two-torus) attractor. Two examples are displayed in Figs. 3.18(b) and (c). The time histories are modulated, the trajectories do not close on themselves, and the FFTs of δ_r seem to consist of two incommensurate frequencies, their multiples, and combinations.

As μ increases slightly above SH to $C \approx 0.6298$, the two-torus collides with its basin boundary, yielding their destruction in a bluesky catastrophe. This can be observed in Fig. 3.19, which displays the time history of δ_r in the vicinity of the bluesky catastrophe.

3.3.3 Q and D - Axes Damper Windings

For $X_Q = 1.696, X_{mq} = 1.58, R_Q = 0.006, X_D = 1.666, X_{md} = 1.66$, and $R_D = 0.0037$, we show in Fig. 3.20 variation of the real and imaginary parts of the eigenvalues with μ. Again, we note that the two damper windings accelerate the decrease in the subsynchronous electrical frequency. The unstable regions overlap so that there is only one Hopf bifurcation point. Moveover, the Hopf bifurcation point is reduced to 0.4004. In Fig. 3.21, we show the influence of the damper windings on the loci of the Hopf bifurcation in the $P_e - \mu$ plane for $v_t = 1.09$ and $Q_e = -0.115$. Clearly, placing damper windings on either the d-axis or the q-axis or both axes reduces the compensation level at which the Hopf bifurcations and hence the instability of the power system occur. So, we conclude that including damper windings along either the q-axis, the d-axis, or both axes shrinks the stable region of the power system, in agreement with Hamdan [67]. Moreover, the q-axis damper windings are more destabilizing than the d-axis damper windings.

Now we investigate the dynamics of the power system in the vicinity of the Hopf bifurcation $H \approx 0.400411$ by determining its normal form, Eq. (3.48). For the case depicted in Fig. 3.22, $P_e = 0.876$, Q_e = -0.115, and $v_t = 1.09$, we find that $\beta_1 = 5.77715$ and β_2 = -0.000211097. Because $\beta_2 < 0$, we conclude that H is supercritical and the limit cycles born as a result of the bifurcation are stable. Their amplitudes are given by

$$a = 165.4305\sqrt{\mu - H} \tag{3.52}$$

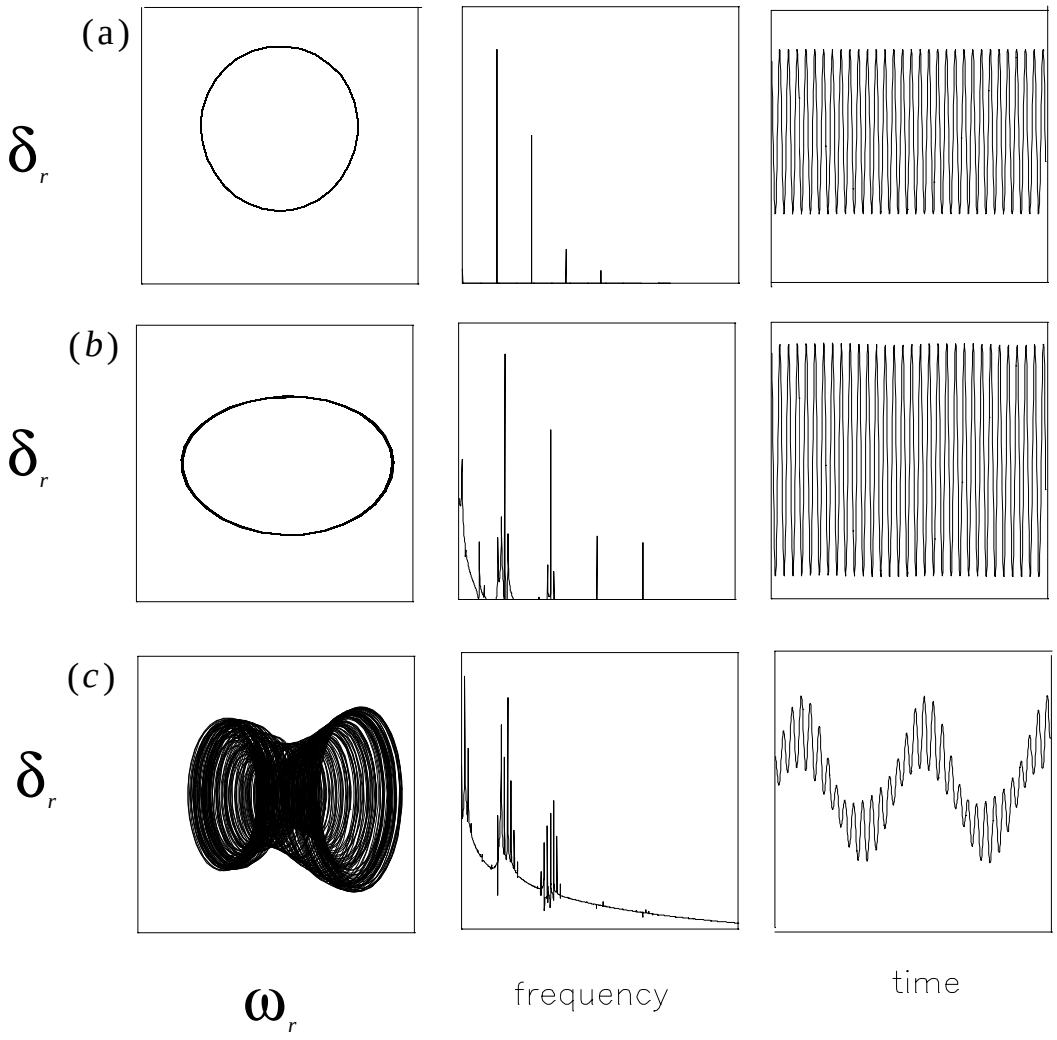

Figure 3.18: Two-dimensional projections of the phase portrait onto the $\omega_r - \delta_r$ plane(left), the FFT of the corresponding generator rotor angle δ_r (middle), and the time traces of the generator rotor angle δ_r (right) at $\mu =$ (a) 0.5738, (b) 0.59295, and (c) 0.59585. The solution at (a) is a limit cycle, at (b) is a two-torus attractor recorded well before the bluesky catastrophe, and at (c) is a two-torus attractor located just before it disappears in a bluesky catastrophe.

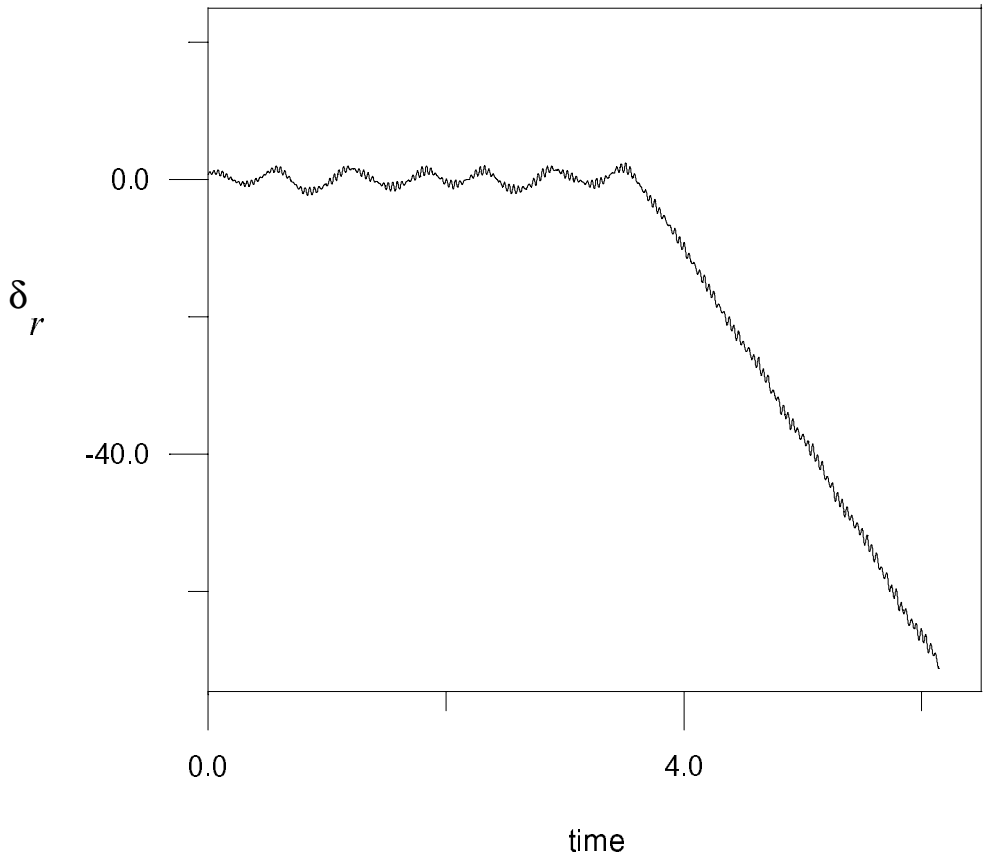

Figure 3.19: The time history of the generator rotor angle δ_r (in rad) at $\mu = 0.60787$, which is slightly larger than $C \approx 0.60785$ at which the bluesky catastrophe that occurs.

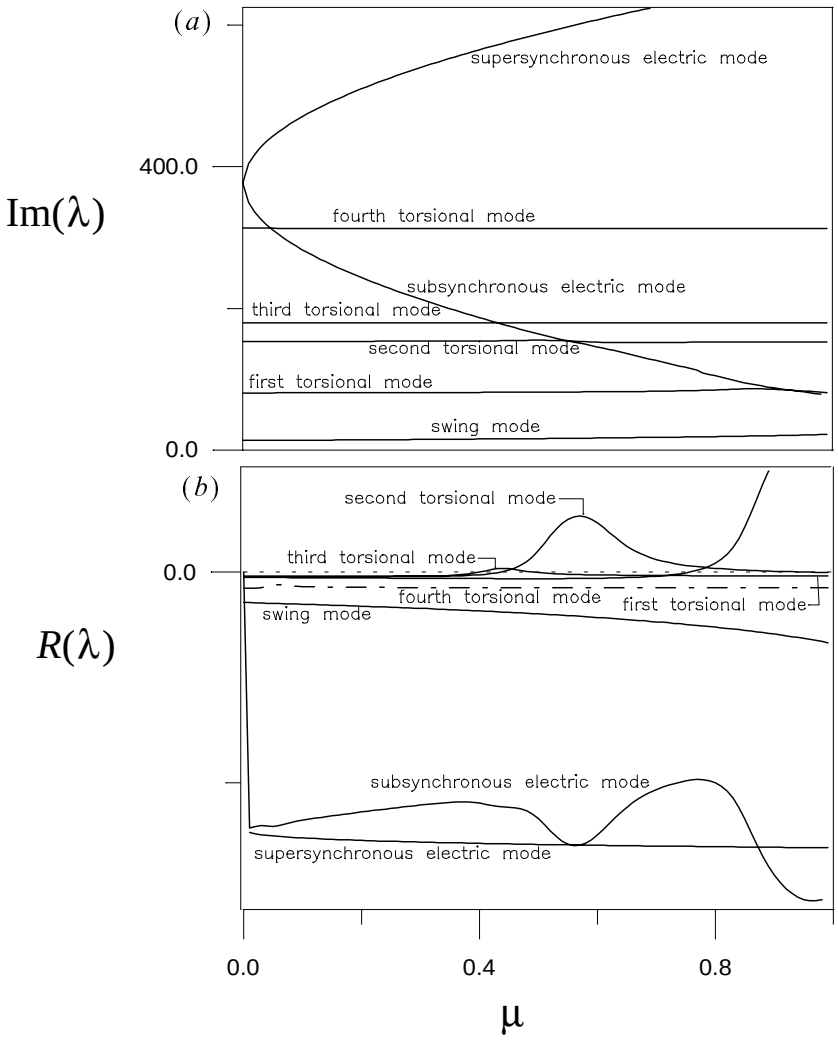

Figure 3.20: Variation of the real and imaginary parts of the eigenvalues with μ in the case of d-and-q axes damper windings when $R_Q = 0.006$ and $R_D = 0.0037$.

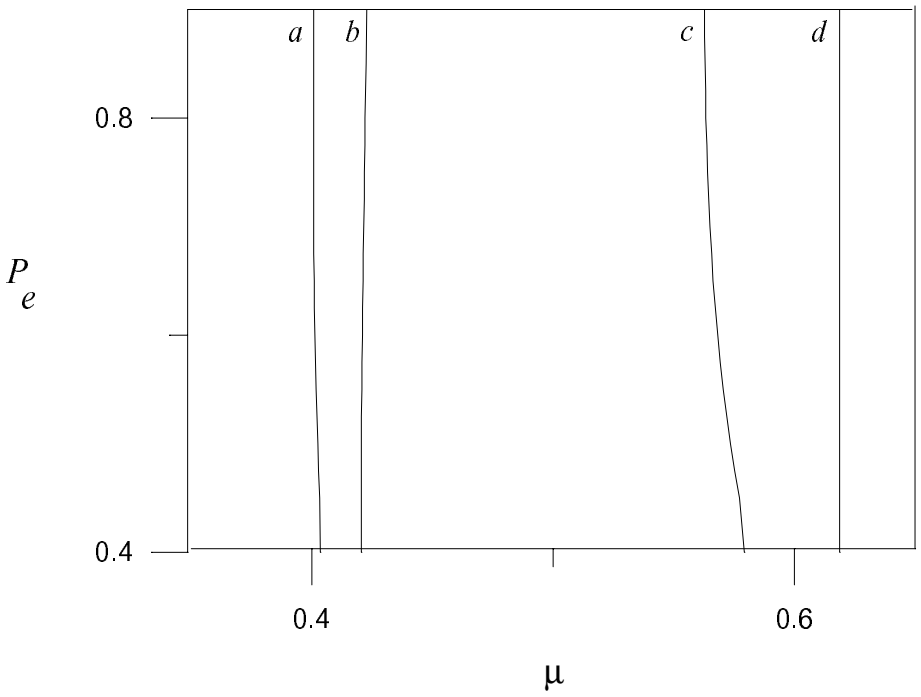

Figure 3.21: Variation of the loci of the Hopf bifurcation points with P_e when $v_t = 1.09$ and $Q_e = -0.115$. Line a corresponds to $R_D = R_Q = 0.0037$, line b corresponds to $R_Q = 0.0037$ and $R_D = 0.0$, line c corresponds to $R_D = 0.0037$ and $R_Q = 0.0$, and line d corresponds to $R_D = R_Q = 0.0$.

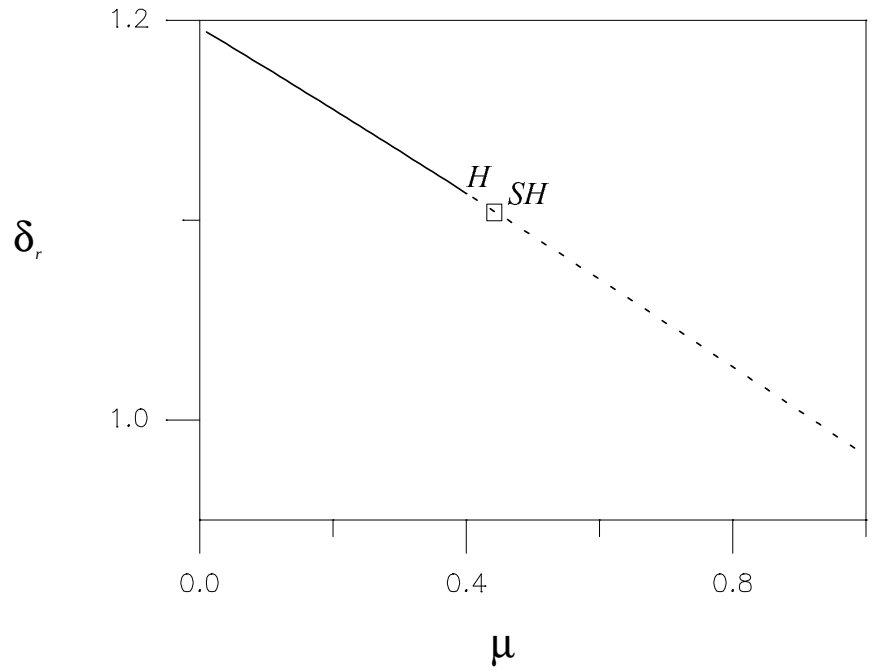

Figure 3.22: Bifurcation diagram showing variation of the generator rotor angle δ_r with the compensation level μ. The solid line denotes sinks and the dashed line denotes unstable foci.

Next, we study the growth and stability of the limit cycles when μ moves away from the Hopf bifurcation inside the unstable region by means of a two-point boundary-value algorithm and Floquet theory [30]. As μ increases from H, the limit cycle grows in size while remaining stable with one Floquet multiplier being unity and the 16 remaining Floquet multipliers lying inside the unit circle. See Figs. 3.23(a) for an example of a limit cycle and the corresponding time trace of the generator rotor angle δ_r. The time history is uniform, the FFT consists of a single frequency and its harmonic, and the trajectory closes on itself.

When μ passes a critical value $SH \approx 0.40271$, two of the Floquet multipliers exit the unit circle away from the real axis, signifying that SH is a secondary Hopf bifurcation. There, the limit cycle loses stability and gives way to a two-period quasiperiodic (two-torus) attractor. Two examples are displayed in Figs. 3.23(b) and (c). The time traces are modulated, the FFTs consist of two incommensurate frequencies, their multiples and their combinations, and the trajectories do not close on themselves. As μ increases slightly above SH to $C \approx 0.40641$, the two-torus collides with its basin boundary, yielding their destruction in a bluesky catastrophe.

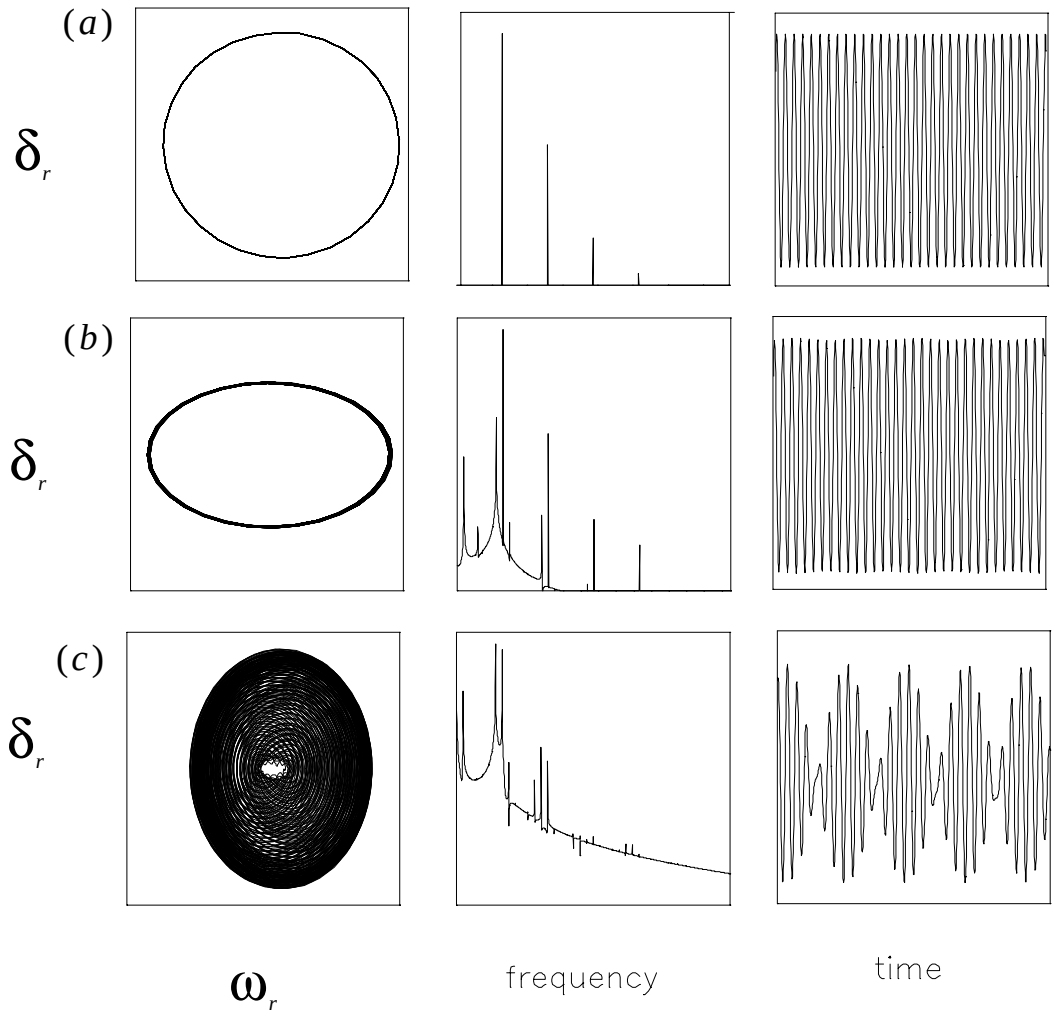

Figure 3.23: Two-dimensional projections of the phase portrait onto the $\omega_r - \delta_r$ plane(left), the FFTs of the corresponding generator rotor angle δ_r (middle), and the time traces of the generator rotor angle δ_r (right) at μ = (a) 0.402011355, (b) 0.403222355, and (c) 0.403211355. The solution at (a) is a limit cycle, at (b) is a two-torus attractor recorded well before the bluesky catastrophe, and at (c) is a two-torus attractor located just before it disappears in a bluesky catastrophe.

Chapter 4

ON THE EFFECT OF MACHINE SATURATION

To make the bifurcation analysis of subsynchronous resonance of power systems simple and manageable, all of the authers have neglected the effect of stator and rotor iron saturation in synchronous machines. However, the importance of saturation has been recognized by many authors [e.g, 34,35,...,57]. In this chapter, we carry out a bifurcation analysis in a complete model of the CHOLLA#4 station. The model includes saturation, but neglects the dynamics of the automatic voltage regulator (AVR) and the turbine governor.

It is evident that accounting for saturation in both the d- and q-axes can lead to an improvement in the accuracy of the simulation models. To account for the iron saturation in stability studies, one usually makes the following assumptions[33]:

(i) The leakage fluxes are in air for a large portion of their pathes. Hence, they are not significantly affected by saturation of the iron core. So, the leakage inductances are independent of the iron saturation. As a result, the only elements that saturate are the mutual flux linkages ψ_{md} and ψ_{mq}.

(ii) The leakage fluxes are usually small and their pathes coincide with that of the main flux for only a small part of its path. So, saturation can be determined by the air-gap flux linkage only.

(iii) The saturation relationship between the resultant air-gap flux and the mmf under loaded conditions is the same as that under no-load conditions. This allows the saturation characteristics to be represented by the open-circuit saturation curve.

In this chapter, we use the modern methods of nonlinear dynamics to analyze the effect of machine saturation on subsynchronous resonance of another practical power system model.

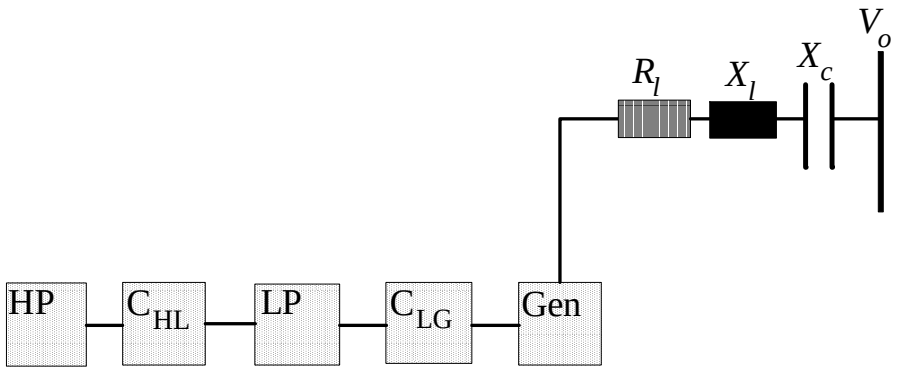

Figure 4.1: A schematic diagram for a series capacitor-compensated single-machine power system. The mechanical system consists of a high-pressure (HP), a coupling mass (C_{HL}), a low-pressure (LP), and a coupling mass (C_{LG}) turbine section, and a generator (Gen).

In Sec. 4.1, we briefly describe the CHOLLA#4 generator, in Sec. 4.2, we analyze the case of no saturation, and in Sec. 4.3, we analyze the effect of saturation on subsynchronous resonance of the power system.

4.1 System Description

We consider a single-machine-infinite-busbar (SMIB) power system, as shown in Fig. 4.1. The model and its parameters are chosen to represent the characteristics of the CHOLLA#4 generator with respect to the SOWARO station at the Arizona Public Service when the generator is heavily loaded.

To obtain analytical formulas for the fluxes ψ_{md} and ψ_{mq} as functions of the currents, we represent the test data which discussed by Denndon in [52], shown in Fig. 4.2, by the following third-order polynomials:

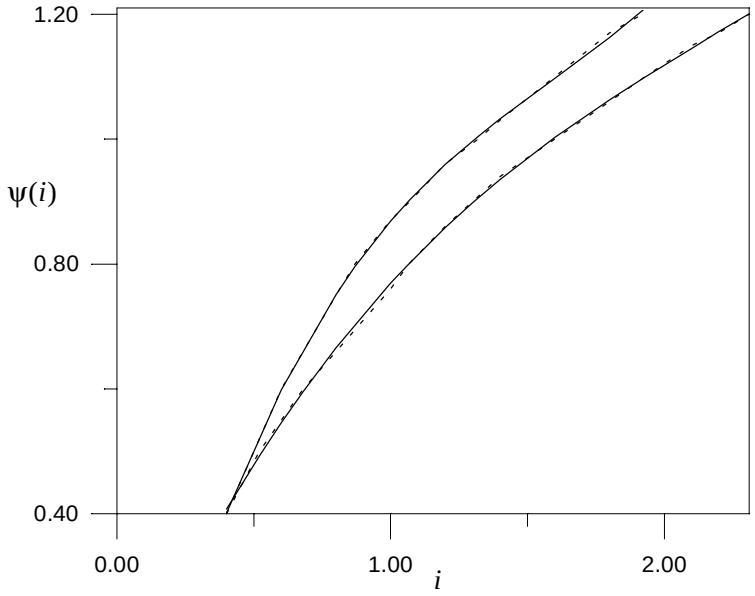

Figure 4.2: Variation of the flux linkage ψ with the current i.

$$\psi_{md} = d_0 + d_1(i_f - i_d) + d_2(i_f - i_d)^2 + d_3(i_f - i_d)^3 \tag{4.1}$$

$$\psi_{mq} = q_0 + q_1(i_Q - i_q) + q_2(i_Q - i_q)^2 + q_3(i_Q - i_q)^3 \tag{4.2}$$

where the d_n and q_n are constants. Clearly, the mutual flux linkages ψ_{md} and ψ_{mq} are nonlinear functions of the machine currents i_d, i_q, i_f, and i_Q. The d-and q-axes flux linkages ψ_d and ψ_q can be determined from the mutual flux linkages ψ_{md} and ψ_{mq} as follows:

$$\psi_d = \psi_{md} - X_{le} i_d \tag{4.3}$$

$$\psi_q = \psi_{mq} - X_{le} i_q \tag{4.4}$$

$$\psi_f = \psi_{md} + X_{le} i_f \tag{4.5}$$

$$\psi_Q = \psi_{mq} + X_{le} i_Q \tag{4.6}$$

where X_{le} is the leakage reactance.

The power-system model is governed by 16 first-order nonlinear ordinary-differential equations, 6 of them represent the electrical subsystem while the other 10 represent the mechanical subsystem. The mechanical subsystem consists of a high-pressure (HP) and a low-pressure (LP) turbine section, a generator, and two coupling masses. One couples the high and low-pressure turbines and the second couples the low-pressure turbine with the generator, as indicated in Fig. 4.1.

In this formulation, the dynamics of the automatic voltage regular (AVR) and the turbine governor are neglected. The dynamics of the damper windings on the q-axis as well as the machine saturation are included. Substituting Eqs. (4.1)-(4.6) into Eqs. (3.1)-(3.29), one obtains the following equations:

$$a_{11}\frac{di_d}{dt} + a_{13}\frac{di_f}{dt} = [(R_l + R_a)i_d - X_l i_q + e_{cd} + v_0 \sin\delta_r + \omega_r \psi_q]\omega_b \tag{4.7}$$

$$a_{22}\frac{di_q}{dt} + a_{24}\frac{di_Q}{dt} = [(R_l + R_a)i_q + X_l i_d + e_{cq} + v_0 \cos\delta_r - \omega_r \psi_d]\omega_b \tag{4.8}$$

$$a_{31}\frac{di_d}{dt} + a_{33}\frac{di_f}{dt} = (v_f - R_f i_f)\omega_b \tag{4.9}$$

$$a_{42}\frac{di_q}{dt} + a_{44}\frac{di_Q}{dt} = -R_Q i_Q \omega_b \tag{4.10}$$

$$\frac{de_{cd}}{dt} = (\mu X_l i_d + e_{cq}\omega_r)\omega_b \tag{4.11}$$

$$\frac{de_{cq}}{dt} = (\mu X_l i_q - e_{cd}\omega_r)\omega_b \tag{4.12}$$

$$\frac{d\omega_1}{dt} = \frac{1}{M_1}[-D_1(\omega_1 - 1) - K_{12}(\theta_1 - \theta_2)] \tag{4.13}$$

$$\frac{d\theta_1}{dt} = (\omega_1 - 1)\omega_b \tag{4.14}$$

$$\frac{d\omega_2}{dt} = \frac{1}{M_2}[-D_2(\omega_2 - 1) + K_{12}(\theta_1 - \theta_2) - K_{23}(\theta_2 - \theta_3)] \tag{4.15}$$

$$\frac{d\theta_2}{dt} = (\omega_2 - 1)\omega_b \tag{4.16}$$

$$\frac{d\omega_3}{dt} = \frac{1}{M_3}[-D_3(\omega_3 - 1) + K_{23}(\theta_2 - \theta_3) - K_{34}(\theta_3 - \theta_4)] \tag{4.17}$$

$$\frac{d\theta_3}{dt} = (\omega_3 - 1)\omega_b \tag{4.18}$$

$$\frac{d\omega_4}{dt} = \frac{1}{M_4}[-D_4(\omega_4 - 1) + K_{34}(\theta_3 - \theta_4) - K_{45}(\theta_4 - \delta_r)] \tag{4.19}$$

$$\frac{d\theta_4}{dt} = (\omega_4 - 1)\omega_b \tag{4.20}$$

$$\frac{d\omega_r}{dt} = \frac{1}{M_5}[-D_5(\omega_r - 1) + K_{45}(\theta_4 - \delta_r) + T_m - T_e] \tag{4.21}$$

$$\frac{d\delta_r}{dt} = (\omega_r - 1)\omega_b \tag{4.22}$$

where

$$\mu = X_c/X_l,$$

$$T_e = i_q\psi_d - i_d\psi_q,$$

$$a_{11} = -\zeta_1 - X_l - X_{le},$$

$$a_{22} = -\zeta_2 - X_l - X_{le},$$

$$a_{33} = \zeta_1 + X_{lf},$$

$$a_{44} = \zeta_2 + X_{lQ},$$

$$a_{13} = -a_{31} = \zeta_1,$$

$$a_{24} = -a_{42} = \zeta_2,$$

where

$$\zeta_1 = d_1 + 2d_2(i_f - i_d) + 3d_3(i_f - i_d)^2,$$

$$\zeta_2 = q_1 + 2q_2(i_Q - i_q) + 3q_3(i_Q - i_q)^2$$

Here X_{le}, X_{lf}, and X_{lQ} are the leakage reactances.

Equations (4.7)-(4.22) constitute a system of 16 first-order nonlinear ordinary-differential equations describing the dynamics of the SMIB power system shown in Fig. 4.1. The 16

state variables of the system are $i_d, i_q, i_f, i_Q, e_{cd}, e_{cq}, \omega_1, \theta_1, \omega_2, \theta_2, \omega_3, \theta_3, \omega_4, \theta_4, \omega_r$, and δ_r. The parameters used in this study in p.u. for the generator and the line are

$$R_f = 0.001252, \quad R_a = 0.0045, \quad X_\ell = 0.08366, \quad R_\ell = 0.00172,$$

$$R_Q = 0.009957, \quad X_{le} = 0.1450, \quad X_{lf} = 0.1061, \quad X_{lQ} = 0.3819,$$

$$d_0 = -0.1626, \quad d_1 = 1.7374, \quad d_2 = -0.8939, \quad d_3 = 0.1876,$$

$$q_0 = 0.0635, \quad q_1 = 0.9808, \quad q_2 = -0.3244, \quad q_3 = 0.0489$$

The mechanical damping coefficients and the inertias and stiffnesses in p.u. are

$$\begin{array}{lll} D_1 = 0.02677, & M_1 = 0.4930, & \\ D_2 = 0.0, & M_2 = 0.03107, & K_{12} = 107.611, \\ D_3 = 0.04150, & M_3 = 2.8383, & K_{23} = 61.705, \\ D_4 = 0.0, & M_4 = 0.1156, & K_{34} = 141.413, \\ D_5 = 0.06832, & M_5 = 1.6512, & K_{45} = 175.208. \end{array}$$

4.2 The Case of No Saturation

In the case of no saturation, we set d_0, d_2, d_3, q_0, q_2, and q_3 equal to zero in Eqs. (4.1) and (4.2) and obtain a system of 16 ordinary-differential equations. The operating conditions are obtained from the system of equations by setting the derivatives of the state variables of the system (4.7)-(4.22) equal to zero. The result is summarized in Appendix A.

When $P_e = 0.9, Q_e = 0.4358$, and $v_t = 1.0$, we show variation of the real and imaginary parts of the eigenvalues with μ in Fig. 4.3. There are 14 complex and two real eigenvalues. Because the Jacobian matrix is real, the complex conjugate of each complex value is an eigenvalue, yielding 7 oscillatory modes. Two modes are electrical modes and 5 are mechanical modes. The mode with the lowest frequency is the swing or electro-mechanical mode whereas the other four mechanical modes are torsional modes. Two of the torsional modes, the third and the fourth modes, are damped and have very high frequencies, namely, 1030 and 1450 rad/sec. Hence, they do not interact with the electrical modes for realistic

compensation levels. The two real eigenvalues are negative, one is associated with the field windings while the other is associated with the damper windings.

For small μ, the frequencies of the electrical modes are approximately 377 rad/sec. As μ increases, the supersynchronous and subsynchronous frequencies separate from each other. As for the BOARDMAN system, the supersynchronous mode is highly damped whereas the subsynchronous is not. We will focus on the subsynchronous frequency and how its associated mode interacts with the second and first torsional modes.

It follows from Fig. 4.3(b) that, as μ increases, the frequency of the subsynchronous electrical mode decreases and approaches the frequency of the second torsional mode (≈ 199 rad/sec) at $\mu \approx 0.88103$. Consequently, the eigenvalues associated with the second torsional mode move to the right and cross transversely the imaginary axis into the right-half of the complex plane at $\mu = H \approx 0.88103$. Consequently, the second torsional mode loses stability via a Hopf bifurcation, which is labeled H in Fig. 4.4. In the present case, the frequency of the electrical mode intersects the second torsional mode for values of $\mu < 1.0$, resulting in one interaction region. Once the equilibrium point loses its stability due to this interaction, it does not regain it for any larger value of μ. Consequently, we conclude that there is only one Hopf bifurcation point.

In Fig. 4.5, we show variation of the loci of the Hopf bifurcation in the $P_e - \mu$ plane for $v_t = 1.0$ and $Q_e = 0.4358$. All modes located to the left of the solid curve are positively damped. The second torsional mode is negatively damped to the right of the solid curve.

The algorithm based on the method of multiple scales, outlined by Nayfeh and Balachandran [30], is used to reduce the system of 16 nonlinear ordinary-differential equations to its normal form in the vicinity of the Hopf bifurcation $H \approx 0.881003$, which occurs when $P_e = 0.9, Q_e = 0.4358$, and $v_t = 1.0$. Variation of the amplitude a of oscillations with time near H is given by

$$a' = (\mu - H)\beta_1 a + \beta_2 a^3 \tag{4.23}$$

with $\beta_1 = 0.620837$ and $\beta_2 = -0.000405884$. Because $\beta_2 < 0$, the Hopf bifurcation is

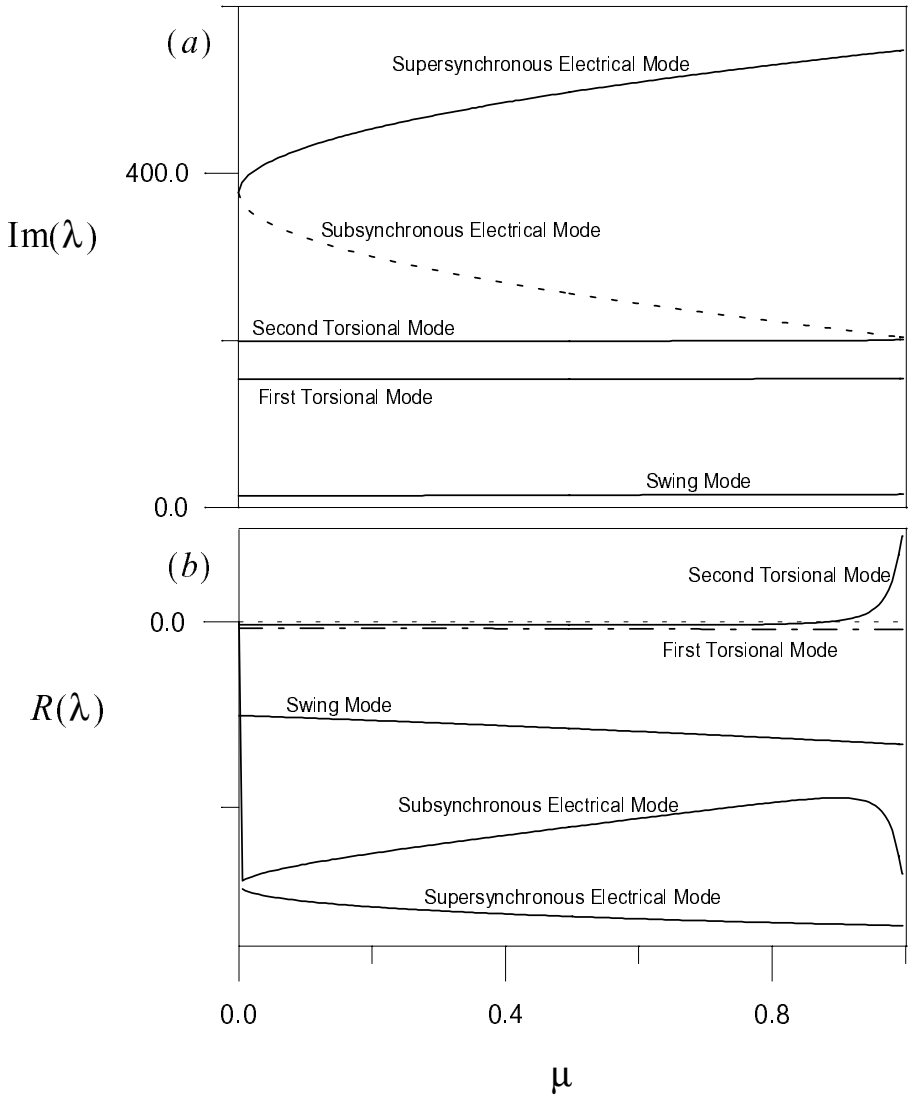

Figure 4.3: Variation of the real and imaginary parts of the eigenvalues with μ for $Q_e = 0.4358, P_e = 0.9$, and $v_t = 1.0$. (No saturation)

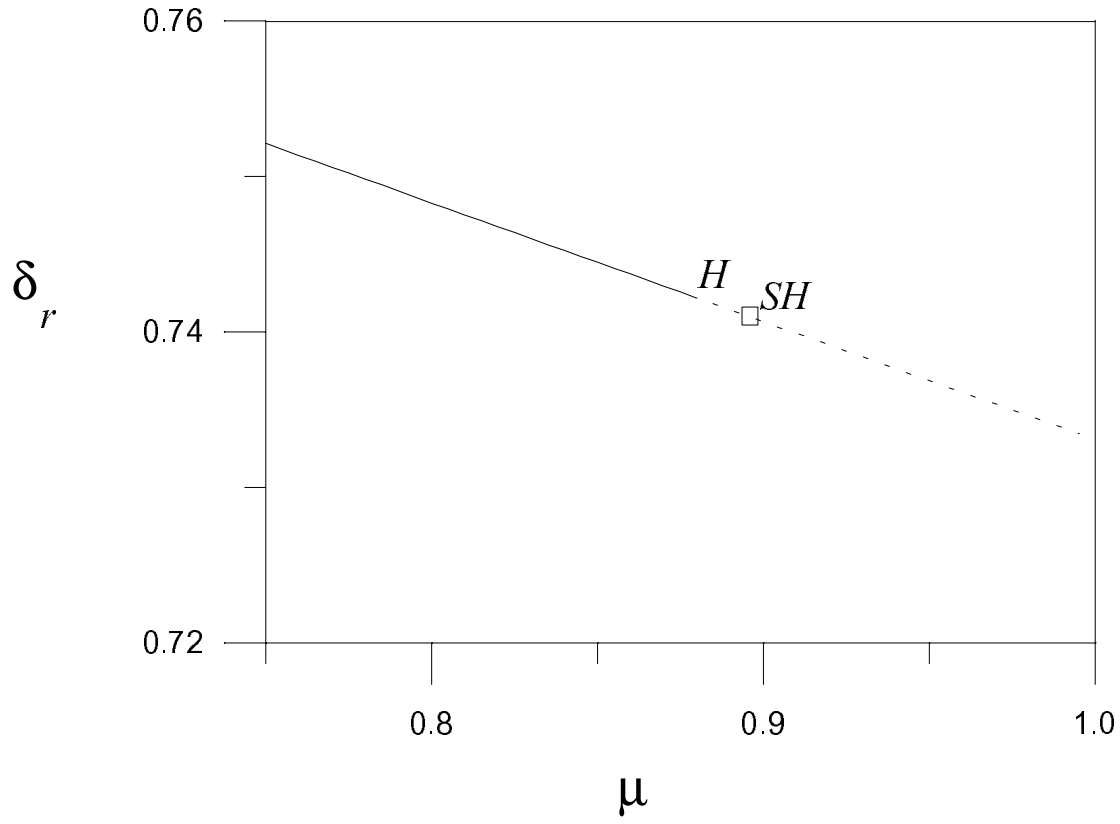

Figure 4.4: Variation of the rotor angle δ_r with the compensation level μ for the case $P_e = 0.9$, $Q_e = 0.4358$, and $v_t = 1.0$. The solid line denotes stable equilibria and the dashed line denotes unstable equilibria. The symbols H and SH indicate the compensation levels where the Hopf and seconary Hopf bifurcations occur, respectively. (No saturation)

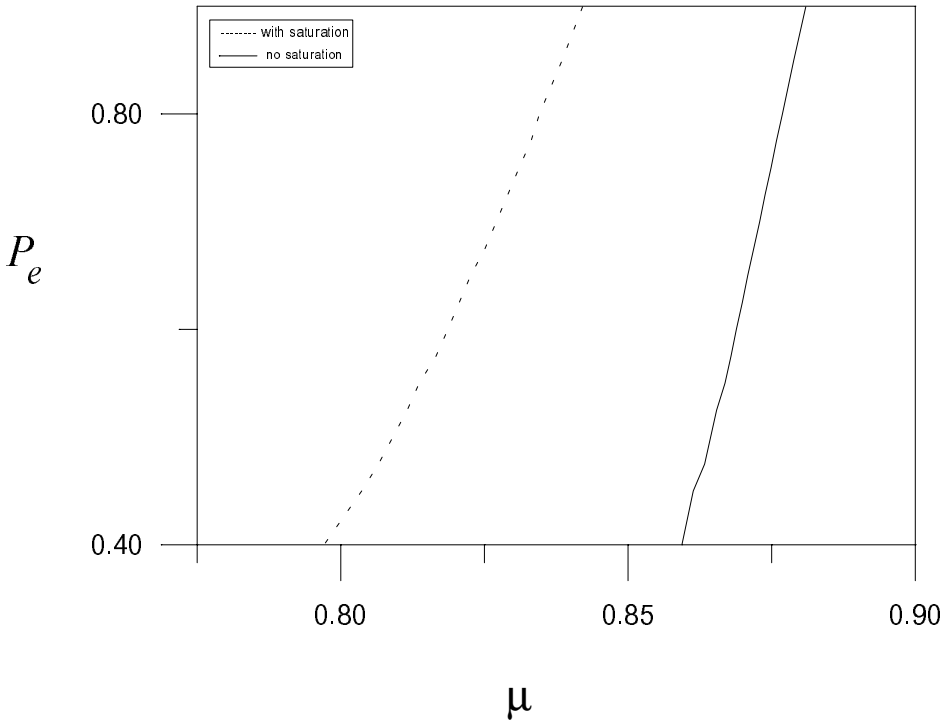

Figure 4.5: Variation of the loci of the Hopf bifurcation points with P_e and μ for $v_t = 1.0$ and $Q_e = 0.4358$.

supercritical and the limit cycles born as a result of the bifurcation are stable. Their amplitudes are given by

$$a = 39.11\sqrt{\mu - H} \tag{4.24}$$

The growth and stability of the limit cycles when μ moves away from the Hopf bifurcation inside the unstable region has been studied by a combination of a two-point boundary-value scheme and Floquet theory [30]. As μ increases from H, the limit cycle grows in size while remaining stable with one Floquet multiplier being unity and the 15 remaining Floquet multipliers lying inside the unit circle. See Fig. 4.6(a) for an example of a limit cycle.

When μ passes a critical value $SH \approx 0.88215$, two of the Floquet multipliers exit the unit circle away from the real axis, signifying that SH is a secondary Hopf bifurcation. There, the limit cycle loses stability and gives way to a two-period quasiperiodic (two-torus) attractor, which is displayed in Figs. 4.6(b) and (c). The corresponding time histories suggest that the oscillations have two incommensurate periods. The FFT of δ_r seems to consist of two incommensurate frequencies, their multiples, and combinations.

As μ increases slightly above SH to $C \approx 0.89976$, the two-torus collides with its basin boundary, yielding their destruction in a bluesky catastrophe. This can be observed in Fig. 4.7, which displays the time histories of δ_r and ω_r in the vicinity of the bluesky catstrophe.

4.3 The Case of Saturation

In this section, we study the effect of the iron saturation. The parameters used are those of the CHOLLA#4 model of the Arizona Public Service Company shown in Fig. 4.2.

Figure 4.8 shows variation of the real and imaginary parts of the eigenvalues with μ. It follows from Fig. 4.8(b) that, as μ increases, the frequency of the subsynchronous electrical mode decreases and approaches the frequency of the second torsional mode (≈ 199 rad/sec) at $\mu \approx 0.842003$. Consequently, the eigenvalues associated with the second torsional mode

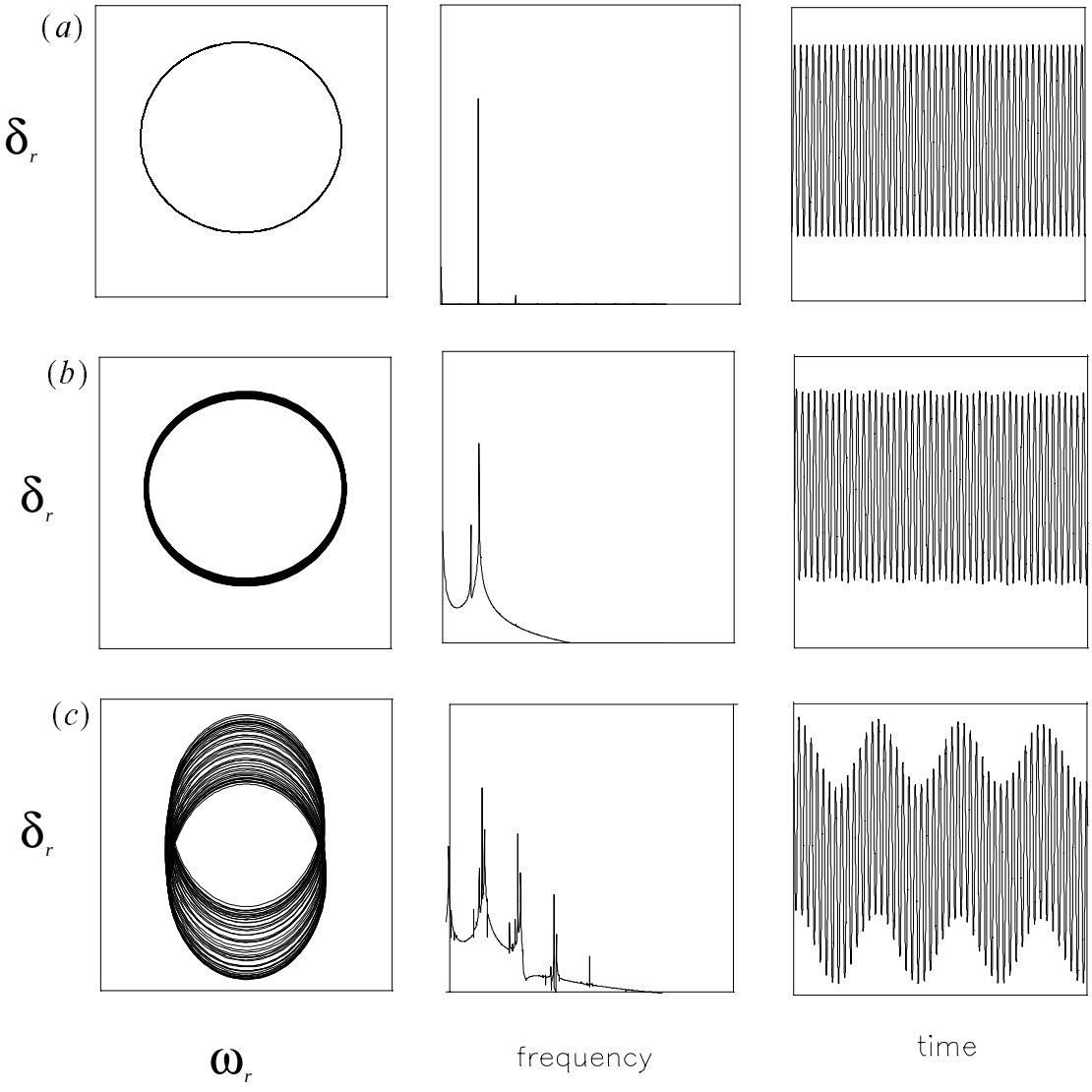

Figure 4.6: Two-dimensional projections of the phase portrait onto the $\omega_r - \delta_r$ plane(left), the FFT of the corresponding generator rotor angle δ_r (middle), and the time traces of the generator rotor angle δ_r (right) at μ = (a) 0.880981, (b) 0.88598, and (c) 0.889760. The solution at (a) is a limit cycle, at (b) is a two-torus attractor recorded well before the bluesky catastrophe, and at (c) is a two-torus attractor located just before it disappears in a bluesky catastrophe.

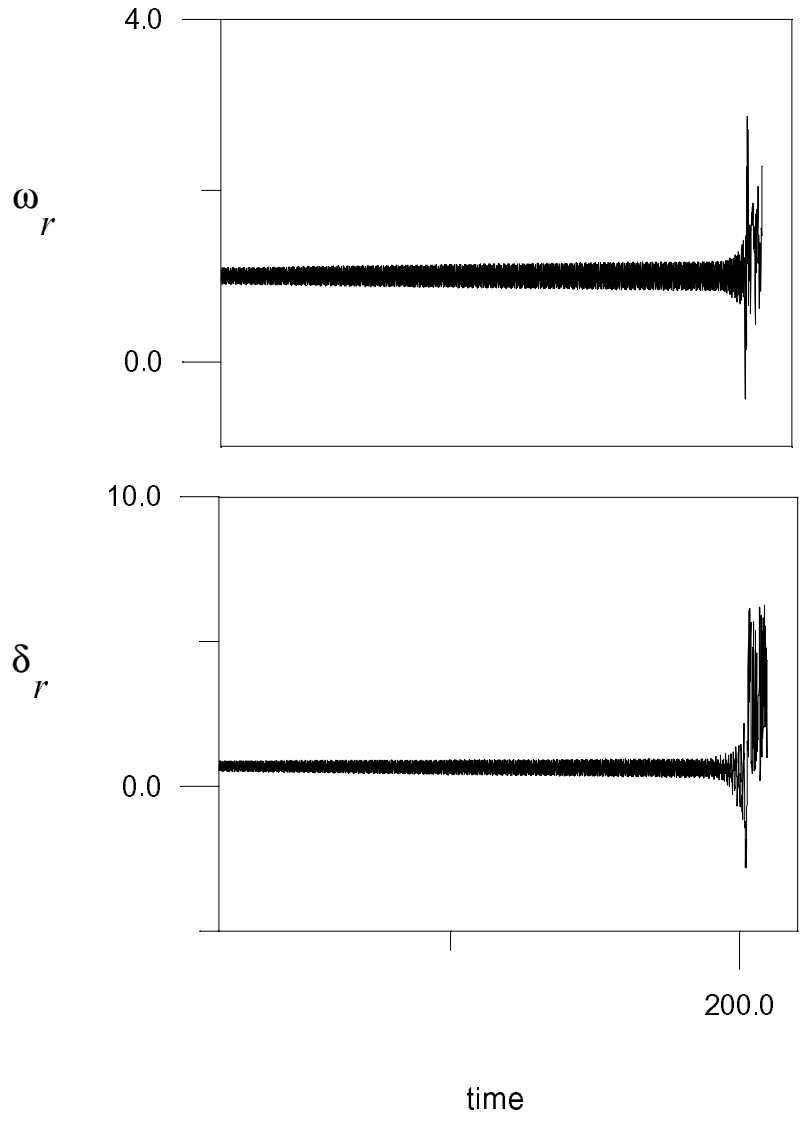

Figure 4.7: Time histories of the generator rotor speed ω_r (in rad/sec) and angle δ_r (in rad) in the vicinity of the bluesky catastrophe that occurs at $C \approx 0.89976$.

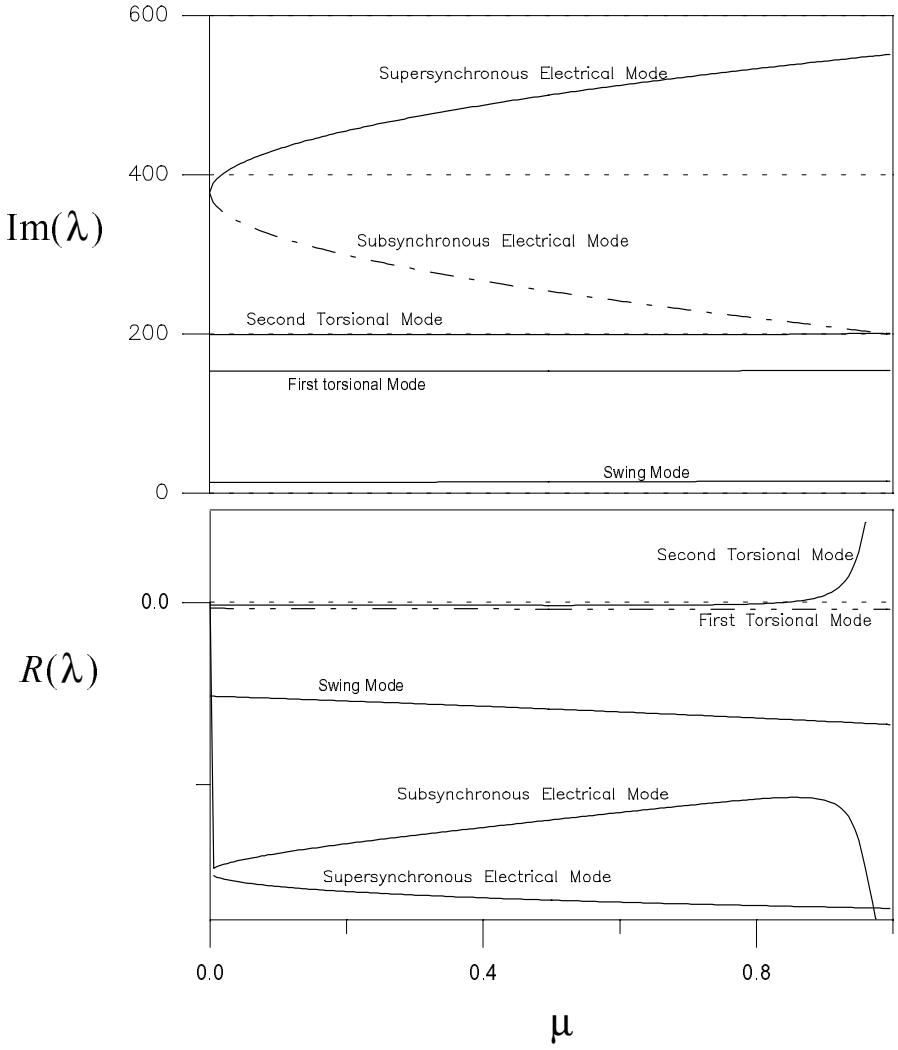

Figure 4.8: Variation of the real and imaginary parts of the eigenvalues with μ for $Q_e = 0.438, P_e = 0.9$, and $v_t = 1.0$. (With saturation)

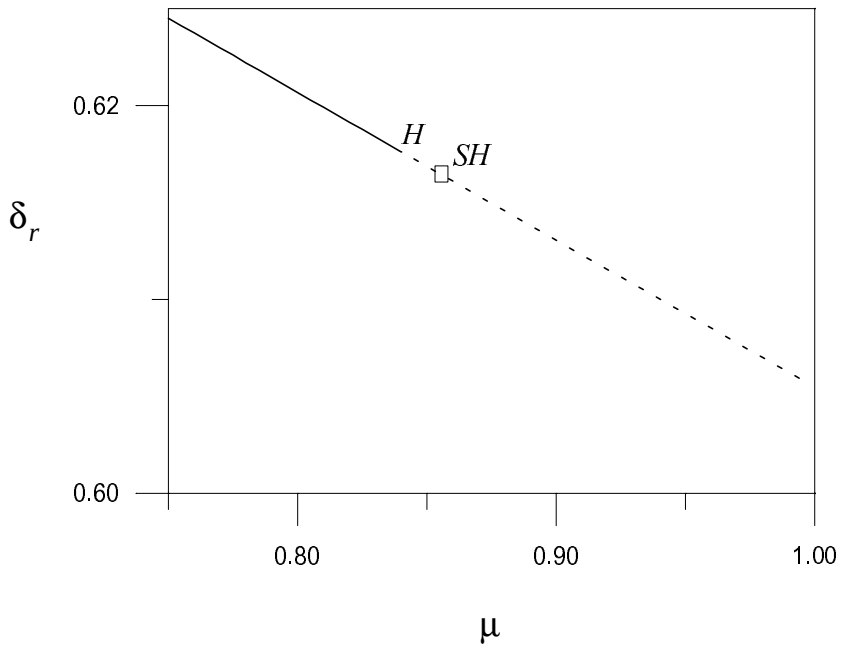

Figure 4.9: Variation of the rotor angle δ_r with the compensation level μ for the case $P_e = 0.9$, $Q_e = 0.4358$, and $v_t = 1.0$. The solid line denotes stable equilibria and the dashed line denotes unstable equilibria. The symbols H and SH indicate the compensation levels at which the Hopf and secondary Hopf bifurcations occur. (With saturation)

move to the right and cross transversely the imaginary axis into the right-half of the complex plane at $\mu = H \approx 0.842003$. There, the second torsional mode loses stability via a Hopf bifurcation, which is labeled H in Fig. 4.8.

Figure 4.9 shows variation of the rotor angle δ_r with the compensation level μ. We observe that the Hopf bifurcation point occurred at $\mu = H \approx 0.842003$. Comparing Fig. 4.4 with Fig. 4.9, we see that, in the case of saturation, the Hopf bifurcation occurs at a smaller value of μ, namely, 0.842003 compared with $\mu \approx 0.881003$ for the case of no saturation. In other words, the Hopf bifurcation point is shifted to the left. The iron saturation results in a shrinking of the positively damped region, implying a destabilization of the system. To show the destabilization of the iron saturation, we show in Fig. 4.5 variation of the loci of the Hopf bifurcation in the $P_e - \mu$ plane for $v_t = 1.0$ and $Q_e = 0.4358$. All modes located to the left of the dashed curve are positively damped whereas the second torsional mode is negatively damped to the right of the dashed curve. It follows from Fig. 4.5 that the iron saturation decreases the compensation level value at which subsynchronous resonance occurs for all values of P_e. The smaller the value of P_e is, the more the destabilization of the iron saturation is.

Again, the method of multiple scales is used to reduce the system of nonlinear ordinary-differential equations to its normal form given by Eq. (4.23) in the vicinity of the Hopf bifurcation H. For $P_e = 0.9, Q_e = 0.4358$, and $v_t = 1.0$, we find that $\beta_1 = 0.59695$ and $\beta_2 = -0.000213555$. Because $\beta_2 < 0$, the Hopf bifurcation $H \approx 0.842003$ is supercritical and the limit cycles born as a result of the bifurcation are stable. Their amplitudes are given by

$$a = 52.8705\sqrt{\mu - H} \tag{4.25}$$

Again, the growth and stability of the limit cycles has been studied by means of a combination of a two-point boundary-value scheme and Floquet theory [30]. As μ increases from H, the limit cycle grows in size while remaining stable with one Floquet multiplier being unity and the 15 remaining Floquet multipliers lying inside the unit circle. See Fig.

4.10(a) for an example of a limit cycle.

When μ increases beyond a critical value $SH \approx 0.846651$, two of the Floquet multipliers exit the unit circle away from the real axis, signifying that SH is a secondary Hopf bifurcation. There, the limit cycle loses stability and gives way to a two-period quasiperiodic (two-torus) attractor, which is displayed in Figs. 4.10(b) and (c). The corresponding time histories suggest that the oscillations have two incommensurate periods. The FFT of δ_r seems to consist of two incommensurate frequencies, their multiples, and combinations.

As μ increases slightly above SH to $C \approx 0.897651$, the two-torus collides with its basin boundary, yielding their destruction in a bluesky catastrophe. This can be observed in Fig. 4.11, which displays the time histories of δ_r and ω_r in the vicinity of the bluesky catstrophe.

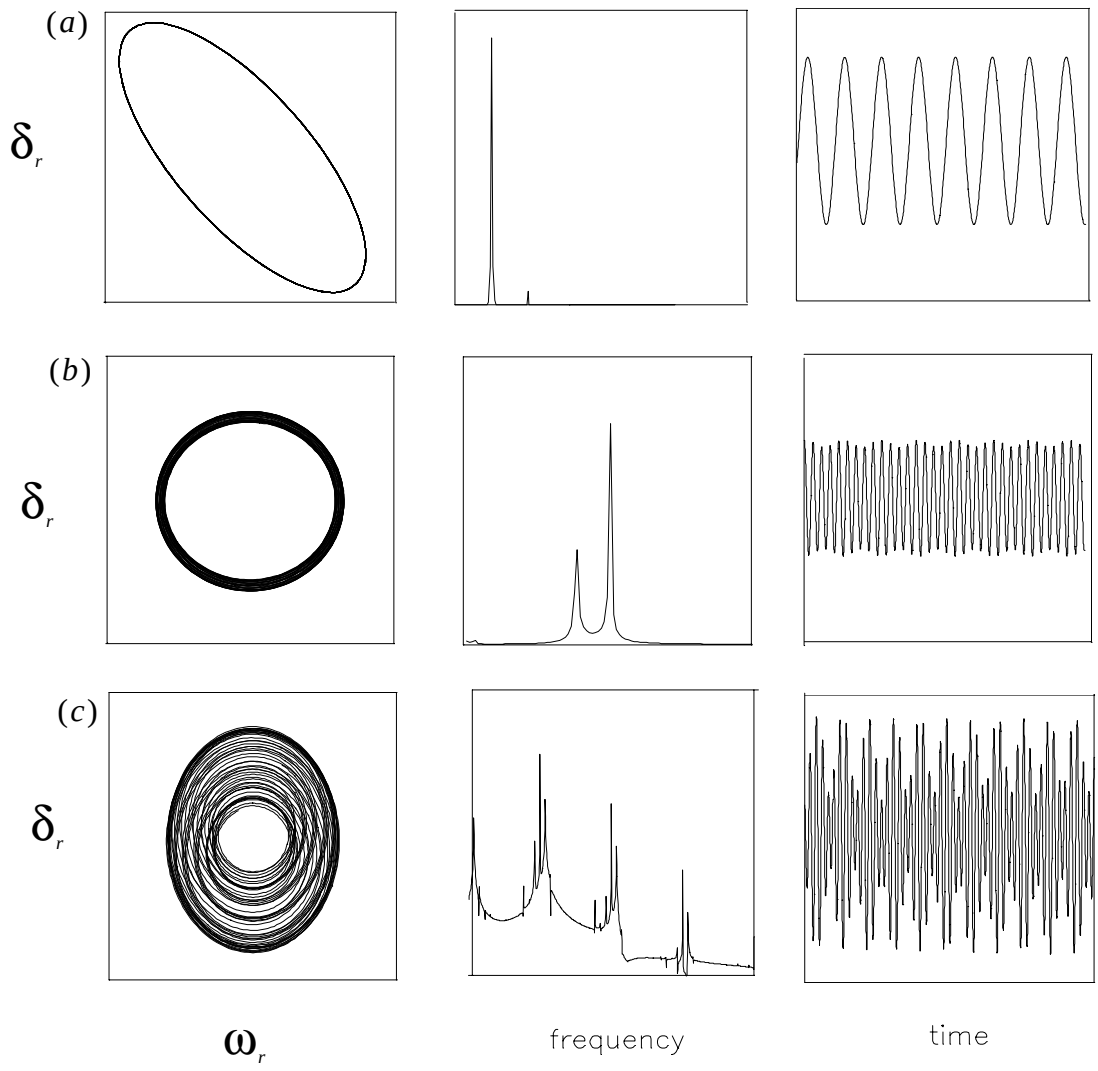

Figure 4.10: Two-dimensional projections of the phase portrait onto the $\omega_r - \delta_r$ plane(left), the FFT of the corresponding generator rotor angle δ_r (middle), and the time traces of the generator rotor angle δ_r (right) at $\mu =$ (a) 0.842351, (b) 0.848651, and (c) 0.887651. The solution at (a) is a limit cycle, at (b) is a two-torus attractor recorded well before the bluesky catastrophe, and at (c) is a two-torus attractor located just before it disappears in a bluesky catastrophe.

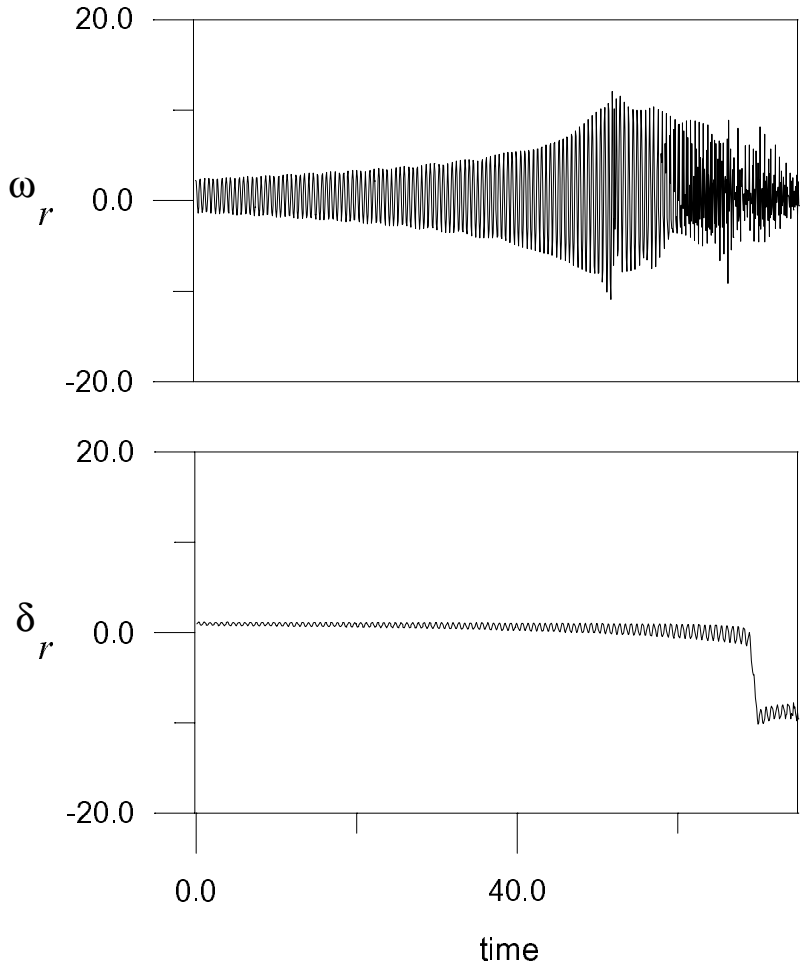

Figure 4.11: Time histories of the generator rotor speed ω_r (in rad/sec) and angle δ_r (in rad) in the vicinity of the bluesky catastrophe that occurs at $C \approx 0.8976$.

Chapter 5
CONTROL OF SSR

In this chapter, we investigate linear and nonlinear schemes to control subsynchronous resonance. Two cases have been studied. First, we analyze the CHOLLA#4 model including the dynamics of a static excitation of the ST3 type. Then, we include the dynamics of a power system stabilizer PSS. The study shows that the excitation system destabilizes the CHOLLA#4 system by shrinking the stable region, whereas the PSS stabilizes the system by expanding the stable region. A nonlinear controller that reduces the amplitudes of the limit cycles has been designed.

5.1 Excitation System

The main function of an excitation system is to provide field current to the synchronous machine. Early excitation systems were controlled manually to maintain the desired generator terminal voltage and reactive power loading [58-67]. When the voltage control was first automated, it was very slow. At the beginning of 1920, the potential for enhancing small signal and transient stability through use of continuous and fast acting regulators was recognized. In the early 1960s, the role of the excitation system was expanded by using auxiliary stabilizing signals, in addition to the terminal voltage error signal, to control the field voltage and, hence, damp off oscillations. This part of the excitation control is known as the power system stabilizer (PSS) [62 and 64].

The general functional block diagram in Fig. 5.1 indicates the various generator excitation subsystems, which are used in the studies of electric power systems. It consists of a terminal voltage transducer and load compensator, a voltage regulator, an exciter, an

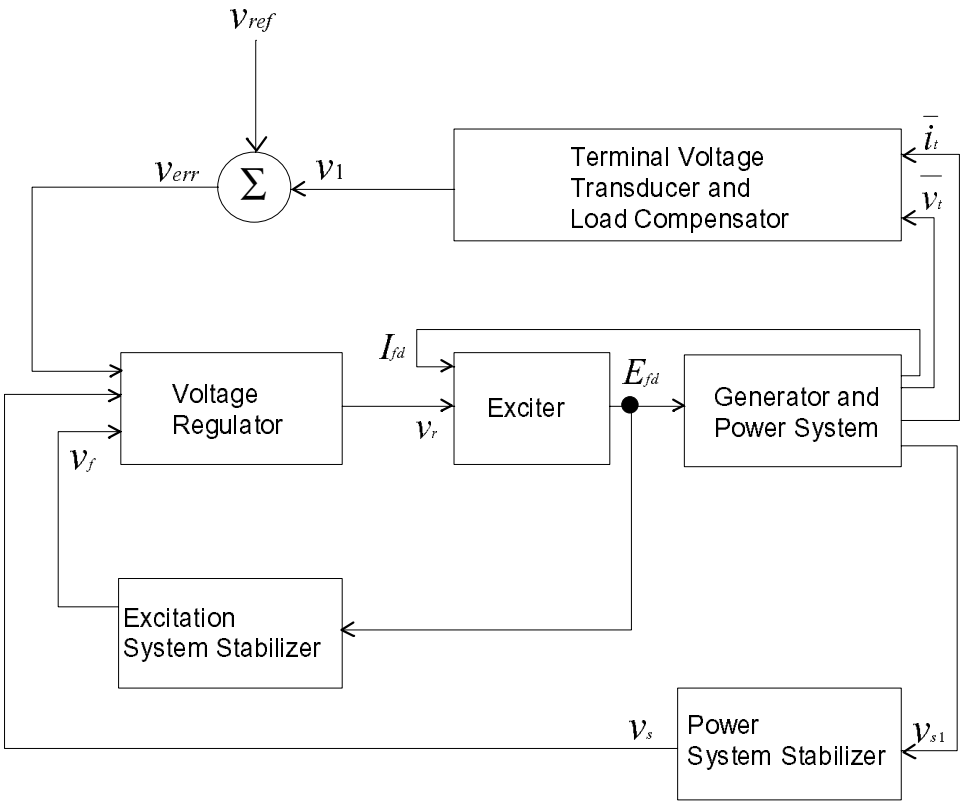

Figure 5.1: A block diagram for a generator excitation control system.

excitation system stabilizer, and in many cases, a power system stabilizer (PSS) [62].

Excitation systems can be divided into three classes based on the excitation power source that is used [62]: DC, AC, and static (ST) excitation systems. The DC excitation system utilizes a direct current generator with a commutator as the source of excitation. The AC excitation system uses an alternator and either stationary or rotating rectifiers to produce the direct current needed for the generator field windings. Finally, a ST excitation system employs transformers and rectifiers.

In this dissertation, a static excitation system is considered. Figure 5.2 shows a ST3 type compound source controlled rectifier exciter, which is known as the General Electric Static Excitation or GENEREX for short. It has been used in the CHOLLA#4 for a long

time. Its excitation system stabilizer is provided by a series lag-lead element, represented by the time constants τ_b and τ_c and the gain k_j and an inner loop field voltage regulator with the gains k_a and k_g and the time constant τ_a. The rectifier circuit is a compound of the generator terminal voltage and current.

5.2 Static Excitation System Modeling

As mentioned earlier, the static excitation system shown in Fig. 5.2 is used in the CHOLLA#4 model. Figure 5.3(a) shows the power system stabilizer PSS. The excitation system with PSS can be modeled by the following equations:

(a) Static excitation system:

$$\dot{v_1} = \frac{1}{\tau_r}(k_r v_t - v_1) \tag{5.1}$$

$$\dot{v_a} = \frac{1}{\tau_b}[k_j(v_{ref} - v_1 - \tau_c\dot{v_1} + v_s + \tau_c\dot{v_s} - v_{nc} - \tau_c\dot{v_{nc}}) - v_a] \tag{5.2}$$

$$\dot{v_r} = \frac{1}{\tau_a}[k_a(v_a - k_g E_{fd}) - v_r] \tag{5.3}$$

(b) Power system stabilizer PSS:

$$y_1 + a_1\dot{y_1} + a_2\ddot{y_1} = v_{s1} \tag{5.4}$$

$$y_2 + \tau_2\dot{y_2} = y_1 + \tau_1\dot{y_1} \tag{5.5}$$

$$y_3 + \tau_4\dot{y_3} = y_2 + \tau_3\dot{y_2} \tag{5.6}$$

$$v_s + \tau_5\dot{v_s} = k_s\tau_5\dot{y_3} \tag{5.7}$$

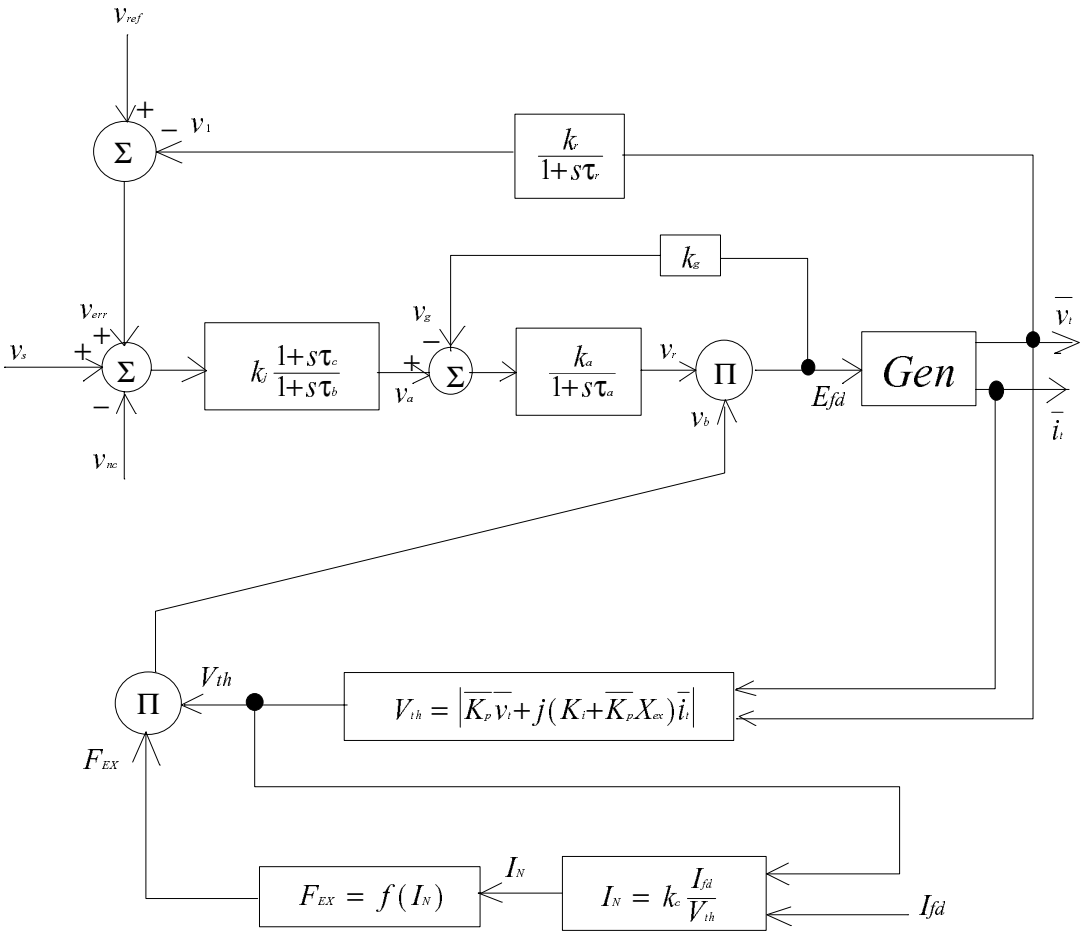

$$\overline{K}_p = K_p e^{j\theta_p} = k_{pr} + jk_{pi}$$

$$f(I_N) = 1 - 0.58 I_N \quad \text{when} \quad I_N \le 0.433$$
$$= \sqrt{0.75 - (I_N)^2} \quad \text{when} \quad 0.433 < I_N > 0.75$$
$$= 1.732(1 - I_N) \quad \text{when} \quad 1.0 \ge I_N \ge 0.75$$

Figure 5.2: A static excitation system of the ST3 type, which is a compound source controlled rectifier exciter (GENEREX).

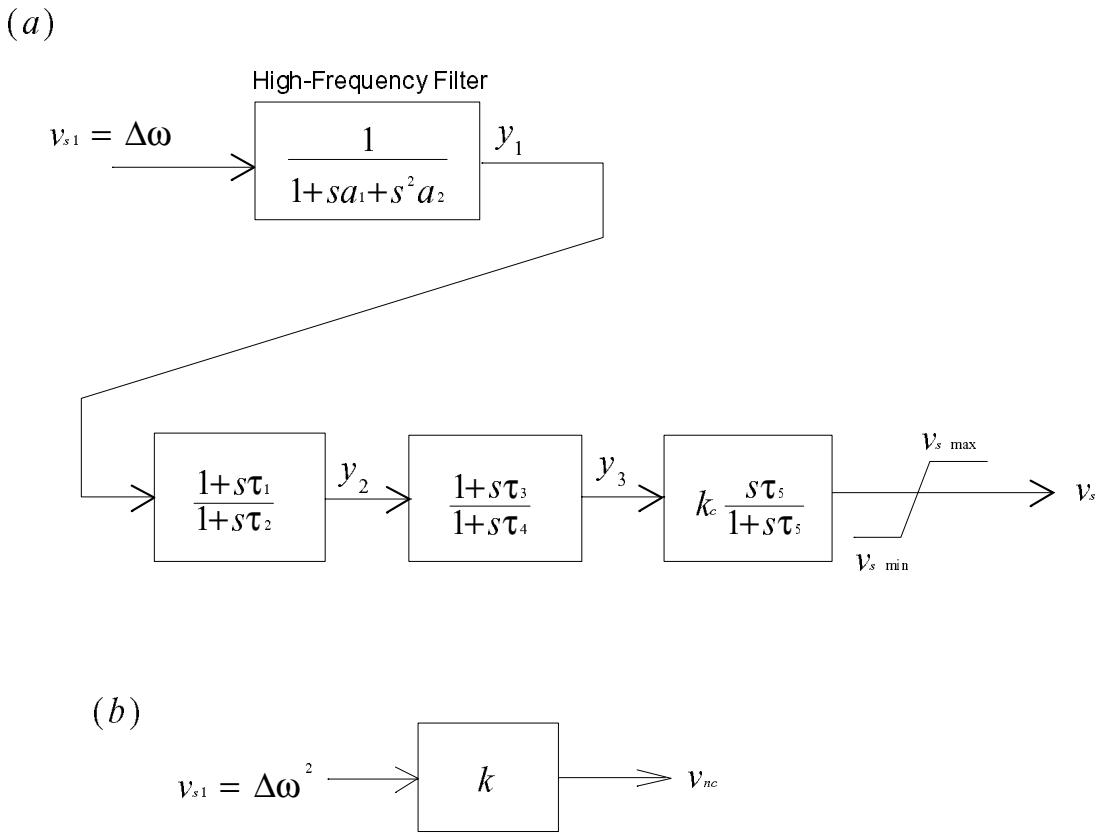

Figure 5.3: a) Power system stabilizer (PSS) and b) nonlinear controller.

Here, v_t is the terminal generator voltage; v_1 is the output of the terminal transducer; k_r and τ_r are the gain and time constant of the transducer, respectively; v_a is the regulator internal voltage; v_s is the power system stabilizer output; v_{nc} is the quadratic controller output signal; τ_a,τ_b, and τ_c are the voltage regulator time constants; v_{ref} is the reference voltage; v_r is the voltage regulator output; E_{fd} is the exciter output voltage (generator field voltage); k_a is the voltage regulator gain; k_g is the inner loop feedback constant; a_1 and a_2 are the PSS high frequency filter constants; v_{s1} is the power system stabilizer input; τ_1 and τ_3 are the PSS lead compensating time constants; τ_2 and τ_4 are the PSS lag compensating time constants; τ_5 is the PSS washout time constant; and k_s is the power system stabilizer gain.

Equations (5.1)-(5.3) represent the dynamics of the static exciter and Eqs. (5.4)-(5.7) represent the dynamics of the power system stabilizer. The total number of equations that describe the system is 23. The first 16 equations represent the system, which was described in Chapter 4, while the remaining 7 equations represent the dynamics of the excitation system with PSS. In addition to the parameters given in Chapter 4, we let

$k_j = 200,\ \ \tau_b = 10,\ \ \tau_c = 1.0,\ \ k_c = 1.13,\ \ \tau_a = 1.0,$

$k_a = 7.97,\ \ k_g = 1.0,\ \ k_r = 1.0,\ \ \tau_r = 0.001,\ \ v_{rmax} = 1.0,$

$v_{rmin} = 0.0\ \ a_1 = 0.061,\ \ a_2 = 0.0017,$

$\tau_1 = 0.3,\ \ \tau_2 = 0.03,\ \ \tau_3 = 0.3,\ \ \tau_4 = 0.03,\ \ \tau_5 = 10.0,$

$k_s = 5.0,\ \ v_{smax} = 0.05,\ \ v_{smin} = -0.05,\ \ \text{and}\ k = 0$

Again all the voltages are given in p.u. and the time constants are given in seconds. When the PSS and the nonlinear controller are neglected, we set $v_s = v_{nc} = 0$ in Eq. (5.2) and obtain

$$\dot{v_a} = \frac{1}{\tau_b}[k_j(v_{ref} - v_1 - \tau_c \dot{v_1}) - v_a] \tag{5.8}$$

5.3 Operating Conditions and Their Stability

The operating conditions (equilibrium solutions or points) can be obtained by setting the derivatives of the state variables in the system of equations (4.7)-(4.22), (5.1), (5.3), and (5.8) equal to zero. The result is

$$(R_\ell + R_a)i_d - X_\ell i_q + e_{cd} + v_0 \sin\delta_r + \psi_q = 0 \tag{5.9}$$

$$X_\ell i_d + (R_\ell + R_a)i_q + e_{cq} + v_0 \cos\delta_r - \psi_d = 0 \tag{5.10}$$

$$v_f - R_f i_f = 0 \tag{5.11}$$

$$e_{cd} = \mu X_\ell i_q \tag{5.12}$$

$$e_{cq} = -\mu X_\ell i_d \tag{5.13}$$

$$T_m = i_q\psi_d - i_d\psi_q \tag{5.14}$$

$$\omega_r = \omega_1 = \omega_2 = \omega_3 = \omega_4 = 1 \tag{5.15}$$

$$\delta_r = \theta_1 = \theta_2 = \theta_3 = \theta_4 \tag{5.16}$$

$$k_r(v_d^2 + v_q^2)^{\frac{1}{2}} - v_1 = 0 \tag{5.17}$$

$$k_j(v_{ref} - v_1) - v_a = 0 \tag{5.18}$$

$$k_a(v_a - k_g v_r v_b) - v_r = 0 \tag{5.19}$$

Instead of specifying T_m and v_0, one usually specifies the real P_e and reactive Q_e powers. In p.u., these control parameters are related to the voltages and currents through

$$P_e = v_d i_d + v_q i_q \tag{5.20}$$

$$Q_e = v_q i_d - v_d i_q \tag{5.21}$$

To relate the voltages v_d and v_q to the currents i_d, i_q, and i_f, we note that, at the operating condition, Eqs. (3.1) and (3.2) reduce to

$$v_d = -R_a i_d - \psi_q \tag{5.22}$$

$$v_q = -R_a i_q + \psi_d \tag{5.23}$$

Using Eqs. (4.3) and (4.4) to eliminate ψ_d and ψ_q from Eqs. (5.9), (5.10), (5.14), (5.22), and (5.23) yields

$$(R_\ell + R_a)i_d - X_\ell i_q + \mu X_\ell i_q + v_0 \sin\delta_r + [q_0 - q_1 i_q + q_2 i_q^2 - q_3 i_q^3 - X_{le} i_q] = 0 \tag{5.24}$$

$$\begin{aligned} X_\ell i_d + (R_\ell + R_a)i_q - \mu X_\ell i_d + v_0 \cos\delta_r \\ -[d_0 + d_1(-i_d + i_f) + d_2(-i_d + i_f)^2 + d_3(-i_d + i_f)^3 - X_{le} i_d] = 0 \end{aligned} \tag{5.25}$$

$$\begin{aligned} T_m = i_q[d_0 + d_1(-i_d + i_f) + d_2(-i_d + i_f)^2 + d_3(-i_d + i_f)^3 - X_{le} i_d] \\ -i_d[q_0 - q_1 i_q + q_2 i_q^2 - q_3 i_q^3 - X_{le} i_q] \end{aligned} \tag{5.26}$$

$$v_d = -R_a i_d - [q_0 - q_1 i_q + q_2 i_q^2 - q_3 i_q^3 - X_{le} i_q] \tag{5.27}$$

$$v_q = -R_a i_q + [d_0 + d_1(-i_d + i_f) + d_2(-i_d + i_f)^2 + d_3(-i_d + i_f)^3 - X_{le} i_d] \tag{5.28}$$

where

$$v_f = v_b v_r \frac{R_f}{d_1} = R_f i_f \tag{5.29}$$

$$\begin{aligned} v_b &= [(w_1^2 + w_2^2)^{\frac{1}{2}} - 0.58 k_c d_1 i_f] \quad \text{when} \quad I_N \le 0.433 \\ &= [0.75(w_1^2 + w_2^2) - (d_1 i_f k_c)^2]^{\frac{1}{2}} \text{ when } 0.75 < I_N < 0.433 \\ &= 1.732[(w_1^2 + w_2^2)^{\frac{1}{2}} - k_c d_1 i_f] \text{ when } 1.0 \ge I_N \ge 0.75 \end{aligned} \tag{5.30}$$

$$I_N = \frac{k_c d_1 i_f}{(w_1^2 + w_2^2)^{\frac{1}{2}}} \tag{5.31}$$

$$w_1 = k_{pr} v_d - k_{pi} v_q - K_I i_q - k_{pr} X_{ex} i_q - k_{pi} X_{ex} i_d \tag{5.32}$$

$$w_2 = k_{pi} v_d + k_{pr} v_q + K_I i_d + k_{pr} X_{ex} i_d - k_{pi} X_{ex} i_q \tag{5.33}$$

Given P_e, Q_e, and $\mu = X_c/X_\ell$, we solve the algebraic system of ten equations given by Eqs. (5.11), (5.17)-(5.21), (5.24), (5.25), and (5.27)-(5.28) to determine the nine state

variables i_d, i_q, i_f, v_d, v_q, v_1, v_a, v_r, and δ_r and the control parameter v_0. Then, we calculate T_m from Eq. (5.26), thereby determining the operating condition and the control parameters v_0 and T_m. Using an arclength continuation scheme [30], we calculate variation of the operating condition (equilibrium point) with the control parameter μ.

The stability of a given equilibrium point is ascertained by examination of the eigenvalues of the Jacobian matrix J of equations (4.7)-(4.22), (5.1)-(5.3), and (5.36)-(5.40) evaluated at the equilibrium point. The equilibrium point is stable if all of the eigenvalues of the Jacobian matrix lie in the left-half of the complex plane and unstable if at least one eigenvalue lies in the right-half of the complex plane.

5.4 The Case without PSS

In this section, we study the effect of the excitation system without PSS on subsynchronous resonance using the modern methods of nonlinear dynamics.

When $P_e = 0.9$ and $Q_e = 0.4358$, we show in Fig. 5.4 variation of the real and imaginary parts of the eigenvalues with μ. There are 14 complex and five real eigenvalues. Because the Jacobian matrix is real, the complex conjugate of each complex value is an eigenvalue, yielding 7 oscillatory modes. Two modes are electrical modes and 5 are mechanical modes. The mode with the lowest frequency is the swing or electro-mechanical mode whereas the other four mechanical modes are torsional modes. Two of the torsional modes, the third and fourth modes, are damped and have very high frequencies, namely, 1030 and 1450 rad/sec. Hence, they do not interact with the electrical modes for realistic compensation levels. The five real eigenvalues are negative, two are associated with the field and damper windings, while the other three are associated with the excitation system.

For small μ, the frequencies of the electrical modes are approximately 377 rad/sec. As μ increases, the supersynchronous and subsynchronous frequencies separate from each other. As for the BOARDMAN system, the supersynchronous mode is highly damped whereas the subsynchronous is not. We will focus on the subsynchronous frequency and how its

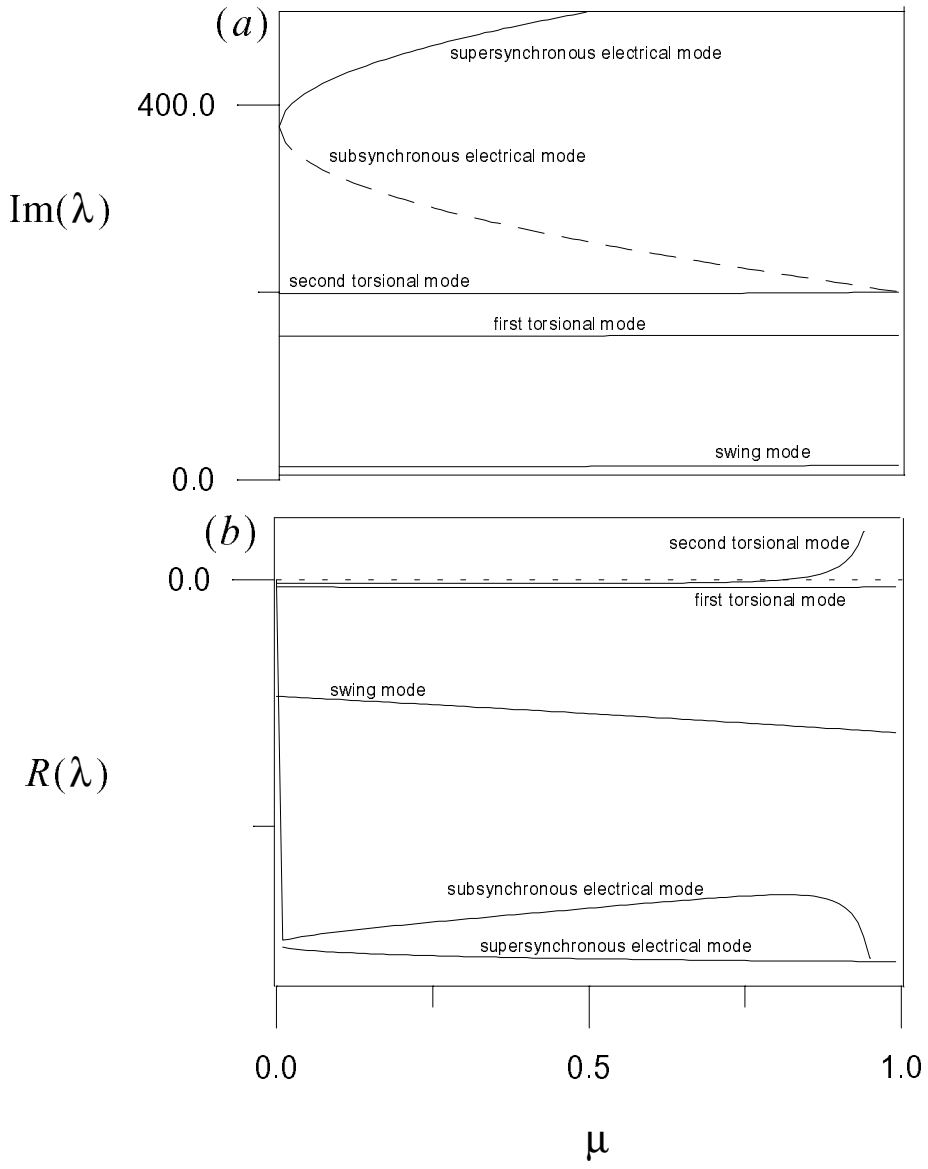

Figure 5.4: Variation of the real and imaginary parts of the eigenvalues with μ for $Q_e = 0.4358$ and $P_e = 0.9$, (Without PSS)

associated mode interacts with the second and first torsional modes.

It follows from Fig. 5.4(a) that, as μ increases, the frequency of the subsynchronous electrical mode decreases and approaches the frequency of the second torsional mode (≈ 199 rad/sec) at $\mu \approx 0.819$. Consequently, the eigenvalues associated with the second torsional mode move to the right and cross transversely the imaginary axis into the right-half of the complex plane at $\mu = H \approx 0.819$. Consequently, the second torsional mode loses stability via a Hopf bifurcation, which is labeled H in Fig. 5.5. In the present case, the frequency of the electrical mode intersects the second torsional mode for values of $\mu < 1.0$, resulting in one interaction region. Once the equilibrium point loses stability due to this interaction, it does not regain it for any larger value of μ. Consequently, we conclude that there is only one Hopf bifurcation point.

Figure 5.5 shows variation of the generator rotor angle δ_r with the compensation level μ. One can see that the Hopf bifurcation point H is shifted to the left from $\mu = 0.842$ to $\mu = 0.819$. In other words, the positively damped region or the stable region is decreased. So, the excitation system is destabilizing the system.

We now resort to the method of multiple scales to reduce the new system of 19 first-order nonlinear ordinary-differential equations to its normal form near the Hopf bifurcation point H at $\mu = \mu_o$. For $P_e = 0.9$ and $Q_e = 0.4358$, variation of the amplitude a of the oscillations with time near H of Fig. 5.5 is given by

$$a^{'} = (\mu - H)\beta_1 a + \beta_2 a^3 \tag{5.34}$$

with $\beta_1 = 0.523413$ and $\beta_2 = -0.000623183$. Thus, the Hopf bifurcation $H \approx 0.819$ is supercritical and the limit cycles born as a result of the bifurcation are stable. Their amplitudes are given by

$$a = 28.98\sqrt{\mu - H} \tag{5.35}$$

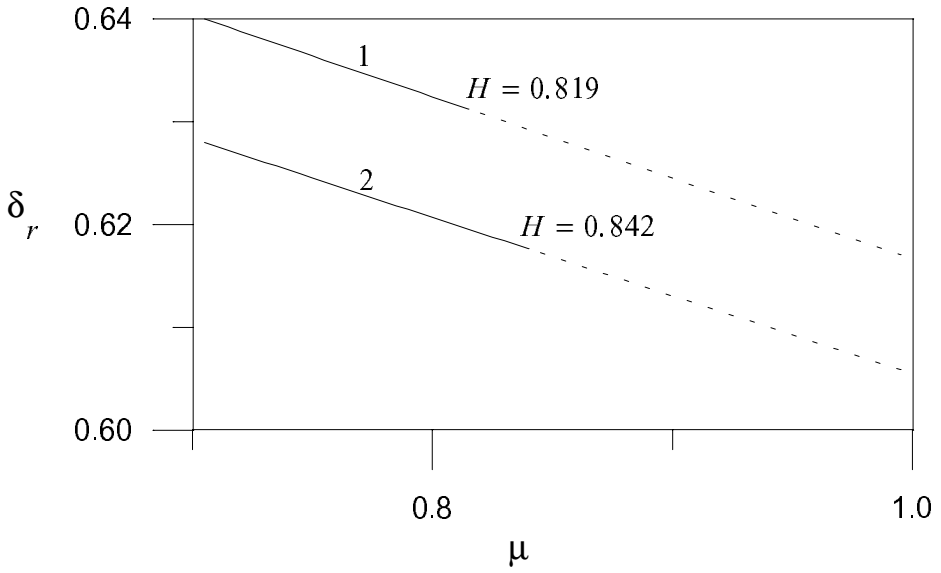

Figure 5.5: Bifurcation diagram showing variation of the generator rotor angle δ_r with the compensation level μ. Line 2 corresponds to the case without the excitation system and the PSS, and line 1 corresponds to the case with the excitation system only. The solid lines denote sinks and the dashed lines denote unstable foci.

5.5 The Case with PSS

The main function of PSS is to improve the dynamic stability of power systems. Intensive effort to improve power system stability has resulted in the widespread use of other regulator input signals in addition to the terminal voltage. These signals are chosen to provide positive damping to the oscillations [62]. In synchronous condenser applications, the objective most frequently used is to minimize voltage swings. Figure 5.3(a) shows the generalized form of such a power system stabilizer. Some common stabilizer input signals include accelerating power, speed deviation, frequency deviation, and terminal voltage. They are designated by v_{s1}.

The first block represents a high-frequency filter. The next two blocks allow two stages of lead-lag compensation. The stabilizer gain is set by k_s and signal washout is set by the time constant τ_5. The stabilizer output can be limited in many ways. Figure 5.3(a) shows simple output limits. In other systems, the stabilizer output is limited by the generator terminal voltage. The stabilizer output v_s is added to the terminal voltage error signal at the location shown in Fig. 5.2.

The dynamics of the PSS, which is shown in Fig. 5.3(a) and given by Eqs. (5.4)-(5.7), consists of a second-order ordinary-differential equation and three first-order ordinary-differential equations. We let $y_1 = x_1$ and $\dot{y_1} = x_2$ and rewrite Eqs. (5.4)-(5.7) as

$$\dot{x_1} = x_2 \tag{5.36}$$

$$\dot{x_2} = \frac{1}{a_2}(v_{s1} - x_1 - a_1 x_2) \tag{5.37}$$

$$\dot{y_2} = \frac{1}{\tau_2}(x_1 + \tau_1 x_2 - y_2) \tag{5.38}$$

$$\dot{y_3} = \frac{1}{\tau_4}(y_2 + \tau_3 \dot{y_2} - y_3) \tag{5.39}$$

$$\dot{v_s} = \frac{1}{\tau_5}(k_s\tau_5 y_3 - v_s) \tag{5.40}$$

Equations (5.36)-(5.40) represent the dynamics of the power system stabilizer. Again, we use bifurcation theory to analyze the new system. It consists of 24 first-order nonlinear ordinary- differential equations. The first 16 equations represent the system, which is described in Chapter 4, the next three equations represent the dynamics of the excitation system, while the last 5 equations represent the dynamics of the power system stabilizer.

Again, when $P_e = 0.9$ and $Q_e = 0.4358$, we show in Fig. 5.6 variation of the real and imaginary parts of the eigenvalues with μ. There are 18 complex and six real eigenvalues. Because the Jacobian matrix is real, the complex conjugate of each complex value is an eigenvalue, yielding 9 oscillatory modes. Four modes are electrical modes and 5 are mechanical modes. The mode with the lowest frequency is the swing or electro-mechanical mode whereas the other four mechanical modes are torsional modes. Two of the electrical modes, which are associated with the PSS, are very highly damped and have low frequencies, namely, 18 and 27 rad/sec. Hence, they do not interact with the subsynchronous electrical mode for realistic compensation levels. Also, two of the torsional modes, the third and the fourth modes, are damped and have very high frequencies, namely, 1030 and 1450 rad/sec. Hence, they do not interact with the electrical modes for realistic compensation levels. So, these four modes do not show up in Fig. 5.3. The six real eigenvalues are negative, two are associated with the field and damper windings, while the other four are associated with the excitation system with PSS.

Figure 5.6 shows variation of the real and imaginary parts of the eigenvalues with μ. It follows from Fig. 5.6(b) that, as μ increases, the frequency of the subsynchronous electrical mode decreases and approaches the frequency of the second torsional mode (≈ 199 rad/sec) at $\mu \approx 0.8254$. Consequently, the eigenvalues associated with the second torsional mode move to the right and cross transversely the imaginary axis into the right-half of the complex plane at $\mu = H \approx 0.8254$. There, the second torsional mode loses stability via a Hopf

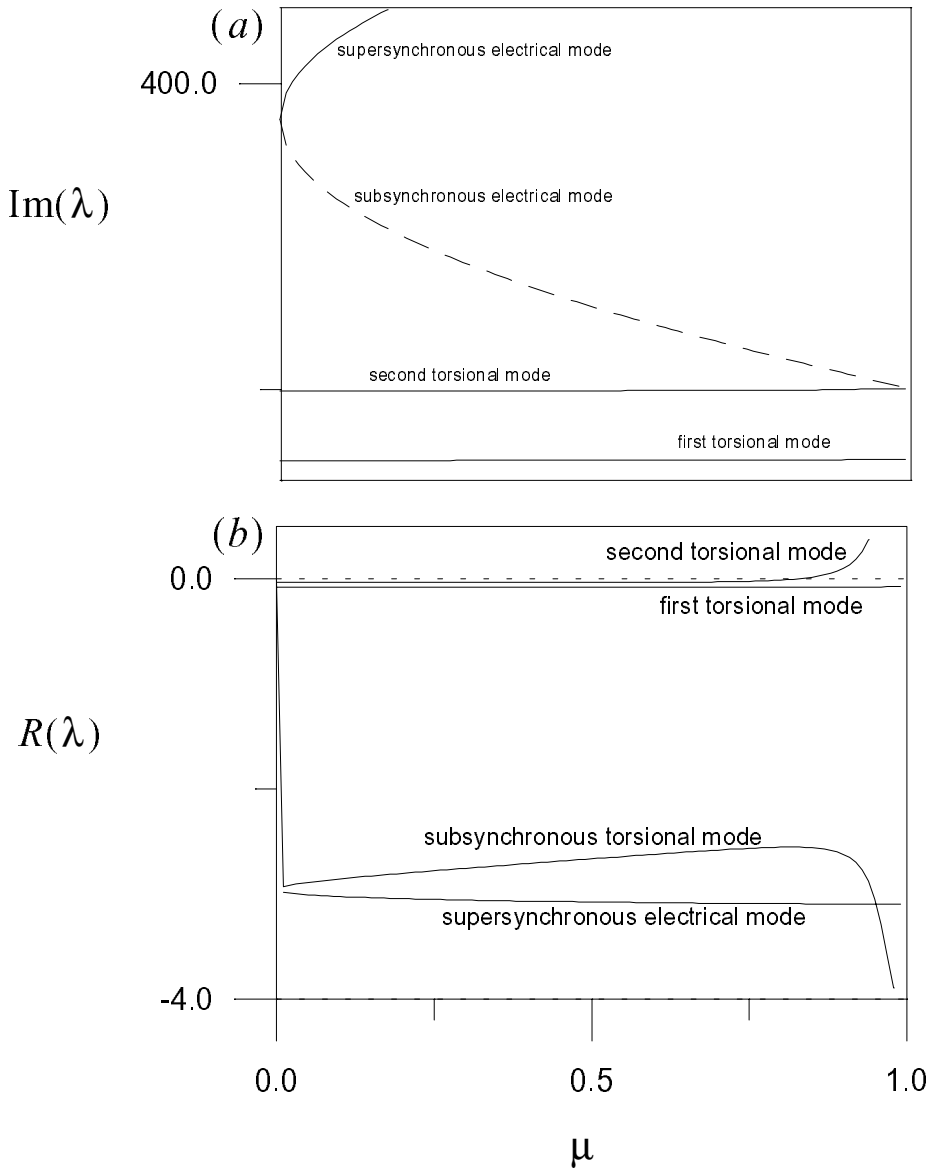

Figure 5.6: Variation of the real and imaginary parts of the eigenvalues with μ for $Q_e = 0.4358$ and $P_e = 0.9$, (With PSS)

bifurcation, which is labeled H in Fig. 5.7.

Figure 5.7 shows variation of the generator rotor angle δ_r with the compensation level μ. Clearly the Hopf bifurcation point H is shifted to the right from $\mu = 0.819$ to $\mu = 0.8254$. In other words, the positively damped region or the stable region is increased. So, the power system stabilizer PSS is stabilizing the system, in agreement with Yu [13].

For $P_e = 0.9$ and $Q_e = 0.4358$, we display in Figs. 5.8 variation of the loci of the Hopf bifurcation points in the $k_j - \mu$ plane. When the voltage regulator time constant $\tau_a = 0.4$ second, the Hopf bifurcation point slightly shifts to the right as the voltage regulator gain k_j increases from 200 up to 300, thereby increasing the positively damped region.

In Fig. 5.9, we show variation of the loci of the Hopf bifurcation points in the $\tau_a - \mu$ plane for $k_j = 200$. As τ_a increases the Hopf bifurcation point moves rapidly to the right, increasing the stability region until τ_a reaches 0.4. As τ_a increases further, the Hopf bifurcation point moves slightly to the left. Therefore $\tau_a \approx 0.4$ is the optimum value.

Again, the method of multiple scales is used to reduce the new system of 24 first-order nonlinear ordinary-differential equations to its normal form Eq. (4.34) near the Hopf bifurcation point H at $\mu = 0.8254$. For $P_e = 0.9$ and $Q_e = 0.4358$, $\beta_1 = 0.573439$ and $\beta_2 = -0.0000349514$. Thus, the Hopf bifurcation $H \approx 0.8254$ is supercritical and the limit cycles born as a result of the bifurcation are stable. Their amplitudes are given by

$$a = 128.089\sqrt{\mu - H} \tag{5.41}$$

5.6 Nonlinear Controller

A nonlinear controller that reduces the amplitudes of the nonlinear torsional oscillations has been designed. As depicted in Fig. 5.3 (b), it uses the generator rotor frequency deviation as the input signal to the excitation system . The signal is squarred, multiplied by a gain k, and the output signal v_{nc} is injected through an additional feedback loop into the excitation system shown in Fig. 5.2. Because the equilibria of Eqs. (4.7)-(4.22), (5.1),

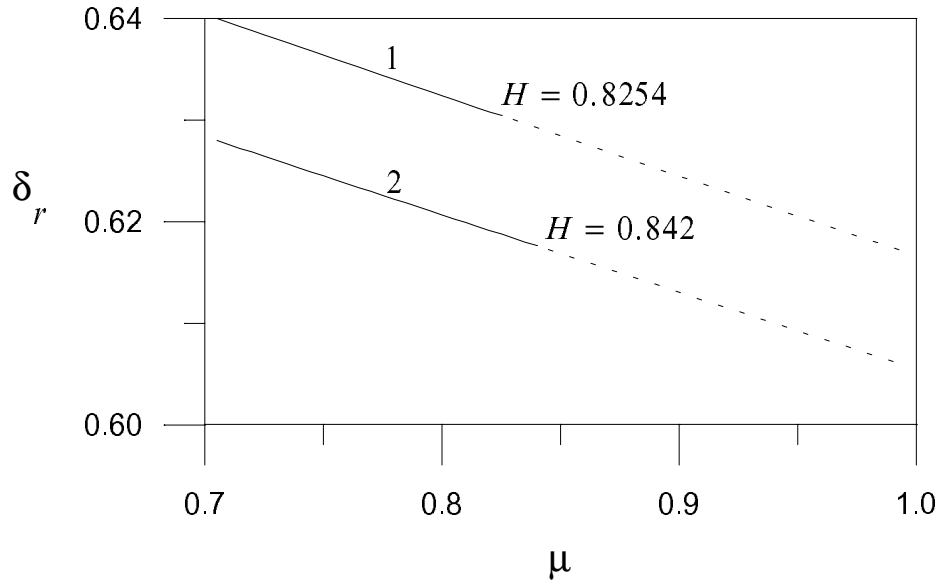

Figure 5.7: Bifurcation diagram showing variation of the generator rotor angle δ_r with the compensation level μ. Line 2 corresponds to the case without the excitation system and the PSS, and line 1 corresponds to the case with the excitation system and the PSS. The solid lines denote sinks and the dashed lines denote unstable foci.

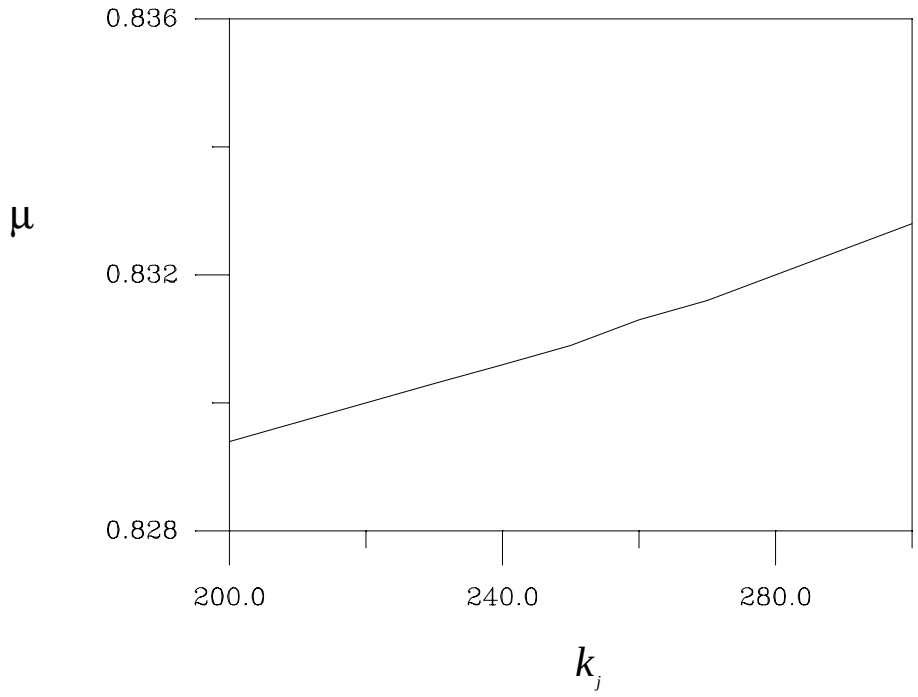

Figure 5.8: Variation of the loci of the Hopf bifurcation points with k_j when $P_e = 0.9$ and $Q_e = -0.2$, and $\tau_a = 0.4$.

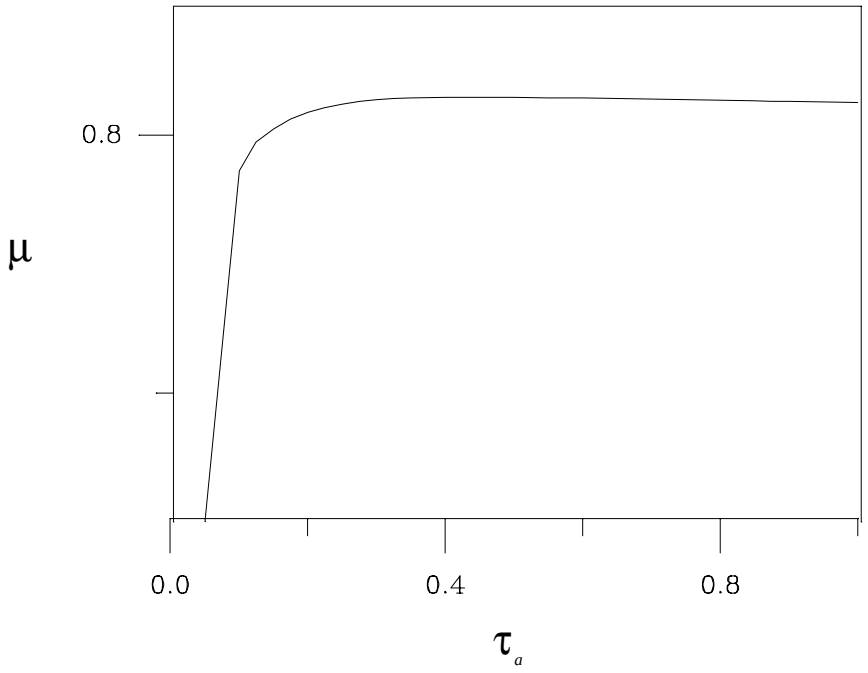

Figure 5.9: Variation of the loci of the Hopf bifurcation points with τ_a when $P_e = 0.9$ and $Q_e = -0.2$, and $k_j = 200$.

(5.3), (5.8), and (5.36)-(5.40) correspond to $\Delta\omega = 0$, this nonlinear controller does not affect their locations. Moreover, because the cotribution of this nonlinear controller to the Jacobian matrix of Eqs. (4.7)-(4.22), (5.1), (5.3), (5.8), and (5.36)-(5.40) evaluated at the equilibria is zero, it does not affect their linear stability. However, this nonlinear controller can have a significant effect on the dynamic behavior of the system. In other words, the nonlinear controller does not affect the operating condition and the location of the Hopf bifurcation, but it strongly affect the nonlinear behaviour of the power system.

Again, using the method of multiple scales, we reduce Eqs. (4.7)-(4.22), (5.1), (5.3), (5.8), and (5.36)-(5.40) into the normal form given by Eq. (5.34) with β_2 being replaced with

$$\hat{\beta}_2 = \beta_2 + k\beta_{21} + k^2\beta_{22} \tag{5.42}$$

To study the effect of the gain on the performance of controller, we carry out a bifurcation analysis as follows. For $k = 100$, we find that $\hat{\beta}_2 = -0.00257164$. Thus, the Hopf bifurcation $H \approx 0.8254$ remains supercritical and the limit cycles born as a result of the bifurcations remain stable. Their amplitudes are given by

$$a = 14.9327\sqrt{\mu - H} \tag{5.43}$$

For $k = 500$, we find that $\hat{\beta}_2 = -0.0127184$. Thus, the Hopf bifurcation $H \approx 0.8254$ remains supercritical and the limit cycles born as a result of the bifurcations remain stable. However, their amplitudes reduced to

$$a = 6.7147\sqrt{\mu - H} \tag{5.44}$$

Using the value of $\hat{\beta}_2$ at $k = 0, 100$ and 500, we find that, the coefficients in Eq. (5.42) are $\beta_{21} = -2.5366 \times 10^{-5}$ and $\beta_{22} = -7.55 \times 10^{-14}$. With these values, we show in Fig. 5.10, variation of a, the amplitude of the limit-cycle born at H, with k. Because β_2 is negative, the Hopf bifurcation $H = 0.8254$ remains supercritical. Because $\mid \hat{\beta}_2 \mid$ increases

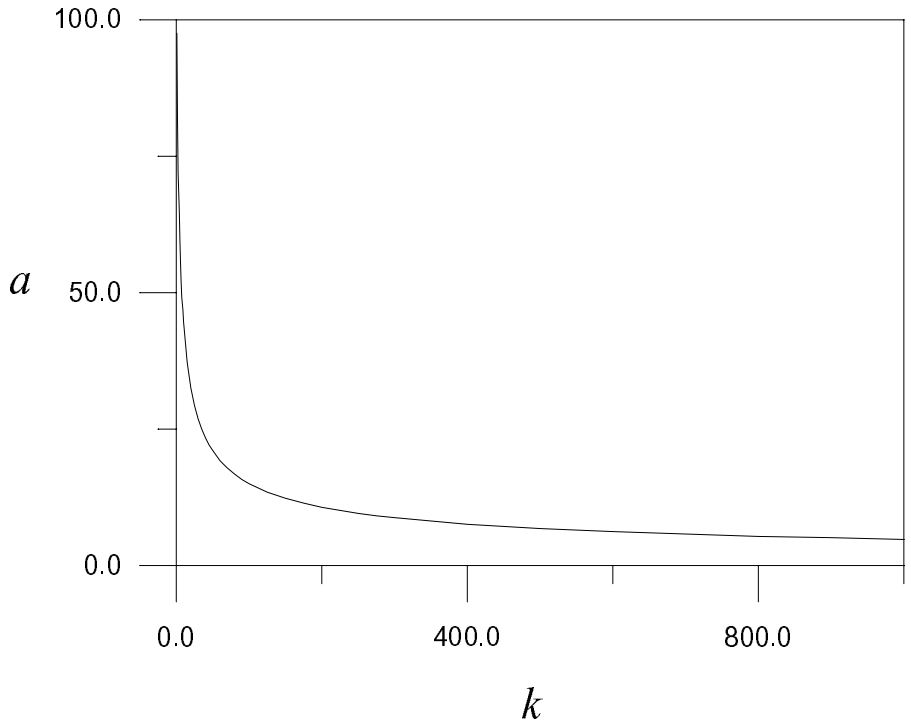

Figure 5.10: Variation of a, the amplitude of the limit-cycle born at H, with the nonlinear controller gain k.

as k increases, the larger the value of k is, the smaller the amplitude of the limit-cycle born at H is. Further increases in the gain k, one can suppress the secondary Hopf bifurcation and hence the bluesky catastrophe.

Chapter 6

CONCLUSIONS

We have applied bifurcation theory together with the method of normal forms and Floquet theory to a two practical series capacitor-compensated-single-machine power systems: the BOARDMAN and CHOLLA#4 turbine-generator systems. For the BOARDMAN system, we have revealed the existence of complex self-excited oscillations of the turbine-generator rotor, such as limit cycles and two-torus attractors, for practical compensation values. We have shown that they result from a strong interaction of the subsynchronous electrical mode with either the second or third mechanical mode of a 5-mass rotor. These oscillations can cause loss of fatigue life of the turbine-generator shaft and, ultimately, can lead to its break with disastrous consequences. For high compensation values, they may induce loss of synchronism of the generator following the disappearance of the two-torus attractor and its basin of attraction in a bluesky catastrophe. Next, we investigate the influence of adding damper windings along the q- and d-axes on subsynchronous resonance. The study shows that these damper windings affect the locations and the type of the Hopf bifurcations. Adding q-axis damper windings shifts the Hopf bifurcation to smaller values of μ and changes it from supercritical to subcritical. In other words, q-axis damper windings shrinks the stable region and may lead to loss of synchronism at a value of μ below that which the Hopf bifurcation occurs.

Adding damper windings on either the d-axis or both q- and d-axes also shifts the Hopf bifurcation to smaller value of μ and hence shrinks the stable region. However, the Hopf bifurcation remains supercritical. In general, the damper windings distabilize the system by reducing the compensation level at which subsynchronous resonance occurs.

For the CHOLLA#4 system, we use a complete turbine-generator model that includes

the generator damper windings, the generator saturation, and the automatic voltage regulator. Results similar to those of the BOARDMAN system have been obtained except that there is only a single supercritical Hopf bifurcation instead of three.

We have studied the effect of the generator saturation on subsynchronous resonances while neglecting the AVR system. The results show that the generator saturation shrinks the positively damped region by shifting the Hopf bifurcation to smaller compensation levels. To enlarge the stability region and damp off the torsional oscillations, we have investigated linear and nonlinear controllers injected into the AVR system. The linear controller increases the compensation level at which subsynchronous resonance occurs. On the other hand, the nonlinear controller does not affect the location and type of the Hopf bifurcation H. The study shows that, the larger the value of the nonlinear controller gain k is, the smaller the amplitude of the limit-cycle born near H is. By increasing the gain k, one can suppress the secondary Hopf bifurcation and hence the bluesky catastrophe.

Future research should continue to see the effect of machine saturation as well as the dynamics of damper windings on subsynchronous resonance for different systems.

REFERENCES

[1] J. W. Ballance and S. Goldberg,"Subsynchronous Resonance in Series Compensated Transmission Lines", *IEEE Trans.* on PAS, pp 1649-1658, Sep./Oct. 1973.

[2] D. N. Walker, C. E. Bowler, R. L. Jackson, and D. A. Hodges,"Results of Subsynchronous Resonance Test at Mohave", IEEE Trans. on PAS, pp 1878-1889, Sep./Oct. 1975.

[3] R. G. Farmer, E. Katz, and A. L. Schwalb,"Navajo Project on Subsynchronous Resonance Analysis and Solutions", IEEE Trans. on PAS, pp 1226-1232, July/Aug., 1977.

[4] IEEE Committee Report, "First Benchmark Model for Computer Simulation of Subsynchronous Resonance," *IEEE Trans.* on PAS, pp. 1565-1570, 1977.

[5] IEEE Committee Report, "Second Benchmark Model for Computer Simulation of Subsynchronous Resonance," *IEEE Trans.* on PAS, pp. 1057-1066, 1985.

[6] IEEE Power System Engineering Committee Report, "Terms, Definitions & Symbols for Subsynchronous Oscillations," *IEEE Trans.* on PAS, pp. 1326-1334, 1985.

[7] IEEE Committee Report, "Reader's Guide to Subsynchronous Resonance," *IEEE Trans.* on PAS, pp. 150-157, 1992.

[8] P. M. Anderson, B. L. Agrawal, and J. E. Van Ness, *Subsynchronous Resonance in Power Systems*, IEEE Press, New York, 1990.

[9] G. Gross and M. C. Hall, "Synchronous Machine and Torsional Dynamics Simulation in the Computation of Electromagnetic Transients," *IEEE Trans.* on PAS, pp. 1074-1085, 1978.

[10] P. H. Beagles, K. Carlsen, M. L. Crenshaw, and M. Temoshok, "Generator and Power System Performance with the GENERREX Excitation System", *IEEE Trans.* on PAS, pp. 489-493, March/April 1976.

[11] A. Edris,"Series Compensation Schemes Reducing the Potential of Resonance", *IEEE Trans.* on PAS,pp. 219-226, Feb. 1990.

[12] L.A. Kilgore, D. G. Ramey, and M. C. Hall,"Simplified Transmission and Generation Analysis Procedures for SSR", *IEEE Trans.* on PAS, pp 1840-1846 Nov./Dec. 1977.

[13] R. D. Rana, S. W. Huff, R. M. Hayes, E. N. Fromholtz, and R. P. Schulz,"AEP's Kanawha River 345 KV Series Capacitor Installation- Subsynchronous Resonance Studies and Torsional Measurements", *Proceedings of the American Power Conference*,pp. 300-305, 1991.

[14] Y. Yu, *Electric Power System Dynamics*, Academic Press, New York, 1983.

[15] A. A. Fouad and K. T. Khu,"Subsynchronous Resonance Zones in the IEEE Bench Mark Power System", *IEEE Trans.* on PAS, May/June 1978.

[16] A. Yan and Y. Yu,"Multi-Mode Stabiliztion of Torsional Oscillations Using Output Feedback Excitation Control", *IEEE Trans.* on PAS, May 1982.

[17] M. R. Iravani and A. A. Edris,"Eigen Analysis of Series Compensation Schemes Reducing the Potential of Subsynchronous Resonance", *IEEE Power System Summer Meeting*, 1994.

[18] W. Zhu,"Analysis of Subsynchronous Resonance in Power Systems", Ph.D Thesis, Oregon State University, June, 1994.

[19] M. R. Iravani and A. Semlyen,"Hopf Bifurcations in Torsional Dynamics (Turbine-Generator)", *IEEE Trans.* on PAS, pp. 28-36, Feb. 1992.

[20] W. Zhu, R. R. Mohler, R. Spee, W. A. Mittelstadt, and D. Maratukulam," Hopf Bifurcations in a SMIB Power System with SSR", *IEEE Proceeding of the 1995 Summer Meeting*, pp. 531-534, PWRS.

[21] W. Zhu, R. Spee, R. R. Mohler, G. G. Alexander, W. A. Mittelstadt, and D. Maratukulam,"An EMTP Study of SSR Mitigation Using the Thyristor Controlled Series Capacitor", *IEEE Trans.* on Power Delivery, 1995.

[22] E. H. Abed and P. Varaiya, "Nonlinear Oscillations in Power Systems," *International Journal of Electric Power and Energy Systems*, pp. 373-343, 1984.

[23] I. Dobson and H.-D. Chiang, "Towards a Theory of Voltage Collapse in Electric Power Systems," *Syst. Control Ltrs.,*, pp. 253-262, 1989.

[24] M. A. Nayfeh, A. M. A. Hamdan, and A. H. Nayfeh, "Chaos and Instability in a Power System - Primary Resonant Case," *Nonl. Dyn.*, pp. 313-339, 1990.

[25] V. Venkatasubramanian, H. Schättler, and J. Zaborszky, "Voltage Dynamics: Study of a Generator with Voltage Control, Transmission and Matched MW Load," *IEEE Trans. Auto. Control*, pp. 1717-1733, 1992.

[26] V. Ajjarapu and B. Lee, "Bifurcation Theory and its Application to Nonlinear Dynamical Phenomena in an Electrical Power System," *IEEE Trans.*, on PAS, pp. 424-431, 1992.

[27] E. H. Abed, H. Wang, J. C. Alexander, A. M. A. Hamdan, and H.-C. Lee, "Dynamic Bifurcations in a Power System Model Exhibiting Voltage Collapse," *Int. J. Bif. Chaos*, pp. 1169-1176, 1993.

[28] W. Ji and V. Venkatasubramanian, "Dynamics of a Minimal Power System: invariant tori and quasi-periodic motions," *IEEE Trans. Circuits Syst.*, pp. 981-1000, 1995.

[29] A. H. Nayfeh, A. M. Harb, and C.-M. Chin, "Bifurcation in a Power System Model," *Int. J. Bif. Chaos*, vol. 6, pp. 497-512, 1996.

[30] A. H. Nayfeh and B. Balachandran, *Applied Nonlinear Dynamics*, Wiley, New York, 1995.

[31] A. Nayfeh, *Introduction to Perturbation Techniques*, Wiley, New-York, 1983

[32] A. Nayfeh, *Perturbation Methods*, Wiley, New-York, 1973

[33] P. Kundur, *Power System Stability and Control*, Electric Power Research Institute, McGraw-Hill, New York, 1994.

[34] R. G. Harly, D. J. Limebeer, and E. Chirricozzi,"Comparative Study of Saturation Methods in Synchronous Machine Models", *IEE Proc.*, vol. 127, Pt. B, January 1980.

[35] F. P. De Mello and L. N. Hannet,"Representation of Saturation in Synchronous Machines", *IEEE Trans.* on PAS, Nov. 1986

[36] A-R. A. M. Makky,"Representation of Saturated Salient-Pole Synchronous Machine by A Single Magnetization Curve", *Electric Machines and Electromechanics*, vol. 7, pp. 369-380, April 1982.

[37] A. M. El-Serafi and J. Wu,"Saturation Representation in Synchronous Machine Models", *Electric Machines and Power Systems*, vol. 20, pp. 355-369, August 1992.

[38] J. Lemay and T. H. Barton,"Small Perturbation Linearization of the Saturated Synchronous Machine Equations", *IEEE Trans.* on PAS, pp. 233-240, Sept. 1971.

[39] A. H. Nayfeh and O. R. Asfar,"An Analytical Solution of the Nonlinear Eddy-Current Losses in Ferromagnetic Materials", *IEEE Trans. on Magnetics*, vol. MAG-10, June 1974.

[40] J. W. Dougherty and S. H. Minnich,"Finite Element Modeling of Large generators; Calculations Versus Load Test Data", *IEEE Trans.* on PAS, August 1981.

[41] A. M. El-Serafi, A. s. Abdallah, M. K. Elsherbiny, and E. H. Badawy, "Experimental Study of the Saturation and the Cross-Magnetizing Phenomenon in Saturated Synchronous Machines", *IEEE Trans. Energy Conversion*, vol. 3

[42] M. K. El-Sherbiny and A. M. El-Serafi,"Analysis of Dynamic Performance of Saturated Machine and Analog Simulation", *IEEE Trans.* on PAS, July 1982.

[43] S. H. Minnich, M. V. K. Chari, and J. F. Berkery,"Operational Inductances of Turbine-Generators by the Finite-Element Method", *IEEE Trans.* on PAS, January 1983.

[44] J. W. Dougherty and S. H. Minnich,"Operational Inductances of Turbine Generators; Test Data Versus Finite-Element Calculations", *IEEE Trans.* on PAS, Oct. 1983.

[45] J. R. Smith, K. J. Binns, S. Williamson, and G. W. Buckley," Determination of Saturated Reactances of Turbogenerators", *IEE Proc.*, vol. 127, Pt. C, May 1980.

[46] K. J. Binns and J. R. Smith,"Prediction Of Load Characteristics of Turbogenerators", *IEE Proc.*, vol. 125, March 1978.

[47] J. C. Flores, G. W. Buckley, and G. McPherson,"The Effects of Saturation on the Armature Leakage Reactance of Large Synchronous Machines", *IEEE Trans.* on PAS, March 1984.

[48] R. Natarajan and J. Wang,"Estimation of Synchronous Machine Parameters from Performance Relations", *Electric Power Systems Research*, Vol. 20, pp. 173-179, 1991.

[49] C. Concordia, *Synchronous Machines*, John Wiley & Sons, 1951.

[50] A. E. Fitzgerald and C. Kingsley, *Electric Machinery*, McGraw-Hill, 1961.

[51] B. Adkins, *The General Theory of Electrical Machines*, Chapman and Hall, 1964.

[52] S. H. Minnich, R. P. Schulz, D. H. Baker, D. K. Sharma, R. G. Farmer, and J. H. Fish,"Saturation Functions for Synchronous Generators from Finite Elements", *IEEE Trans. Energy Conversion*, vol. EC-2, December 1987.

[53] N. A. Demerdashi and H. B. Hamilton,"A simplified Approach to Determination of Saturated Synchronous Reactances of Large Turbogenerators Under Load", *IEEE Trans.* on PAS, March/April 1976.

[54] R. P. Schulz, C. J. Goering, R. G. Farmer, S. M. Bennett, and D. A. Selin,"Benefit Assessment of Finite-Element Based generator Saturation Model", *IEEE Trans.* on PAS, November 1987.

[55] J. E. Brown, K. P. Kovacs, and P. Vas,"A method of Including the Effects of Main Flux Path Saturation in the Generalized Equations of A.C. Machines", *IEEE Trans.* on PAS, January 1983.

[56] V. Brandwajn,"Representation of Magnetic Saturation in the Synchronous Machine Model in an Electro-Magnetic Transients Program", *IEEE Trans.* on PAS, Sept./Oct. 1980.

[57] K. P. Kovacs,"On the Theory of Cylindical Rotor A.C. Machines, Including Main Flux Saturation", *IEEE Trans.* on PAS, April 1984.

[58] IEEE Committee Report,"Computer Representation of Excitation Systems", *IEEE Trans.* on PAS, June 1968.

[59] A. A. Fouad and K. T. Khu,"Damping of Torsional Oscillations in Power Systems with Series-Compensated Lines",*IEEE Trans.* on PAS, May/June 1978.

[60] O. Saito, H. Mukae, and K. Murotani,"Suppresion of Selef-Excited Oscillations in Series-Compensated Transmission Lines by Excitation Control of Synchronous Machines", *IEEE Trans.* on PAS, Sept./Oct. 1975.

[61] C. E. J. Bowler and D. H. Baker,"Concepts of Supplementary Torsional Damping by Excitation Modulation", *PES Special Publications*, 1981.

[62] C. E. J. Bowler and R. A. Lawson,"Operating Experience with Supplementary Excitation Damping Controls", *PES Special Publications*, 1981.

[63] N. G. Hingorani, "A New Scheme for Subsynchronous Resonance Damping of Torsional Oscillations and Transient Torque - Part I," *IEEE Trans.* on PAS-100, pp 1852-1855, April 1981.

[64] IEEE Committee Report,"Proposed Excitation System Definitions for Synchronous Machines", *IEEE Trans.* on PAS, pp 1248-1258, August 1969.

[65] IEEE Committee Report,"Excitation System Dynamic Characteristics", *IEEE Trans. Power Appar. Syst.*, on PAS-92, pp 64-75, Jan./Feb. 1973.

[66] IEEE Committee Report,"Excitation System Models for Power System Stability Studies", *IEEE Trans.* on PAS, pp 494-509, February 1981.

[67] H. M. Hamdan, "Multivariable Frequency Response Approach Applied to Power System Dynamics and Control",*PhD Thesis*, University of Manchester Institute of Science and Technology, 1977.

Appendix A

Appendix A

$$((R_\ell + R_a)i_d - X_l i_q + e_{cd} + v_0 \sin\delta_r + \omega_r \psi_q) = 0 \tag{A.1}$$

$$(X_l i_d + (R_l + R_a)i_q + e_{cq} + v_0 \cos\delta_r - \omega_r \psi_d) = 0 \tag{A.2}$$

$$P_e = v_d i_d + v_q i_q \tag{A.3}$$

$$Q_e = v_q i_d - v_d i_q \tag{A.4}$$

$$v_d = -R_a i_d + X_q i_q \tag{A.5}$$

$$v_q = -(R_a i_q + X_d i_d) + X_{md} i_f \tag{A.6}$$

$$v_t^2 = v_d^2 + v_q^2 \tag{A.7}$$

$$\omega_r = \omega_1 = \omega_2 = \omega_3 = \omega_4 = 1 \tag{A.8}$$

$$\delta_r = \theta_1 = \theta_2 = \theta_3 = \theta_4 \tag{A.9}$$

where

$$e_{cd} = X_c i_q \tag{A.10}$$

$$e_{cq} = -X_c i_d \tag{A.11}$$

Given P_e, Q_e, v_t, and $\mu = X_c/X_\ell$, we solve the algebraic system of the seven Eqs. given by (1)-(7) to determine the seven state variables $i_d, i_q, i_f, v_d, v_q, v_0$, and δ_r. Then, we calculate v_f and T_m from the following Eqs.

$$v_f = r_f i_f \tag{A.12}$$

$$T_m = (X_q - X_d) i_d i_q + X_{md} i_q i_f \tag{A.13}$$

VITA

The auther was born in Irbid, Jordan. He received the B.S. degree from Yarmouk University, Irbid, Jordan, in 1987, and the M.S. degree from the Jordan University of Science and Technology, Irbid, Jordan, in 1990, both in electrical engineering. Currently, he is completing his Ph.D. degree in electrical engineering at Virginia Polytechnic Institute and State University. His research interests include power system analysis and control, nonlinear dynamics, power system planning, electric machine design, optimal control, and linear system analysis.